

**Investigation of the Mechanism and  
Dynamics of Resonance Excitation Energy  
Transfer from Photoexcited Donors to Metal  
Nanoparticles and Nanoclusters**

**Ph.D. Thesis**

*by*

**ROOPALI PRAJAPATI**



**DISCIPLINE OF CHEMISTRY**

**INDIAN INSTITUTE OF TECHNOLOGY INDORE**

**NOVEMBER 2017**



**Investigation of the Mechanism and  
Dynamics of Resonance Excitation Energy  
Transfer from Photoexcited Donors to Metal  
Nanoparticles and Nanoclusters**

**A THESIS**

*Submitted in partial fulfillment of the  
requirements for the award of the degree*

*of*

**DOCTOR OF PHILOSOPHY**

*by*

**ROOPALI PRAJAPATI**



**DISCIPLINE OF CHEMISTRY**

**INDIAN INSTITUTE OF TECHNOLOGY INDORE**

**NOVEMBER 2017**





# INDIAN INSTITUTE OF TECHNOLOGY INDORE

## CANDIDATE'S DECLARATION

I hereby certify that the work which is being presented in the thesis entitled **Investigation of the Mechanism and Dynamics of Resonance Excitation Energy Transfer from Photoexcited Donors to Metal Nanoparticles and Nanoclusters** in the partial fulfillment of the requirements for the award of the degree of **DOCTOR OF PHILOSOPHY** and submitted in the **DISCIPLINE OF CHEMISTRY, Indian Institute of Technology Indore**, is an authentic record of my own work carried out during the time period from **JULY 2013** to **NOVEMBER 2017** under the supervision of **Dr. TUSHAR KANTI MUKHERJEE**, Associate Professor, Discipline of Chemistry, IIT Indore.

The matter presented in this thesis has not been submitted by me for the award of any other degree of this or any other institute.

**Signature of the student with date  
(ROOPALI PRAJAPATI)**

-----  
This is to certify that the above statement made by the candidate is correct to the best of my knowledge.

**Signature of Thesis Supervisor with date  
(Dr. TUSHAR KANTI MUKHERJEE)**

-----  
**ROOPALI PRAJAPATI** has successfully given his Ph.D. Oral Examination held on .....

Signature of Chairperson (OEB)      Signature of External Examiner      Signature of Thesis Supervisor

Date:

Date:

Date:

Signature of PSPC Member #1

Signature of PSPC Member #2

Signature of Convener, DPGC

Date:

Date:

Date:

Signature of Head of Discipline

Date:

-----



## **Acknowledgements**

I enunciate my heartfelt gratitude to my thesis supervisor Dr. Tushar Kanti Mukherjee for his unwavering support and constructive guidance throughout my work. His confidence, enthusiasm, and dedication have been always inspirational. His deep insights and suggestions helped me a lot at various stages of my research. His persistent patience, understanding, and motivation have been immensely helpful for the completion of this journey.

I am thankful to my PSPC members, Dr. Anjan Chakraborty and Dr. Srivathsan Vasudevan for their guidance and valuable suggestions during my work.

I wish to express my gratitude to Prof. Pradeep Mathur, Director, IIT Indore for his continuous support in every aspect.

I would like to thank IIT Indore for providing infrastructure and financial support.

I would also like to thank Dr. Satya S. Bulusu, Dr. Tridib Kumar Sarma, Dr. Apurba Kumar Das, Dr. Sanjay Kumar Singh, Dr. Suman Mukhopadhyay, Dr. Biswarup Pathak, Dr. Shaikh M. Mobin, Dr. Rajneesh Misra, Dr. Sampak Samanta, Dr. Chelvam Venkatesh, and Dr. Amrendra Kumar Singh for their guidance and help during various activities in the department.

I extend my deep thanks to my group members Dr. Surajit Chatterjee, Dr. Arpan Bhattacharya, Ms. Jamuna Vaishnav, Mr. Ashish Raikwar, Mrs. Shallu Tanwar, and Mr. Pushpender Yadav for their generous help and co-operation.

I would also like to thank Ms. Sarita Batra, Mr. Kinny Pandey, Mr. Ghanshyam Bhavsar, Mr. Ravinder Kumar, Mr. Manish Kushwaha, Ms. Vinita Kothari, and Mr. Rameshwar Dauhare for their technical support. I would also like to thank Ms. Anjali Bandiwadekar, Mr. Rajesh Kumar, Mr. Lala Ram Ahirwar and other library staffs for their constant help, whenever required.

Further, I would like to acknowledge SIC, IIT Indore for instrumentation facilities. I would like to thank SAIF, IIT Bombay for TEM facility. I sincerely thank Professor Anindya Datta from IIT Bombay for his help during femtosecond upconversion and dynamic light scattering measurements.

I would also like to thank all my co-researchers at Discipline of Chemistry, IIT Indore. It has been a wonderful experience to work with many seniors and friends during my Ph.D. who really helped me in many aspects. I would like to record my thanks to Dr. Bhagwati, Dr. Tamalika, Dr. Rajendar, Dr. Sonam, Dr. Dnyaneswar, Dr. Bhausahab, Dr. Anupam, Dr. Thaksen, Ms. Neha, Ms. Nishu, Ms. Daisy, Mr. Biju, Mr. Siddarth, Mr. Soumya, Mr. Miraj, Mr. Abhiram, Ms. Anupama and many others for their generous help and co-operation.

I would personally like to extend my heartiest thanks to Mrs. Linia Anie Kurian for standing with me in all the ups and downs during this time. Her faith in almighty and my faith in her belief kept me strong enough to fruitfully complete this journey. My friends Ms. Kavita Gupta and Dr. Indrani Choudhuri will always be remembered for understanding and supporting me in all the phases throughout my Ph.D. tenure.

I would like to take this opportunity to express my respect, love, and gratitude to my teachers Mrs. Shilpa Lamba and Dr. Tripti Kumari for

their persistent belief in me. I owe a lot to their motivation, affection, and blessings ever since I met them.

I also extend credits to all my friends outside the institute, especially, Mayank, Amrita, Khushvender, Neha and Pankaj for being the strongest possible pillars in all the ups and downs during my professional as well as personal life. Whether it is through the way they comforted me when I was down or the way they cheered me up when I was overjoyed, they have been there, each and every single day, to make sure that my life turned out this way. Without their companionship, this journey would have been way too difficult.

Most importantly, it would have been impossible for me to reach here without the support, care, and love of my family. I express my respect, love, and gratitude to my beloved maternal grandparents Mr. Des Raj Prajapati and Mrs. Bhagwati Devi, my parents Mr. Parveen Aggarwal and Mrs. Meena Aggarwal, and my siblings Muskan Aggarwal and Sheel Aggarwal, for their unconditional love and support.

I thank each and every single person who, knowingly or unknowingly, helped me during this time.

**ROOPALI PRAJAPATI**



*Dedicated to*

*My Maternal Grandparents*

*&*

*My Parents*



# Abstract

The resonance excitation energy transfer (EET) from various photoexcited donors to acceptors has been studied thoroughly in the recent past due to its importance in photovoltaics, light-emitting diodes, sensors, bioimaging, etc. Nonradiative energy transfer from a photoexcited donor to an acceptor via dipole-dipole interactions is well known as Förster resonance energy transfer (FRET). Over the last few years, metal and semiconductor nanoparticle (NPs) based donor-acceptor composite systems have gained considerable attention due to their size-dependent optoelectronic properties which allow easy tuning of energy transfer efficiency. For example, semiconductor NPs or quantum dots have been extensively used as FRET-based donor due to their stable and bright size-dependent photoluminescence (PL) in the visible region of the electromagnetic spectrum. It has been observed that metal NP with distinct localized surface plasmon resonance (LSPR) often quenches the molecular excitation energy of nearby fluorophore by nanometal surface energy transfer (NSET), which is quite different from the conventional FRET. Extensive theoretical and experimental studies have been performed to understand the mechanism behind the highly efficient quenching of molecular excitation energy of various photoexcited fluorophores by metal NPs. Some reports have illustrated the PL quenching of photoexcited donors in the presence of metal NPs by FRET mechanism, whereas several other studies have demonstrated that EET from photoexcited donor to metal NP is best modeled by NSET theory. Moreover, it has been reported that NSET does not require the spectral overlap between the emission spectrum of donor and absorption spectrum of acceptor. In contrast, several researchers have validated the involvement of spectral overlap in NSET process. Despite numerous reports, the fundamental mechanism of EET from various photoexcited donors to metal NP as well as the role of spectral overlap in the EET process still remains obscure.

Moreover, very less is known about the mechanism and dynamics of fluorescence quenching near the ultrasmall metal nanocluster (NC) surface, which lacks characteristic LSPR. In this thesis, the detailed mechanism and dynamics of EET from various photoexcited donors such as silicon quantum dots (Si QDs), carbon dots (CDs), and 4',6-diamidino-2-phenylindole (DAPI) to silver nanoparticles and nanoclusters (Ag NP and Ag NC) as acceptors have been demonstrated. The role of spectral overlap between donor emission spectrum and LSPR band of Ag NPs in NSET process as well as the effect of different sizes of NPs on NSET efficiency has been clearly presented. Furthermore, the influence of various microheterogeneous environments such as surfactants, polymer, and DNA on the efficiency of energy transfer has been illustrated.

The contents of each chapter included in the thesis are discussed briefly as follows:

## **1. Introduction**

In this chapter, a brief overview of the unique optical properties of Ag NP, Ag NC, Si QD, and CD has been provided. The effect of metal NPs and NCs on the emission properties of various photoexcited fluorophores has been briefly explained. The mechanism and dynamics of various EET theories have been discussed in detail. Further, the importance of spectroscopic nanorulers such as FRET and NSET, in numerous biologically relevant microheterogeneous environments has been illustrated.

## **2. Materials and experimental techniques**

The details of all the chemicals and complete synthetic procedures of citrate-stabilized Ag NP, dihydrolipoic acid-capped Ag NC, allylamine-functionalized Si QD, and CD have been mentioned here. A brief description of the sample preparations and experimental techniques used to complete the entire work of this thesis has been provided.

### **3. Surfactant-induced modulation of nanometal surface energy transfer from silicon quantum dots to silver nanoparticles**

In this chapter, the EET from Si QD to Ag NP and its modulation in the presence of CTAB surfactant has been demonstrated by means of steady-state and time-resolved PL spectroscopy. Significant spectral overlap between the emission spectrum of Si QDs and localized surface plasmon resonance (LSPR) of Ag NPs results in a substantial amount of PL quenching of Si QDs. In addition, the PL lifetime of Si QDs is shortened in the presence of Ag NPs. The origin of this PL quenching has been rationalized on the basis of increased nonradiative decay rate due to EET from Si QDs to Ag NPs surface. The observed energy transfer efficiency correlates well with the NSET theory with  $1/d^4$  distance dependence rather than conventional FRET theory. It has also been observed that the EET efficiency drastically reduces in the presence of 0.5 mM CTAB. Dynamic light scattering (DLS), and single particle PL microscopy results indicate the formation of large surfactant-induced aggregates of Ag NPs. Finally, the energy transfer efficiency values obtained from experiment have been used to calculate the distance between Si QDs and Ag NPs in the absence and presence of CTAB, which correlates well with the proposed model.

### **4. Resonant excitation energy transfer from carbon dots to different sized silver nanoparticles**

The influence of size on the efficiency of NSET process between excited donor and different sized metal NP is poorly explored in literature. Here in this work, a systematic study has been demonstrated by correlating the size of Ag NPs with the efficiency of EET from photoexcited CD to Ag NP. Three different sized citrate-capped Ag NPs with mean hydrodynamic diameter of  $39.91 \pm 1.03$ ,  $53.12 \pm 0.31$  and  $61.84 \pm 0.77$  nm have been synthesized for the present study. The estimated zeta potential of synthesized CD is  $-25.45 \pm 1.23$  mV while that for the smallest,

medium and largest sized Ag NP is  $-76.24 \pm 3.92$ ,  $-67.60 \pm 4.40$ , and  $-58.01 \pm 3.10$  mV. It has been observed that the spectral overlap between the emission spectrum of CD and LSPR band of Ag NP increases with increase in the size of Ag NPs. The steady-state and time-resolved PL measurements reveal significant PL quenching of CD as a function of Ag NP size. A control experiment with Ag NPs having LSPR at 398 nm shows negligible amount of PL quenching of CDs. The negligible PL quenching of CD in the presence of Ag NP having inadequate spectral overlap confirms the resonant EET from photoexcited CD to different sized Ag NPs. The separation distances between CD and different sized Ag NPs estimated using FRET theory exceed the FRET limit. The calculated EET related parameters correlate well with the  $1/d^4$  distance-dependent NSET theory. Further, it has been observed that the NSET efficiency increases with increase in the size of Ag NPs. This phenomenon has been explained by considering larger spectral overlap and shorter separation distance between CD and larger sized Ag NPs due to reduced electrostatic repulsion. These results reveal that the size of NP plays an important role in the NSET process and this phenomenon can be easily utilized to tune the efficiency of energy transfer for various applications.

## **5. Effect of compartmentalization of donor and acceptor on the ultrafast resonance energy transfer from DAPI to silver nanoclusters**

In this chapter, the mechanism and dynamics of EET from photoexcited DAPI to dihydrolipoic acid-capped Ag NC and its subsequent modulation in the presence of cationic polymer PDADMAC and CT-DNA have been demonstrated using steady-state FL and femtosecond FL upconversion techniques. The synthesized Ag NCs were characterized using FTIR spectroscopy, mass spectrometry, XPS, HRTEM, DLS, UV-Vis and PL spectroscopy. The mass spectrometric analysis reveals the formation of ultrasmall  $\text{Ag}_4$  NCs with a small amount of  $\text{Ag}_5$  NCs. UV-Vis and PL spectra show distinct molecular-like

optoelectronic behavior of these ultrasmall Ag NCs. The Ag NCs strongly quench the FL of DAPI with concomitant increase in its PL intensity at 675 nm. This steady-state FL quenching proceeds with a significant shortening of FL lifetime of DAPI in the presence of Ag NCs, signifying the nonradiative FRET from DAPI to Ag NCs. Various energy transfer related parameters have been estimated from FRET theory. The present FRET pair shows a characteristic Förster distance of 2.45 nm and can be utilized as a reporter of short-range distances in various FRET-based applications. Moreover, this nonradiative FRET completely suppresses in the presence of both 0.2 wt% PDADMAC and CT-DNA. Steady-state PL, HRTEM, and PL imaging measurements reveal efficient and complete encapsulation of acceptor (Ag NCs) within the polymer matrix. It has been observed that the nonradiative FRET process completely suppresses in the presence of CT-DNA due to the selective binding of DAPI with CT-DNA. This selective compartmentalization of donor and acceptor and the subsequent modification of FRET process may find application in various sensing, photovoltaic, and light harvesting applications.

## **6. Effect of surfactant assemblies on the resonance energy transfer from 4',6-diamidino-2-phenylindole to silver nanoclusters**

Here, the effect of SDS assemblies on the FRET between DAPI and Ag NC in phosphate buffer has been demonstrated by using FL spectroscopy. While DAPI interacts specifically with SDS surfactants in a concentration-dependent manner, Ag NC shows no specific interaction with surfactant assemblies. At very low concentrations of SDS ( $< 0.6$  mM), DAPI forms surfactant-induced aggregates at the interface. In the case of intermediate SDS concentrations ( $0.6 \text{ mM} \leq \text{SDS} < 4 \text{ mM}$ ), DAPI associates with the negatively charged SDS pre-micelles via electrostatic interaction. Beyond 4 mM SDS, the FL intensity of DAPI saturates due to complete incorporation of DAPI into the micellar Stern layer. The negligible changes in the FL of DAPI upon addition of non-ionic triton X-

100 (TX-100) and cationic CTAB surfactants indicate minimal interaction of DAPI with TX-100 and CTAB. Hence, the significant FL enhancement of DAPI in the presence of SDS is due to the specific electrostatic interactions between the positively charged DAPI and negatively charged SDS. Notably, the interaction between DAPI and Ag NC significantly perturbs in the presence of SDS. In phosphate buffer, FRET efficiency ( $\phi_{\text{Eff}}$ ) of 78% has been estimated for DAPI-Ag NC pair. This  $\phi_{\text{Eff}}$  decreases to 23% in the presence of 1 mM SDS. Furthermore, in the presence of 16 mM SDS, complete suppression of this nonradiative FRET has been observed due to incorporation of DAPI into the micellar Stern layer.

## 7. Conclusion and future scope

The conclusions of the entire research work of this thesis described here are as follows:

- 1) The observed PL quenching of Si QDs in the presence of Ag NPs correlates well with NSET rather than FRET model. The NSET efficiency significantly reduces in the presence of 0.5mM CTAB. The CTAB molecules not only induce aggregation of Ag NPs, but also provide an extra bilayer shell on top of the citrate-capped Ag NPs, due to which the mean separation distance between Si QD and the surface of Ag NP increases. As a result, the NSET efficiency decreases.
- 2) The steady-state and time-resolved lifetime measurements reveal that the observed PL quenching of CD in the presence of different sized Ag NPs is due to the resonant EET. The separation distances between CD and different sized Ag NPs estimated using FRET theory exceed the FRET limit. The calculated EET related parameters correlate well with NSET theory. Moreover, the NSET efficiency increases with increase in the size of Ag NPs. It was observed that with increase in the size of Ag NPs, the spectral

overlap increases. More importantly, the zeta potential of Ag NPs decreases with increase in the size and as a consequence, the effective distance between CD and Ag NPs decreases due to reduced electrostatic repulsion. Hence, these results reveal that the efficiency of NSET process can be easily tuned as a function of NP size.

- 3) The significant FL quenching of DAPI by Ag NC with a concomitant increase in the PL of Ag NCs clearly signifies the involvement of FRET from photoexcited DAPI to Ag NC. Selective compartmentalization of Ag NC and DAPI has been observed in the presence of 0.2 wt% PDADMAC and CT-DNA, respectively. Moreover, complete suppression of the nonradiative FRET has been observed in the presence of both 0.2 wt% PDADMAC and CT-DNA.
- 4) It has been shown that the specific electrostatic interactions of DAPI with SDS significantly alter the FRET process between DAPI and Ag NC. The FRET efficiency of DAPI-Ag NC pair reduces from a bulk value of 78% to 23% in the presence of 1 mM SDS. Furthermore, this FRET completely suppresses in the presence of 16 mM SDS due to the incorporation of DAPI into the micellar Stern layer of SDS.

Further, the relevant future scope of the work described in this thesis has been discussed briefly.



## List of Publications

- 1) **Prajapati R.**, Chatterjee S., Bhattacharya A., Mukherjee, T. K. (2015), Surfactant-induced modulation of nanometal surface energy transfer from silicon quantum dots to silver nanoparticles, *J. Phys. Chem. C*, 119, 13325-13334. (DOI: 10.1021/acs.jpcc.5b02903)
- 2) **Prajapati R.**, Chatterjee S., Kannaujiya K., Mukherjee T. K. (2016), Effect of compartmentalization of donor and acceptor on the ultrafast resonance energy transfer from DAPI to silver nanoclusters, *Nanoscale*, 8, 13006-13016. (DOI: 10.1039/C6NR01792D)
- 3) **Prajapati R.**, Bhattacharya A., Mukherjee T. K. (2016), Resonant excitation energy transfer from carbon dots to different sized silver nanoparticles, *Phys. Chem. Chem. Phys.*, 18, 28911-28918. (DOI: 10.1039/C6CP05451J)
- 4) **Prajapati R.**, Mukherjee T. K. (2017), Effect of surfactant assemblies on the resonance energy transfer from 4', 6-diamidino-2-phenylindole to silver nanoclusters, *J. Photochem. Photobiol. A.*, 353, 130-137. (DOI:10.1016/j.jphotochem.2017.11.016)
- 5) Chatterjee S., **Prajapati R.**, Bhattacharya A., Mukherjee, T. K. (2014), Microscopic evidence of “Necklace and Bead”-like morphology of polymer-surfactant complexes: A comparative study on PVP-SDS and PDADMAC-SDS systems, *Langmuir*, 30, 9859-9865. (DOI: 10.1021/la5022615)
- 6) Bhattacharya A., **Prajapati R.**, Chatterjee S., Mukherjee, T. K. (2014), Concentration-dependent reversible self-oligomerization of serum albumins through intermolecular  $\beta$ -sheet formation, *Langmuir*, 30, 14894-14904. (DOI: 10.1021/la5034959)

- 7) Bhattacharya A., Chatterjee S., **Prajapati R.**, Mukherjee T. K. (2015), Size-dependent penetration of carbon dots inside the ferritin nanocages: Evidence for the quantum confinement effect in carbon dots, *Phys. Chem. Chem. Phys.*, 17, 12833-12840. (DOI: 10.1039/C5CP00543D)

- Publications 5-7 are not a part of this thesis.

# Table of Contents

<i>1. List of Figures</i>	<b>xxiii</b>
<i>2. List of Schemes</i>	<b>xxxix</b>
<i>3. List of Tables</i>	<b>xxxv</b>
<i>4. Acronyms</i>	<b>xxxvii</b>
<i>5. Nomenclature</i>	<b>xxix</b>
<i>Chapter 1: Introduction</i>	<b>1-61</b>
1.1. Background	<b>2</b>
1.2. Silver Nanoparticles (Ag NPs)	<b>4</b>
1.3. Silver Nanoclusters (Ag NCs)	<b>5</b>
1.4. Quantum Dots (QDs)	<b>7</b>
1.4.1. Silicon Quantum Dots (Si QDs)	<b>9</b>
1.4.2. Carbon Dots (CDs)	<b>11</b>
1.5. Influence of Metal NPs and NCs on the Nearby Fluorophore	<b>13</b>
1.6. Mechanism of Excitation Energy Transfer (EET)	<b>14</b>
1.6.1. Förster Resonance Energy Transfer (FRET)	<b>16</b>
1.6.2. Gersten-Nitzan (G-N) model	<b>19</b>
1.6.3. CPS-Kuhn model	<b>21</b>
1.6.4. Nanometal Surface Energy Transfer (NSET)	<b>23</b>
1.7. Resonance EET from Photoexcited Donors to Metal NPs and NCs	<b>26</b>
1.8. Microheterogeneous Environments	<b>29</b>
1.8.1. Surfactant Assemblies	<b>29</b>

1.8.2. Polymer	31
1.8.3. Deoxyribonucleic acid (DNA)	32
1.9. FRET and NSET in Microheterogeneous Environments	33
1.10. Organization of Thesis	35
1.11. References	38
<b><i>Chapter 2. Materials and Experimental Techniques</i></b>	<b>63-77</b>
2.1. Introduction	64
2.2. Chemicals	64
2.3. Synthesis	65
2.3.1. Citrate-Stabilized Silver Nanoparticles (Ag NPs)	65
2.3.2. Dihydrolipoic Acid-Capped Silver Nanoclusters (Ag NCs)	66
2.3.3. Allylamine-Capped Silicon Quantum Dots (Si QDs)	67
2.3.4. Carbon Dots (CDs)	68
2.4. Sample Preparations	68
2.5. Instrumentation	70
2.5.1. Fourier Transform Infrared (FTIR) Spectrometer	70
2.5.2. Atomic Force Microscope (AFM)	70
2.5.3. Field-Emission Scanning Electron Microscope (FE-SEM)	70
2.5.4. Transmission Electron Microscope (TEM)	70
2.5.5. Liquid Chromatography-Mass Spectrometer (LC-MS)	71
2.5.6. Powder X-Ray Diffractometer (PXRD)	71

2.5.7. X-ray Photoelectron Spectrometer (XPS)	71
2.5.8. Dynamic Light Scattering (DLS) and Zeta Potential	71
2.5.9. UV-Vis Spectrophotometer	72
2.5.10. Spectrofluorometer	72
2.5.11. Time-Correlated Single Photon Counting Technique (TCSPC)	72
2.5.12. Femtosecond Fluorescence Upconversion	73
2.5.13. Single Molecule Epifluorescence Microscopy	74
2.6. References	76
<b><i>Chapter 3: Surfactant-Induced Modulation of Nanometal Surface Energy Transfer from Silicon Quantum Dots to Nanoparticles</i></b>	<b>79-111</b>
3.1. Introduction	80
3.2. Results and Discussion	81
3.2.1. Characterization of Si QDs and Ag NPs	81
3.2.2. Interaction of Si QDs and Ag NPs with CTAB	85
3.2.3. Steady-State PL Quenching of Si QDs in the Presence of Ag NPs	92
3.2.4. Time-Resolved PL Quenching of Si QDs in the Presence of Ag NPs	95
3.2.5. Mechanism of EET from Si QDs to Ag NPs	99
3.3. Conclusions	102
3.4. References	104
<b><i>Chapter 4: Resonant Excitation Energy Transfer from Carbon Dots to Different Sized Silver Nanoparticles</i></b>	<b>113-137</b>

4.1.	Introduction	<b>114</b>
4.2.	Results and Discussion	<b>115</b>
4.2.1.	Characterization of CDs and Ag NPs	<b>115</b>
4.2.2.	Steady-State PL Measurements of CD in the Presence of Ag NPs	<b>119</b>
4.2.3.	Time-Resolved PL Measurements of CD in the Presence of Ag NPs	<b>123</b>
4.2.4.	Mechanism of EET from CD to Ag NPs	<b>126</b>
4.3.	Conclusions	<b>130</b>
4.4.	References	<b>132</b>
<b><i>Chapter 5: Effect of Compartmentalization of Donor and Acceptor on the Ultrafast Resonance Energy Transfer from DAPI to Silver Nanoclusters</i></b>		<b>139-172</b>
5.1.	Introduction	<b>140</b>
5.2.	Results and Discussion	<b>141</b>
5.2.1.	Characterization of Ag NCs	<b>141</b>
5.2.2.	Excitation Energy Transfer from DAPI to Ag NCs	<b>147</b>
5.2.3.	Effect of Ag NCs-Polymer Composite Formation on the FRET Process	<b>153</b>
5.2.4.	Effect of DNA Binding of DAPI on the FRET Process	<b>160</b>
5.3.	Conclusions	<b>164</b>
5.4.	References	<b>166</b>
<b><i>Chapter 6: Effect of Surfactant Assemblies on the Resonance Energy Transfer from 4',6-diamidino-2- phenylindole to Silver Nanoclusters</i></b>		<b>173-202</b>

6.1.	Introduction	174
6.2.	Results and Discussion	175
6.2.1.	Interaction of DAPI with SDS: Steady-State FL Measurement	175
6.2.2.	Time-Resolved FL Measurements: DAPI-SDS System	180
6.2.3.	Effect of Surfactant Assemblies on FRET Between DAPI and Ag NC	184
6.3.	Conclusions	193
6.4.	References	195
	<b><i>Chapter 7: Conclusions and Future Scopes</i></b>	<b>203-208</b>
7.1.	Conclusions	204
7.2.	Scope for Future Works	207



## List of Figures

### Chapter 3

- Figure 3.1.** FTIR spectrum of synthesized allylamine-capped Si QDs. **82**
- Figure 3.2.** (A) AFM image and (B) size distribution histogram of allylamine-capped Si QDs. **83**
- Figure 3.3.** Absorption and PL spectra ( $\lambda_{\text{ex}} = 375$  nm) of Si QDs. **83**
- Figure 3.4.** (A) AFM image of synthesized Ag NPs. The inset shows the height profile of two Ag NPs marked with an arrow. (B) The size distribution histogram of Ag NPs from DLS measurement. The mean hydrodynamic diameter is mentioned with the standard deviation. (C) The absorption spectrum of Ag NPs. **84**
- Figure 3.5.** (A) Changes in the LSPR of Ag NPs (black and blue line) and absorption spectra of Si QDs (red and green line) in the presence of 0.5 mM CTAB. (B) The maximum absorbance of Ag NPs versus CTAB concentrations. Changes in the LSPR of Ag NPs upon addition of (C) SDS and (D) TX-100. **86**
- Figure 3.6.** (A) Size distribution histogram of Ag NPs in the presence of 0.5 mM CTAB from DLS measurement. The mean diameter with standard deviation is mentioned in the figure. (B) The estimated Zeta potentials of citrate-capped Ag NPs in the absence and presence of 0.5 mM CTAB. **88**

<b>Figure 3.7.</b>	(A) PL image and (B) PL intensity profiles of Ag NPs. (C) PL image and (D) PL intensity profiles of Ag NPs in presence of 0.5mM CTAB.	<b>91</b>
<b>Figure 3.8.</b>	(A) Spectral overlap between PL spectrum ( $\lambda_{\text{ex}}=375$ nm) of Si QDs and LSPR band of Ag NPs. Changes in the (B) absorption spectra and (C) PL spectra ( $\lambda_{\text{ex}}=375$ nm) of Si QDs in the presence of 5 pM Ag NPs. (D) PL spectra of Si QDs in the presence of tri-sodium citrate dihydrate at an excitation wavelength of 375 nm.	<b>93</b>
<b>Figure 3.9.</b>	Changes in the (A) absorption spectra and (B) PL spectra ( $\lambda_{\text{ex}}=375$ nm) of Si QDs in the absence and presence of 5 pM Ag NPs with 0.5 mM CTAB.	<b>94</b>
<b>Figure 3.10.</b>	PL decay traces ( $\lambda_{\text{ex}} = 376$ nm) of Si QDs in the absence and presence of (A) 5 pM Ag NPs and (B) 5 pM Ag NPs with 0.5 mM CTAB.	<b>96</b>
<b>Figure 3.11.</b>	Correlation between experimentally obtained EET efficiencies for the Si QDs-Ag NPs system in the absence (red point) and presence (blue point) of 0.5 mM CTAB with the theoretical curves generated from NSET (black line) and FRET (magenta line) theory.	<b>101</b>
<b>Chapter 4</b>		
<b>Figure 4.1.</b>	(A) FTIR spectrum, (B) HRTEM image, the inset shows the magnified image of single CD, (C) size distribution histogram of CDs from DLS measurements, and (D) normalized absorption (black line) and PL spectra (red line) of CDs at $\lambda_{\text{ex}} = 400$ nm.	<b>116</b>

<b>Figure 4.2.</b>	(A) Elemental analysis histogram and (B) powder XRD spectrum of the synthesized CDs.	<b>117</b>
<b>Figure 4.3.</b>	(A) Size distribution histograms estimated from SEM measurements for s-Ag NP (blue), m-Ag NP (green), and l-Ag NP (red). The inset of each graph shows SEM image of respective Ag NP. (B) The hydrodynamic size distribution histogram of synthesized s-, m- and l-Ag NPs estimated from DLS measurements. (C) Normalized LSPR of s-, m- and l-Ag NPs.	<b>118</b>
<b>Figure 4.4.</b>	(A) Spectral overlap between LSPR bands of different sized Ag NPs and PL spectrum ( $\lambda_{\text{ex}} = 400$ nm) of CDs. The inset shows the changes in the absorption spectra of CDs in the presence of 20 pM s-, m-, and l-Ag NPs. Changes in the PL spectra ( $\lambda_{\text{ex}} = 400$ nm) of CDs upon addition of (B) s-, (C) m-, and (D) l-Ag NPs.	<b>120</b>
<b>Figure 4.5.</b>	(A) Steady-state Stern-Volmer plots for CDs in the presence of s-, m- and l-Ag NPs. (B) Normalized excitation spectra ( $\lambda_{\text{em}} = 495$ nm) of CD upon addition of 20 pM s, m, and l-Ag NPs. (C) Spectral overlap between the LSPR of Ag NP ( $\lambda_{\text{LSPR}} = 398$ nm) and PL spectrum ( $\lambda_{\text{ex}} = 400$ nm) of CDs. (D) The steady-state Stern-Volmer plot for CDs in the presence of Ag NP having an LSPR band at 398 nm.	<b>121</b>
<b>Figure 4.6.</b>	Changes in the PL decay traces ( $\lambda_{\text{ex}} = 405$ nm) of CD in the presence of s, m, and l- Ag NPs recorded at 495 nm emission wavelength.	<b>124</b>
<b>Figure 4.7.</b>	Theoretical curve of energy transfer efficiency	<b>128</b>

against the distance between CD and Ag NP generated from NSET theory. Separation distances obtained from the experimentally determined energy transfer efficiencies are highlighted with blue, green and red arrows for s, m, and l- Ag NPs (20 pM) respectively.

## Chapter 5

- Figure 5.1.** (A) FTIR spectra of dihydrolipoic acid and synthesized Ag NCs. (B) The normalized absorption (black line) and PL (red line) spectra of 5  $\mu$ M Ag NCs. Photographs of Ag NCs in pH 7.4 buffer under of (i) day-light and (ii) UV light. **143**
- Figure 5.2.** (A) Normalized PL spectra of Ag NCs at different excitation wavelengths. (B) Absorption and normalized PL spectrum ( $\lambda_{\text{ex}}= 375$  nm) of Ag(I)-DHLA complex. **143**
- Figure 5.3.** Electrospray ionization mass spectrum of as-synthesized DHLA-capped Ag NCs in 1:1 water-methanol mixture (L represents DHLA ligand). The inset shows the mass spectrum beyond 850 m/z. **144**
- Figure 5.4.** Expanded XPS spectra of the elements (A) Ag 3d, (B) S 2p, (C) C 1s, and (D) O 1s of DHLA-capped Ag NC. **145**
- Figure 5.5.** (A) HRTEM image of Ag NCs. The inset shows the presence of lattice planes with interfringe distance of 0.23 nm. Size distribution histogram of Ag NCs estimated from (B) TEM and (C) DLS measurements. **146**

- Figure 5.6.** (A) The normalized absorption spectrum (black dashed line) and fluorescence ( $\lambda_{\text{ex}} = 375$  nm) spectrum (black line) of 2.5  $\mu\text{M}$  DAPI and the normalized absorption spectrum of Ag NCs (red line). The blue dotted region shows the overlap between the absorption spectrum of Ag NCs and fluorescence of DAPI. (B) Changes in the fluorescence spectra ( $\lambda_{\text{ex}} = 375$  nm) of DAPI (black line) and Ag NCs (red line) upon formation of DAPI–Ag NCs composite (blue line). **147**
- Figure 5.7.** (A) Changes in the fluorescence spectra of DAPI (black line) on the addition of DHLA (red line). (B) Normalized (at 500 nm) excitation spectra of Ag NCs ( $\lambda_{\text{em}} = 675$  nm) in the absence (black line) and presence (red line) of DAPI recorded with 399 nm filter. **148**
- Figure 5.8.** (A) Femtosecond fluorescence transients ( $\lambda_{\text{ex}} = 375$  nm) of DAPI in the absence (black) and presence of Ag NCs (blue) recorded at 490 nm emission wavelength. (B) Theoretical curves of energy transfer efficiency against the distance between DAPI and Ag NCs generated from FRET theory. Experimentally obtained energy transfer efficiency from steady-state data is highlighted with a blue color circle. **150**
- Figure 5.9.** (A) Changes in the PL spectra ( $\lambda_{\text{ex}} = 375$  nm) of Ag NCs upon addition of 0.2 wt% PDADMAC. (B) Normalized PL spectra of Ag NCs in buffer (black line) and methanol (red line). **154**

- Figure 5.10.** (A) HRTEM image of Ag NCs-PDADMAC composite system. (B) A zoomed portion of image (A) showing encapsulated Ag NCs inside the PDADMAC matrix. The inset shows the size distribution histogram of encapsulated Ag NCs estimated from the HRTEM measurements. **155**
- Figure 5.11.** (A) PL image and (B) intensity traces of individual Ag NCs. (C) PL image and (D) intensity traces of PDADMAC encapsulated Ag NCs. **156**
- Figure 5.12.** Distribution histogram of (A) intensity and (B) FWHM of Ag NCs in the absence and presence of 0.2 wt% PDADMAC. **157**
- Figure 5.13.** (A) Changes in the fluorescence spectra ( $\lambda_{\text{ex}} = 375$  nm) of DAPI (black line) and Ag NCs (red line) upon formation of DAPI-PDADMAC-Ag NCs composite (blue line). (B) Femtosecond fluorescence transients ( $\lambda_{\text{ex}} = 375$  nm) of DAPI in the absence (black) and presence (blue) of PDADMAC-Ag NCs composite recorded at 490 nm emission wavelength. **158**
- Figure 5.14.** Changes in the fluorescence spectra of DAPI ( $\lambda_{\text{ex}} = 375$  nm) upon addition of 0.2 wt% PDADMAC. **159**
- Figure 5.15.** (A) Absorption spectra and (B) fluorescence spectra of DAPI (2.5  $\mu\text{M}$ ,  $\lambda_{\text{ex}} = 375$  nm) in the absence (black line) and presence (red line) of 10  $\mu\text{M}$  CT-DNA. **161**
- Figure 5.16.** Changes in the PL spectra of Ag NCs upon addition of CT-DNA. **162**

- Figure 5.17.** (A) Changes in the fluorescence spectra ( $\lambda_{\text{ex}} = 375$  nm) of DAPI–DNA complex (blue line) and Ag NCs (red line) upon formation of DAPI–DNA–Ag NCs composite (pink line). (B) Changes in the PL lifetime traces ( $\lambda_{\text{ex}} = 375$  nm) of DAPI–DNA complex (blue) in the presence of 5  $\mu\text{M}$  Ag NCs recorded at 440 nm emission wavelength. **163**
- Chapter 6**
- Figure 6.1.** Changes in the absorption spectra of DAPI upon gradual addition of SDS. **176**
- Figure 6.2.** Changes in the FL spectra of DAPI ( $\lambda_{\text{ex}} = 375$  nm) upon addition of (A) (i) 0 mM, (ii) 0.2 mM, (iii) 0.4 mM, (iv) 0.6 mM SDS and (B) (v) 1 mM, (vi) 2 mM, (vii) 4 mM, (viii) 8 mM and (ix) 16 mM SDS. **177**
- Figure 6.3.**  $I/I_0$  ( $\lambda_{\text{em}} = 492$  nm) against concentrations of surfactant for DAPI in the presence of (A) SDS and (B) TX-100 and CTAB. **178**
- Figure 6.4.** (A) Changes in the FL lifetime decay traces of DAPI ( $\lambda_{\text{ex}} = 375$  nm) in the presence of (A) (i) 0 mM, (ii) 0.2 mM, (iii) 0.4 mM, (iv) 0.6 mM SDS and (B) (v) 1 mM, (vi) 2 mM, (vii) 4 mM, (viii) 8 mM and (ix) 16 mM SDS recorded at 492 nm emission wavelength. (C)  $\tau/\tau_0$  ( $\lambda_{\text{em}} = 492$  nm) against concentrations of SDS for DAPI-SDS system. **182**
- Figure 6.5.** (A) Normalized absorption (black line) and PL (red line) spectra of synthesized Ag NCs at excitation wavelength of 375 nm. (B) HRTEM image of Ag NCs. The inset shows the size distribution **185**

histogram for Ag NCs generated from HRTEM measurements. (C) ESI mass spectrum of synthesized DHLA capped Ag NCs in 1:1 water-methanol mixture.

- Figure 6.6.** Changes in the emission spectra ( $\lambda_{\text{ex}} = 375$  nm) of DAPI (dash blue) and Ag NC (dash red) upon mixing (solid orange) in PBS. **186**
- Figure 6.7.** Changes in the PL spectrum ( $\lambda_{\text{ex}} = 375$  nm) of Ag NCs upon gradual addition of SDS. The inset shows the changes in the absorption spectrum of Ag NCs in the presence of SDS. **188**
- Figure 6.8.** Changes in the emission spectra ( $\lambda_{\text{ex}} = 375$  nm) of DAPI (dash blue) and Ag NC (dash red) upon mixing (solid orange) in (A) 1 mM SDS and (B) 16 mM SDS. **189**
- Figure 6.9.** FL lifetime decay traces ( $\lambda_{\text{ex}} = 375$  nm) of DAPI, upon addition of (A) 1 mM and (B) 16 mM SDS in the absence (i) and presence (ii) of Ag NC ( $\lambda_{\text{em}} = 492$  nm). **190**

## List of Schemes

### Chapter 1

<b>Scheme 1.1.</b>	Electronic energy levels of bulk metal, metal NP, and NC.	<b>2</b>
<b>Scheme 1.2.</b>	Schematic representation of the different ligands stabilizing the Ag NCs.	<b>6</b>
<b>Scheme 1.3.</b>	Quantum confinement and size-tunable PL properties of QDs.	<b>8</b>
<b>Scheme 1.4.</b>	Indirect and direct exciton recombination in bulk silicon and Si QD, respectively.	<b>10</b>
<b>Scheme 1.5.</b>	Schematic illustration of CD preparations via “bottom-up” and “top-down” approaches.	<b>12</b>
<b>Scheme 1.6.</b>	Jablonski diagram for nonradiative resonance energy transfer.	<b>15</b>
<b>Scheme 1.7.</b>	Important parameters on which FRET depends.	<b>18</b>
<b>Scheme 1.8.</b>	Schematic illustration of fluorophore-metal NP donor-acceptor system by G-N theory.	<b>19</b>
<b>Scheme 1.9.</b>	Schematic representation of CPS-Kuhn approximation for a fluorophore-metal thin film as the donor-acceptor pair.	<b>21</b>
<b>Scheme 1.10.</b>	NSET model for the fluorophore-metal NP as the donor-acceptor system.	<b>23</b>
<b>Scheme 1.11.</b>	The chemical structures of CTAB, SDS, and TX-100.	<b>29</b>
<b>Scheme 1.12.</b>	Representation of the surfactant assemblies in solution.	<b>30</b>
<b>Scheme 1.13.</b>	Schematic illustration of the structure of an anionic micelle.	<b>31</b>
<b>Scheme 1.14.</b>	Illustration of a polymer composed of small	<b>32</b>

	monomeric units.	
<b>Scheme 1.15.</b>	Schematic representation of a double-stranded DNA.	<b>33</b>
<b>Chapter 2</b>		
<b>Scheme 2.1.</b>	Synthesis of citrate stabilized Ag NPs.	<b>65</b>
<b>Scheme 2.2.</b>	Synthesis of DHLA-capped Ag NCs.	<b>66</b>
<b>Scheme 2.3.</b>	Synthesis of allylamine-capped Si QDs in TOAB micelles.	<b>67</b>
<b>Scheme 2.4.</b>	Synthesis of CDs using citric acid and ethylenediamine.	<b>68</b>
<b>Scheme 2.5.</b>	Schematic representation of our home-built epifluorescence microscope.	<b>75</b>
<b>Chapter 3</b>		
<b>Scheme 3.1.</b>	Proposed model for CTAB bilayer-induced aggregation of Ag NPs.	<b>89</b>
<b>Scheme 3.2.</b>	Schematic illustration of the CTAB-induced modulation of the NSET between Si QDs and Ag NPs.	<b>102</b>
<b>Chapter 4</b>		
<b>Scheme 4.1.</b>	Schematic representation of EET from CD to different sized Ag NPs.	<b>130</b>
<b>Chapter 5</b>		
<b>Scheme 5.1.</b>	Chemical structures of DAPI and DHLA-capped Ag NC. The parameter $R_0$ indicates the distance from center of DAPI molecule to the center of Ag NC.	<b>153</b>
<b>Scheme 5.2.</b>	Schematic representation of the proposed polymer encapsulation of Ag NCs and subsequent modulation of nonradiative FRET process between DAPI and Ag NCs.	<b>160</b>
<b>Scheme 5.3.</b>	Illustration of the effect of DNA binding of	<b>164</b>

DAPI on the nonradiative FRET process between DAPI and Ag NCs.

**Chapter 6**

**Scheme 6.1.** Interaction of DAPI with different surfactant assemblies of SDS. **184**

**Scheme 6.2.** Schematic representation of the modulation of FRET between DAPI and Ag NC due to the addition of 1 mM and 16 mM SDS. **193**

**Chapter 7**

**Scheme 7.1.** Schematic representation of metal NPs with surface ligands having different alkyl chain length. **208**



## List of Tables

### Chapter 3

- Table 3.1.** PL decay parameters of Si QDs, and Si QDs with Ag NPs in the absence and presence of 0.5 mM CTAB. **97**
- Table 3.2.** Estimated quantum yields, average lifetimes, radiative rates, nonradiative rates, energy transfer rates, and efficiency of energy transfer from Si QDs to Ag NPs in the absence and presence of CTAB. **98**

### Chapter 4

- Table 4.1.** PL decay parameters of CD in the absence and presence of different sized Ag NPs. **124**
- Table 4.2.** Estimated quantum yields, radiative rates, nonradiative rates, energy transfer rates, efficiencies of energy transfer and estimated distance ( $d$ ) between CD and 20 pM Ag NPs. **128**

### Chapter 5

- Table 5.1.** Fluorescence decay parameters of DAPI in the absence and presence of Ag NCs. **152**
- Table 5.2.** Estimated quantum yields, overlap integral ( $J$ ), rate of energy transfer ( $k_{ET}$ ), and  $R_0$  for DAPI-Ag NCs system. **152**
- Table 5.3.** Fluorescence decay parameters of DAPI in the presence of CT-DNA and CT-DNA-Ag NCs system. **163**

### Chapter 6

- Table 6.1.** Fluorescence decay parameters of DAPI in the presence of different concentrations of SDS. **183**

<b>Table 6.2.</b>	Fluorescence decay parameters of DAPI-SDS system in the absence and presence of Ag NCs.	<b>191</b>
<b>Table 6.3.</b>	Estimated quantum yields, radiative rates, nonradiative rates, efficiency of energy transfer, and FRET distance for DAPI-Ag NC pair in the presence of 1 mM SDS.	<b>193</b>

## Acronyms

AFM	Atomic force microscope
Ag NC	Silver nanocluster
Ag NP	Silver nanoparticle
Au NC	Gold nanocluster
Au NP	Gold nanoparticle
CD	Carbon dot
CMC	Critical micelle concentration
CPS-Kuhn	Chance, Prock, Silbey-Kuhn
CTAB	Cetyltrimethylammonium bromide
CT-DNA	Calf thymus DNA
DAPI	4',6-diamidino-2-phenylindole
DHLA	Dihydrolipoic acid
DLS	Dynamic light scattering
DNA	Deoxyribonucleic acid
EET	Excitation energy transfer
EMCCD	Electron-multiplying charge-coupled device
FE-SEM	Field-emission scanning electron microscope
FL	Fluorescence
FL. I.	Fluorescence intensity
FRET	Förster resonance energy transfer
FTIR	Fourier transform infrared
FWHM	Full width at half maxima
G-N	Gersten-Nitzan
IRF	Instrument response function
LC-MS	Liquid chromatography-mass spectrometer
LSPR	Localized surface plasmon resonance
NSET	Nanometal surface energy transfer
O. D.	Optical density
PDADMAC	Poly(diallyldimethylammonium chloride)

PL	Photoluminescence
PL. I.	Photoluminescence intensity
PXRD	Powder X-ray diffractometer
QD	Quantum dot
SDS	Sodium dodecyl sulphate
SERS	Surface-enhanced Raman scattering
TCSPC	Time-correlated single photon counting
TEM	Transmission electron microscope
TX-100	Triton X-100
UV	Ultraviolet
Vis	Visible
XPS	X-ray photoelectron spectrometer

## Nomenclature

a. u.	Arbitrary unit
cm	Centimeter
$\epsilon_2$	Complex dielectric function of the metal
$^\circ$	Degree
$\epsilon_1$	Dielectric function of metal
$\mu$	Dipole moment of the emitter
$d$	Distance from the center of the donor to the metal NP surface
$d_0^{\text{CPS-Kuhn}}$	Donor-acceptor distance given by CPS-Kuhn model at which 50% energy transfer is observed
$d_0$	Donor-acceptor distance given by NSET model at which 50% energy transfer is observed
eV	Electron volt
$\lambda_{\text{em}}$	Emission wavelength
$R$	Estimated donor-acceptor separation distance using FRET theory
$\lambda_{\text{ex}}$	Excitation wavelength
$\tau$	Excited-state lifetime
$\epsilon$	Extinction coefficient
$k_F$	Fermi wave-vector
$\phi$	Fluorescence quantum yield
$R_0$	Förster distance at which 50% energy transfer is observed
$\omega$	Frequency
g	Gram
h	Hour
kDa	Kilodalton
$l$	Mean free path for the metal
$\mu\text{L}$	Microlitre

$\mu\text{m}$	Micrometer
$\mu\text{M}$	Micromolar
mV	Milli volt
mg	Milligram
mL	Millilitre
mM	Millimolar
min	Minute
M	Molar
nm	Nanometer
ns	Nanosecond
$k_{\text{nr}}$	Non-radiative decay rate
$\kappa$	Orientation factor of the transition dipoles of the donor and the acceptor
$\alpha$	Orientation of the donor to the metal plasmon vector
pM	Picomolar
ps	Picosecond
$\phi_{\text{Eff}}$	Quenching efficiency
$k_{\text{r}}$	Radiative decay rate
$r$	Radius of the metal NP
$k_{\text{ET}}$	Rate of energy transfer
$k_{\text{FRET}}$	Rate of FRET
$k_{\text{NSET}}$	Rate of NSET
$\chi^2$	Reduced chi-square
$\eta$	Refractive index of the medium
$\eta_{\text{t}}$	Refractive index of the metal
rpm	Rotations per minute
$J(\lambda)$	Spectral overlap integral
$c$	Speed of light
$F_{\text{Surface}}$	Surface-dependent quenching term
pH	The negative logarithm of hydronium-ion concentration

$F_{Volume}$	Volume-dependent quenching term
$\lambda$	Wavelength

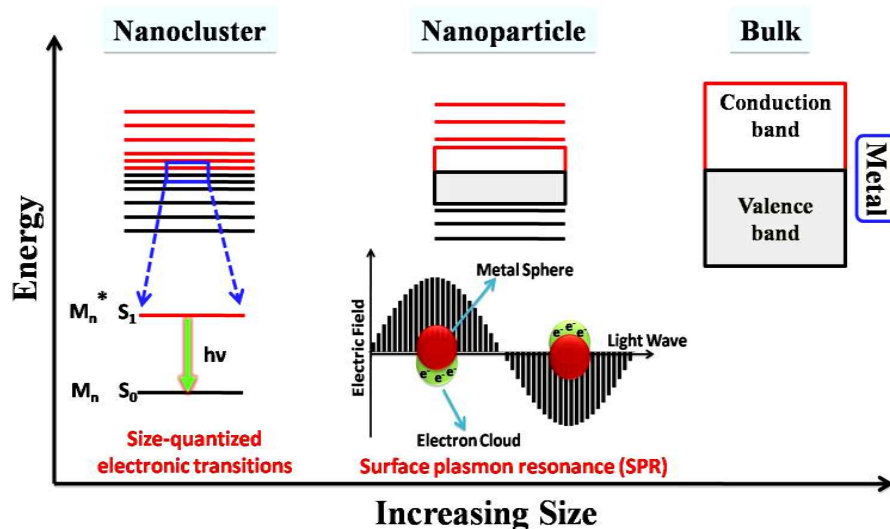


# **Chapter 1**

## *Introduction*

## 1.1. Background

Noble metal nanoparticles (NPs) have attracted considerable attention in the past few decades due to their potential applications in miniature optical devices, sensors, medical diagnostics, therapeutics, etc [1-4]. The electronic and optical properties of metal NPs depend greatly on their size, particularly in the nanometre range (Scheme 1.1) [5-9].



**Scheme 1.1.** Electronic energy levels of metal NC, NP, and bulk metal.

Bulk metals are electrically conducting and good optical reflectors due to the freely moving delocalized electrons in the conduction band. Metal NPs (2-100 nm) display intense colors as a result of the localized surface plasmon resonance (LSPR), which arises due to the collective oscillation of conduction electrons upon interaction with light [5, 6]. When the size of a metal NP is further reduced to around 2 nm or less, the continuous band structure becomes

discrete due to the quantum confinement effect (Scheme 1.1) [7-9]. In such an extremely small size scale, NPs are known as nanoclusters (NCs). These metal NCs are said to have molecule-like properties with discrete electronic energy levels and size-dependent emission.

Extensive theoretical and experimental studies have been performed to understand the emission properties of various fluorophores in the presence of metal NP and NC. Metal NPs and NCs alter the emission properties of fluorophores within the several nanometers from their surface. Metal NPs exhibiting distinct LSPR band are known to either enhance or quench the fluorescence yield of nearby fluorophore [10-20]. The ultrasmall luminescent metal NCs having molecule-like properties affect the nearby fluorophore in an entirely different way as they do not show any LSPR. Metal NCs act as efficient quenchers in the presence of nearby photoexcited molecules [21-23]. The influence of metal NPs and NCs on the fluorescence quantum yield of nearby fluorophore is very complex and depends on various parameters such as size of the metal NP and NC, shape of the metal NP, the separation distance between fluorophore and metal NP or NC, the orientation of fluorophore dipole with respect to metal NP or NC, and the spectral overlap between the emission spectrum of fluorophore and absorption spectrum of metal NP or NC. In this thesis, the effect of silver nanoparticles and nanoclusters (Ag NPs and NCs) on the emission properties of the various fluorophores such as silicon quantum dots (Si QDs), carbon dots (CDs) and 4', 6-diamidino-2-phenylindole (DAPI) has been demonstrated. A brief overview of the optical properties, synthetic routes and applications of Ag NPs, Ag NCs, Si QDs, and CDs has been provided in the next sections.

### 1.2. Silver Nanoparticles (Ag NPs)

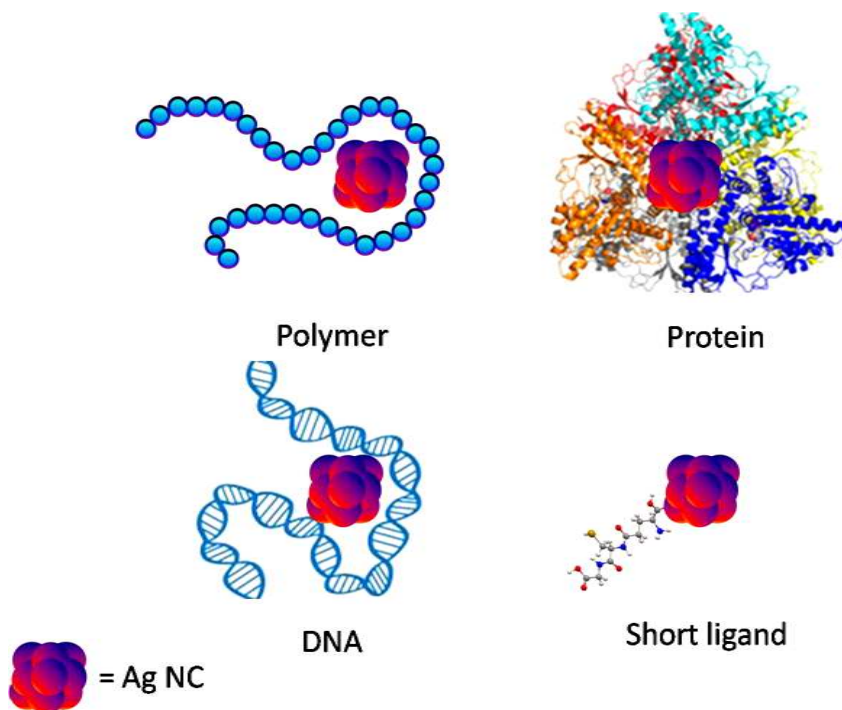
In the past few decades, Ag NPs have been utilized in diverse domains including optoelectronics, biosensors, antimicrobials catalysis, surface enhanced Raman scattering (SERS), near-field scanning probe microscopy, luminescence enhancement and quenching at the metal surface, etc [24-31]. The shape and size of the Ag NP directly influence its characteristic LSPR band. The LSPR maximum ( $\lambda_{\text{LSPR}}$ ) of spherical Ag NP ranges from 390-500 nm depending on the size of the Ag NP [25, 26]. With the increase in the size of NP, the  $\lambda_{\text{LSPR}}$  shifts to the longer wavelength.

Colloidal particles of varying size and shape have been synthesized using templates, photochemistry, seeds, electrochemistry, and radiolysis [32-36]. The simplest and the most commonly used synthetic method for Ag NPs usually makes use of a soluble Ag salt, a reducing agent, and a stabilizing agent. The stabilizing agent caps the NP and prevents further growth or aggregation. The formation of colloidal solutions from the reduction of Ag salts involves two stages, namely nucleation and subsequent growth. The size and shape of the synthesized Ag NPs are strongly dependent on these stages. The initial nucleation and the subsequent growth of the nuclei can be controlled by adjusting the reaction parameters such as reaction temperature, pH, precursors, reducing agents, and stabilizing agents [25, 37-41]. Recently, Agnihotri et al. (2014) precisely controlled the nucleation and growth kinetics to synthesize different sized spherical Ag NPs using sodium borohydride as a primary reducing agent and trisodium citrate, both as secondary reducing agent as well as stabilizing agent [25]. They prepared monodisperse Ag NPs with average size varying from 5-

100 nm exhibiting  $\lambda_{\text{LSPR}}$  in between 393 to 462 nm. They also illustrated the size and dose-dependent bacteriostatic/bactericidal effect of different sized Ag NPs. In this thesis, different sized citrate-capped Ag NPs exhibiting  $\lambda_{\text{LSPR}}$  at 398, 415, 425, 435, and 449 nm have been synthesized by the well-known Lee and Meisels method with slight modifications [42]. The effect of citrate-capped Ag NPs on the emission properties of Si QDs and CDs has been demonstrated.

### 1.3. Silver Nanoclusters (Ag NCs)

Ag NCs have sizes comparable to the Fermi wavelength of an electron and exhibit molecular-like properties including discrete electronic states and size-dependent PL properties [43, 44]. For the synthesis of Ag NCs, the most common route follows the reduction of  $\text{Ag}^+$  ion precursor in the presence of suitable ligand. Various reduction techniques such as radiolytical, photochemical, sonochemical, etc. have been employed for the synthesis of Ag NCs [45-52]. The frequently used capping ligands are DNA, polymer microgels, peptides, proteins, and thiol- or amine-appended molecules (Scheme 1.2) [21, 47, 50-55]. For example, Xiao et al. (2013) synthesized luminescent Ag NCs using ssDNA chain containing 12 cytosine bases as the scaffold. They employed Ag NCs in energy transfer studies and demonstrated the biosensing application of Ag NCs [21]. In another study, Li et al. (2013) synthesized highly stable water-dispersible luminescent  $\text{Ag}_5$  clusters with a PL quantum yield of 9.7% using tridentate polymer ligand. For the first time, they demonstrated the successful application of Ag NCs as biomarkers to label mouse liver tissues [56].



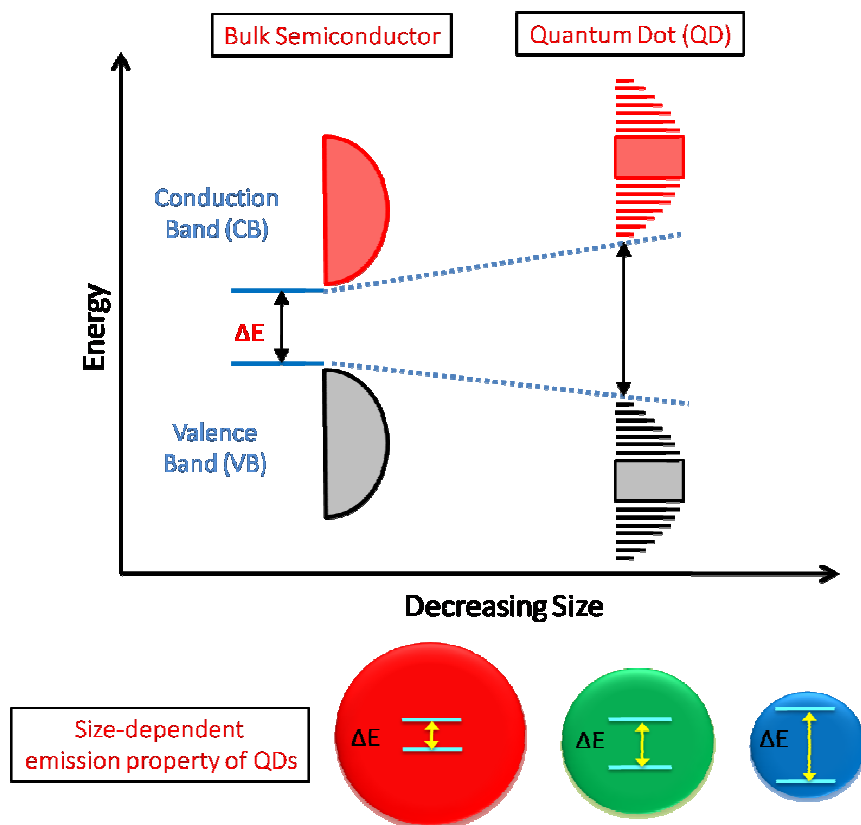
**Scheme 1.2.** Schematic representation of the different ligands stabilizing the Ag NCs.

Small molecules containing carboxylic and thiols groups have also been used to stabilize silver NCs in solution using sodium borohydride as reducing agent [52, 55, 57]. Recently, Adhikari et al. (2010) reported a single step facile synthesis of water-dispersible, dihydrolipoic acid (DHLA) capped luminescent Ag<sub>4</sub> and Ag<sub>5</sub> NCs showing excellent optical properties, narrow emission profile, good photostability, and large Stokes shift [52]. They also demonstrated the sensing application of Ag NC for ultrasensitive detection of highly toxic mercury ions. Over the past few years, Ag NCs due to their excellent optical properties, sub-nanometer size and non-toxicity have

been employed in various important chemical and biological systems [21, 44, 52-54, 56]. In this thesis, the effect of ultrasmall DHLA-capped Ag NCs on the emission properties of DAPI has been demonstrated.

### 1.4. Quantum Dots (QDs)

The term “quantum dot” was first used by Mark A. Reed in 1988 to describe a spatially quantized system, where the electrostatically bound electron-hole pair which is known as exciton is confined in all the three spatial dimensions [58]. The bulk semiconductor consists of the continuous valence band (VB) and conduction band (CB) separated by a region of the forbidden energy gap, known as band gap,  $E_g$ , of the material. An electron gets excited from filled VB to the empty CB leaving a hole in the VB, by absorbing a photon of energy greater than  $E_g$ . The average distance between the electron and hole is called the exciton Bohr radius. When the size of the particle approaches near or below the exciton Bohr radius, the energy bands become discrete and the properties of the particles become size dependent (Scheme 1.3). The energy gap between VB and CB increases as the size decreases resulting in a blue shift of the optical transitions [58-60]. This effect is known as quantum confinement effect, which is usually observed in size regime below 10 nm for most of the semiconductor materials. Compared to bulk materials, QDs show unique size-dependent photoluminescence (PL) properties due to the quantum confinement effect.



**Scheme 1.3.** *Quantum confinement and size-tunable PL properties of QDs.*

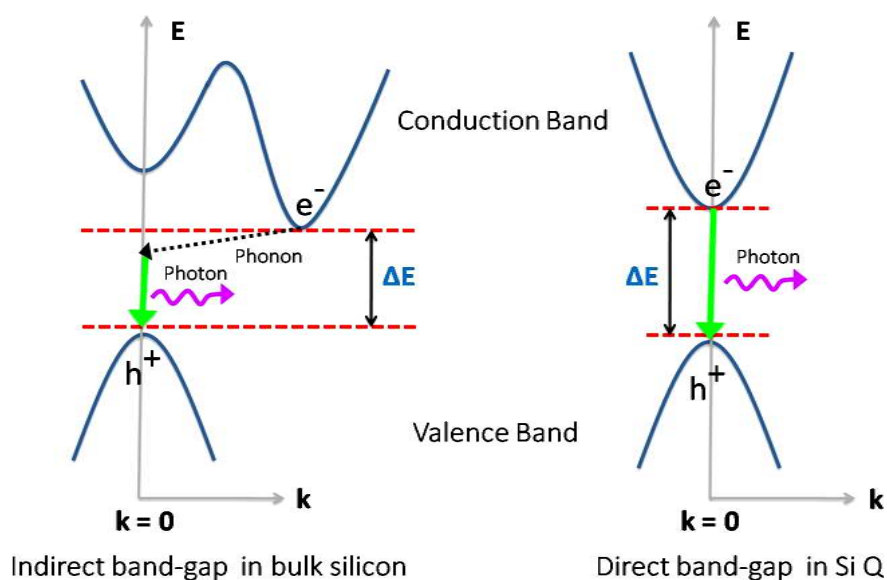
QDs exhibit broad excitation spectra, size- and composition-tunable narrow emission from ultraviolet to near-infrared wavelength range, high quantum yield and better stability against photobleaching. QDs show excitation-dependent emission because of significant size distribution, which allows their selective optical excitation. In addition, QDs have relatively large surface-area to volume ratio which is

promising for its water-solubilization, sensing applications, bioconjugation, etc.

Several solution phase synthesis, purification, and characterization procedures have been well established to synthesize high-quality QDs, consisting elements from the groups II-VI, III-V, and IV-VI of the periodic table, such as CdSe, CdTe, CdS/ZnS, CdSe/ZnS, InAs, etc [61-65]. As a result of their narrow size distribution, selective morphology, controlled surface chemistry and bright PL, these QDs have been widely used for solar cell applications, LEDs, sensors, biolabeling, etc [65-68]. However, these heavy metal QDs possess significant drawbacks in biological application due to their potential cytotoxicity [69-72]. Therefore, extensive research has been carried out to develop less toxic, heavy metal free QDs such as silicon quantum dots (Si QDs), carbon-based nanomaterials such as carbon dots (CDs), graphene quantum dots (GQDs), polymer dots, etc.

### 1.4.1. Silicon Quantum Dots (Si QDs)

Bulk silicon is an indirect bandgap semiconductor material which shows poor applications in light emitting devices (Scheme 1.4). However, as the size of the silicon nanomaterial becomes comparable to its exciton Bohr radius, it exhibits quantum confinement effect. As a consequence, the band gap increases resulting into the direct exciton recombination in Si QD (Scheme 1.4). Si QDs show size-tunable PL emission with high quantum yields [73]. Unlike heavy metal QDs, Si QDs are considered highly promising candidates for large-scale bio-applications, particularly for in vivo applications due to their low-toxicity, good biocompatibility, and smaller size [73].



**Scheme 1.4.** Indirect and direct exciton recombination in bulk silicon and Si QD, respectively.

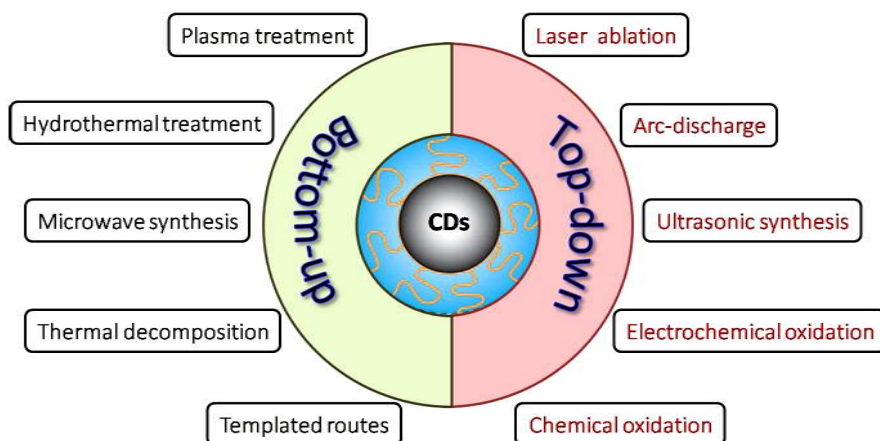
Numerous synthetic methods have been developed over the past few decades for the synthesis of mono-dispersed Si QDs which are broadly classified into “top-down” and “bottom-up” approaches [60-68, 73-80]. Recently, relatively mono-dispersed Si QDs having tunable PL properties have been synthesized with different surface functionalizations such as amines, carboxylic acid, amphiphilic block copolymer, etc. Earlier, Warner et al. (2005) synthesized amine-terminated water-dispersible Si QDs by reducing silicon precursor using hydride reducing agent inside reverse micelles at room temperature [79]. Recently, Clark et al. (2010) prepared and characterized luminescent Si QDs functionalized with propionic acid, pentanoic acid, heptanoic acid, and undecanoic acid [81]. They

illustrated that the oxidative and optical stability was improved by increasing the length of the carbon spacer between the silicon surface and the polar carboxylic acid group. The surface functionalization plays an important role in determining the solubility, stability, cytotoxicity, and hence the applicability of Si QDs in various fields. In this thesis, the PL properties of allylamine-capped Si QDs in the presence of citrate-capped Ag NPs have been explored.

### 1.4.2. Carbon Dots (CDs)

In 2004, while purifying single-walled carbon nanotubes, Xu et al. (2004) serendipitously discovered an unknown luminescent carbon nanomaterial which is now referred to as carbon quantum dots or CDs [82]. CDs constitute a fascinating class of luminescent carbogenic nanomaterial having sizes below 10 nm with an outer shell composed of oxygen or other heteroatom rich functional groups and an inner core rich in  $sp^2$  hybridized carbon atoms [83-87]. Analogous to semiconductor QDs, these surface-passivated CDs display size and wavelength-dependent luminescence properties, resistance to photobleaching, facile bio-conjugation, etc [83-87]. These CDs combine several favourable attributes of traditional semiconductor-based QDs without incurring the burden of intrinsic toxicity, elemental scarcity, tedious and costly synthetic procedures. There have been several explanations for the origin of the optical properties of CDs [85-94]. Some studies have stated that the luminescence of CD is due to the electronic transition within the core, whereas other reports have linked the emission to surface-localized states. Also, the characteristic excitation-dependent PL properties of CDs have been explained by several researchers on the basis of either distribution of different

surface chromophores or sizes. Till now, the origin of intense wavelength-dependent PL properties of CD is a matter of debate and not yet entirely understood.



**Scheme 1.5.** Schematic illustration of CD preparations via “bottom-up” and “top-down” approaches.

The fabrication of CDs can generally be classified into two kinds of approaches, “bottom-up” and “top-down” (Scheme 1.5). Bottom-up approaches fabricate CDs from molecular precursors such as citric acid, sucrose, and glucose through microwave synthesis, thermal decomposition, hydrothermal treatment, template-based routes, and plasma treatment [95-100]. Top-down approaches synthesize CDs from macroscopic carbon structures, such as graphite, activated carbon, and carbon nanotubes by treatments like arc-discharge, laser ablation, electrochemical oxidation, chemical oxidation, and ultrasonic synthesis [86, 88, 100-102]. For example, Park et al. (2014) reported a large-scale “green solution” for the synthesis of CDs having uniform spherical shape with an average size of 4.6 nm, using waste food as

carbon sources under ultrasound treatment at room temperature [102]. Recently, Ding et al. (2016) hydrothermally synthesized CDs having different degree of oxidation with tunable PL and a quantum yield of upto 35% in water and separated these CDs via silica column chromatography [97]. The separated CDs displayed bright and stable luminescence from blue to red under a single-wavelength UV light exhibiting high optical uniformity. In the recent years, CDs owing to their outstanding merits in terms of luminescence, stability, biocompatibility, and low cost have found potential applications in numerous important fields such as biosensing, bioimaging, drug delivery, photocatalysis, and optoelectronics [83, 84, 88, 101-105]. In this thesis, the effect of three different sized citrate-capped Ag NPs on the PL properties of CDs has been illustrated.

### **1.5. Influence of Metal NPs and NCs on the Nearby Fluorophore**

Metal NPs show broad LSPR band due to collective oscillation of conduction electrons upon interaction with light, whereas ultrasmall metal NCs display size-dependent bright luminescence due to the discrete electronic energy levels. Due to their drastically different optical properties, metal NPs and NCs affect the nearby fluorophore in different ways. The presence of metal NPs either enhances or quenches the luminescence yield of the nearby fluorophore. It is well established that the origin of luminescence enhancement is due to either enhanced electromagnetic field of LSPR at the metal NP surface or an increase in the radiative decay rate of the excited fluorophore near the metal NP [10-13]. It has been observed that metal NP often quenches the fluorescence yield due to nonradiative energy transfer, electron transfer, or by decreasing the radiative rate of the fluorophore [15-20].

## Chapter 1

---

The ultrasmall metal NC having molecule-like properties quenches the luminescence yield of the nearby fluorophore due to either nonradiative energy transfer or electron transfer [21-23]. The radiative ( $k_r$ ) and nonradiative ( $k_{nr}$ ) decay rates of the fluorophore are expressed as [106]:

$$k_r = \frac{\phi_D}{\tau_D} \quad (1)$$

$$k_{nr} = \left( \frac{1-\phi_D}{\tau_D} \right) \quad (2)$$

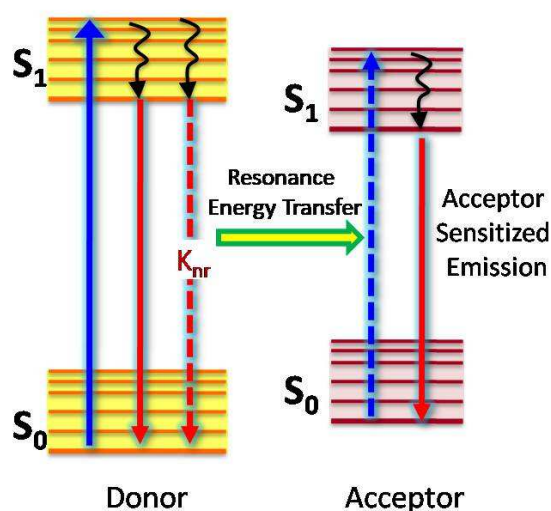
where  $\phi_D$  is the quantum yield and  $\tau_D$  is the average lifetime of the fluorophore.

Several investigations have been performed to understand the highly efficient nonradiative energy transfer from various photoexcited fluorophores to metal NPs and NCs. Since metal NP exhibits broad LSPR band and metal NC shows size-dependent PL properties due to discrete electronic energy levels, both NP and NC quench the nearby photoexcited donor via different mechanisms. The mechanism of excitation energy transfer and the different related theories have been discussed briefly in the next section.

### 1.6. Mechanism of Excitation Energy Transfer (EET)

EET is defined as the nonradiative transfer of excitation energy from a photoexcited donor to a proximal acceptor [106] (Scheme 1.6). The donor is a fluorophore and the acceptor can be another fluorophore of lower excitation energy, a dark quencher, a metal film or a metal NP. The rate of energy transfer depends upon various parameters such as size and shape of the acceptor, the orientation of the donor and acceptor transition dipoles, the distance between donor and acceptor, and the spectral overlap between the emission spectrum of donor and

absorption spectrum of acceptor [106]. Since EET is sensitive to the donor-acceptor spectral properties and the donor-acceptor distance, it is commonly known as the “*spectroscopic ruler*”. Being a sensitive and selective fluorescence technique, it has been widely applied in various fields including photovoltaics, light-emitting diode, sensors, bioimaging, etc [107-110].



**Scheme 1.6.** Jablonski diagram for nonradiative resonance energy transfer.

Energy transfer techniques rely on the measurement of the intensity quenching and/or the lifetime quenching of the donor. The quenching efficiency for a donor-acceptor pair is given by the equation [106]:

$$\phi_{\text{Eff}} = 1 - \frac{\phi_{\text{D-A}}}{\phi_{\text{D}}} = 1 - \frac{\tau_{\text{D-A}}}{\tau_{\text{D}}} \quad (3)$$

where  $\phi_{\text{D-A}}$  and  $\phi_{\text{D}}$  are the quantum yield of the donor in the presence and absence of the acceptor, respectively.  $\tau_{\text{D-A}}$  and  $\tau_{\text{D}}$  are the excited-

state average lifetimes of the donor in the presence and absence of the acceptor, respectively. The rate of energy transfer ( $k_{\text{ET}}$ ) between a donor and acceptor is expressed as [106]:

$$k_{\text{ET}} = \frac{1}{\tau_{\text{D}}} \left( \frac{R_0}{R} \right)^n \quad (4)$$

where  $\tau_{\text{D}}$  is the excited-state average lifetime of the donor in the absence of the acceptor,  $R_0$  is the distance at which efficiency of energy transfer is 50%,  $R$  is the estimated separation distance between the donor and acceptor, and  $n$  is the power dependence of the theory used to describe  $R_0$ . Both  $R_0$  and  $n$  are highly dependent on the nature of the donor and acceptor. Due to the strong distance dependence of  $k_{\text{ET}}$ , EET has found various applications in structural biology to measure distances and to monitor structural or conformational changes in biomolecules.

Numerous models such as Förster resonance energy transfer (FRET), Gersten-Nitzan (G-N), Chance, Prock, Silbey-Kuhn (CPS-Kuhn), and nanometal surface energy transfer (NSET) have been developed in the last few decades to understand the mechanism of energy transfer from photoexcited donors to metal NPs and NCs [15-17, 111, 112]. A brief description of these theories, their assumptions, and limiting conditions are provided in the next section.

### 1.6.1. Förster Resonance Energy Transfer (FRET)

In 1948, Theodor Förster quantum mechanically described the theory of FRET occurring between two closely juxtaposed molecules [111]. FRET is defined as the nonradiative energy transfer from a photoexcited donor (D) to an acceptor (A) via dipole-dipole

interactions. It is a through space distance-dependent interaction in which the excited donor transfers its excitation energy to an acceptor molecule nonradiatively. The rate of FRET depends upon various factors such as the extent of spectral overlap, the relative orientation of the transition dipoles and the center-to-center distance between the donor and acceptor molecules (Scheme 1.7) [106, 111].

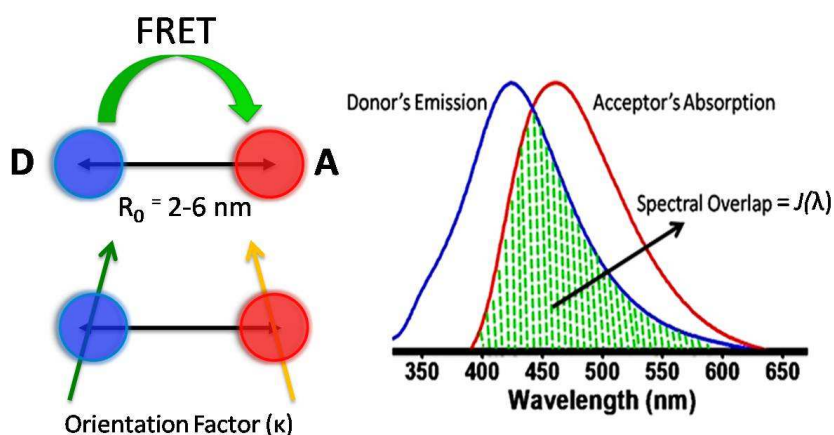
FRET invokes the Fermi Golden Rule in the dipole approximation of energy transfer. The Golden Rule approximation relates the energy transfer rate ( $k_{\text{ET}}$ ) to a product of the interaction elements of the donor ( $F_{\text{D}}$ ) and acceptor ( $F_{\text{A}}$ ),  $k_{\text{ET}} \approx F_{\text{D}}F_{\text{A}}$ . These interaction elements can be simplified such that their separation distance ( $R$ ) dependencies are sole functions of their geometric arrangement. For single dipoles,  $F \approx 1/R^3$ , for a 2D dipole array,  $F \approx 1/R$ , and for a 3D dipole array,  $F = \text{constant}$  such that the power of the distance factor decreases as the dimension increases [17]. FRET, which consists of two single dipoles, is easily derived from this rule such that  $k_{\text{FRET}} \approx F_{\text{D}}F_{\text{A}} \approx (1/R^3)(1/R^3) \approx 1/R^6$ . Therefore, the rate of FRET ( $k_{\text{FRET}}$ ) for a donor-acceptor pair is given by the following equation:

$$k_{\text{FRET}} = \frac{1}{\tau_{\text{D}}} \left( \frac{R_0}{R} \right)^6 \quad (5)$$

where  $\tau_{\text{D}}$  is the excited state average lifetime of the donor in the absence of the acceptor,  $R$  is the separation distance between donor and acceptor, and  $R_0$  is the distance at which the 50% FRET is observed which is known as the Förster distance ( $R_0$ ).  $R_0$  is a function of the oscillator strengths of the donor and acceptor molecules, their mutual energetic resonance, and the vector addition of their dipoles. The Förster distance ( $R_0$ ) can be expressed as

$$R_0 = [(8.8 \times 10^{-25})(\kappa^2 \eta^{-4} \phi_D J(\lambda))]^{1/6} \quad (6)$$

where  $\kappa^2$  is the orientation factor of the transition dipoles of the donor and the acceptor,  $\eta$  is the refractive index of the medium,  $\phi_D$  is the quantum yield of the donor and  $J(\lambda)$  is the spectral overlap integral between the donor emission and the acceptor absorption spectrum. The value of  $\kappa^2$  depends on the relative orientation of the donor and acceptor dipoles. For randomly oriented dipoles,  $\kappa^2 = 2/3$ , and it varies between 0 and 4 for the cases of orthogonal and parallel dipoles, respectively.



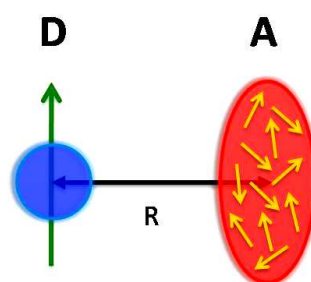
**Scheme 1.7.** *Important parameters on which FRET depends.*

FRET is only useful for measuring donor-acceptor intermolecular distances in between 1 and 10 nm [113, 114]. This range is sufficient for observing dynamic interactions between proteins, nucleic acids, and cell membranes. Recently, FRET has also been applied to explain the luminescence quenching of various photoexcited donors such as dyes, semiconductor QDs, and CDs in the presence of metal NPs. But the assumption of a metal NP to behave as a single

point dipole is debatable [115]. Therefore, by changing the acceptor from a point dipole to a metal NP, the  $1/R^6$  distance dependent term alters giving larger abrupt donor-acceptor separation distances beyond the FRET limit [116, 117]. A number of alternative energy transfer models such as G-N, CPS-Kuhn, and NSET have been developed to treat an oscillator in the metal NP near field, in an attempt to account for the quenching of photoexcited molecules in the presence of metal NPs.

### 1.6.2. Gersten-Nitzan (G-N) model

The GN-model provides one of the first theoretical treatments for a molecular dipole in the presence of either a metallic sphere or spheroid [16, 118]. In this model, the NP is assumed to consist of a volume of uncoupled dipoles (Scheme 1.8). This assumption results in  $1/R^6$  distance dependence as the donating dipole couples to a single dipole in the volume of oscillators present in the metal NP. Since the volume of dipoles has all possible orientations, the orientation factor is no longer required.



**Scheme 1.8.** Schematic illustration of fluorophore-metal NP donor-acceptor system by G-N theory.

## Chapter 1

---

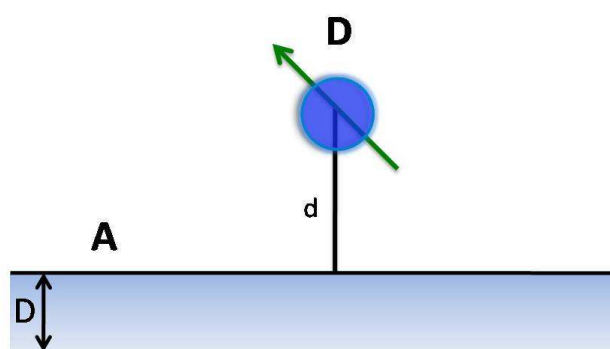
The fluorophore is placed at a distance  $R$  from the center of a spherical NP of radius  $r$ , such that  $r \ll \lambda$ . The assumption of the NP being much smaller than the wavelength of light ( $\lambda$ ) allows for the problem to be treated within the electrostatic theory. The assembly of the NP with the fluorophore placed in its vicinity is treated as one complete system with a dipole moment which has contributions from both the metal NP and the fluorophore. This is considered to be more appropriate because of the generation of the induced dipole due to the electric field of the metal NP. The induced dipole causes an image enhancement effect which is prominent at distances closer to the metal surface. The field of the NP affects both the  $k_r$  and  $k_{nr}$ . If the changes in the  $k_r$  are ignored and only nonradiative energy transfer is the dominant process, then the distance ( $R_0^{GN}$ ) corresponding to 50% energy transfer given by the following equation [16, 119]:

$$R_0^{GN} = \left[ 2.25 \cdot \frac{c^3}{\omega_D^3} \cdot \phi_D \cdot r^3 \cdot \frac{(\epsilon_1 + 2)^2 + \epsilon_2^2}{|\epsilon_2|^2} \right]^{1/6} \quad (7)$$

where  $\omega_D$  is the frequency of the donor,  $\phi_D$  is the quantum yield of the donor,  $r$  is the radius of the metal NP,  $\epsilon_1$  and  $\epsilon_2$  are the real and imaginary components of the dielectric constant of the metal and  $c$  is the speed of light. This equation is derived under the assumption that there is no change in the radiative rate of the donor molecule in the presence of the metal NP and therefore no enhancement effects. Overall, this model predicted more efficient quenching than FRET because the increased number of accepting dipoles increased the probability of coupling. But it failed to predict both the rates of energy transfer as well as the dependence upon the distance between the emitter and NP surface [20, 117].

### 1.6.3. CPS-Kuhn model

In 1970, Kuhn explained the energy transfer from a dipole to a thin metal film [112]. His theory deals with the quenching of an emitting fluorophore when placed close to a thin metal film and is applicable when the thickness of the film ( $D$ ) is less than the distance of the fluorophore from its surface ( $d$ ) (Scheme 1.9). The emitter is again treated as a simple harmonic oscillator and the metal film is assumed to be a perfect mirror with a reflectivity of unity. The emitting field from the donor induces oscillations in the acceptor and this induced field in the acceptor travels back to the donor and slows down the acceptor oscillator. Thus, it can be said that the quenching in Kuhn theory is a retardation effect on the emitter due to the acceptor. The theory also explains the quenching of a quadrupole emitter by a metal thin film acceptor.



**Scheme 1.9.** Schematic representation of CPS-Kuhn approximation for a fluorophore-metal thin film as the donor-acceptor pair.

However, it was later found that the Kuhn's theory greatly over-estimated the extent of energy transfer and it was modified by Chance, Prock, and Silbey which is now known as CPS-Kuhn model. The CPS-

## Chapter 1

---

Kuhn model was developed to describe thin films below the electron mean free path and assumes that the metal thin film is primarily an absorber of the excited-state oscillator energy in the near field through the formation of an image dipole. In the CPS-Kuhn model, the surface is treated as a strongly correlated collection of oscillators resulting in  $d^{-4}$  distance dependence. According to this model, the distance ( $d_0^{\text{CPS-Kuhn}}$ ) at which the probability of nonradiative energy transfer is 50% is given by the following equation [15, 12 119]:

$$d_0^{\text{CPS-Kuhn}} = \frac{\alpha\lambda}{\eta} (A\phi)^{1/4} \left( \frac{\eta_r}{2\eta} \left( 1 + \frac{\epsilon_1^2}{|\epsilon_2|^2} \right) \right)^{1/4} \quad (8)$$

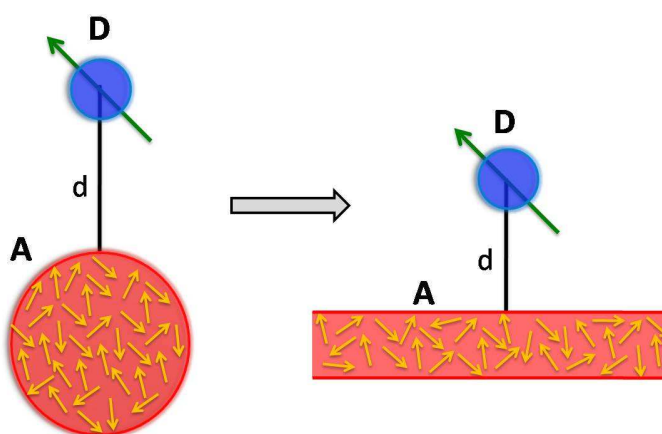
where the orientation of the donor to the metal plasmon vector is  $\alpha$ , which takes a value of  $(1/4\pi) \cdot (9)^{1/4}$  for a dipole oriented perpendicularly to the metal surface while it takes a value of  $(1/4\pi) \cdot (9/2)^{1/4}$  when the dipole is aligned parallel to the metal surface.  $\lambda$  is the emission wavelength maximum of the donor,  $\eta$  is the refractive index of the medium,  $A$  is the absorptivity of the thin film mirror,  $\phi_D$  is the quantum yield of the donor,  $\eta_r$  is the refractive index of the metal,  $\epsilon_1$  is the dielectric function, and  $\epsilon_2$  is the complex dielectric function of the metal which can be decomposed into the real and imaginary components ( $\epsilon_2 = \epsilon_2' + i\epsilon_2''$ ). The CPS-Kuhn expression is only appropriate for a thin film with mirror-like behavior where the image dipole depth is defined by the penetration depth of the oscillator dipole, which is dependent on the metal complex dielectric function ( $\epsilon_2$ ) and absorptivity ( $A$ ) at the oscillator frequency [15, 120].

It has been reported that the G-N model developed for spherical metal NP predicting  $R^{-6}$  distance dependence failed to predict

separation distance-dependent quenching [117]. The failure of G-N model was believed to reflect the inability to accurately predict the observed rates for the fluorophore when the NP has insignificant scattering contributions. In the NP, neither an infinite surface nor a bulk volume is a correct model and thus the CPS-Kuhn model, although validated in thin films, over-predicted the interaction strength of NP with the dipole [112, 114, 120, 121]. Hence, there was a requirement of the incorporation of size-dependent electronic properties of the metal NPs in the quasi-static CPS-Kuhn model [112, 115, 122].

### 1.6.4. Nanometal Surface Energy Transfer (NSET)

The NSET model is an extension of the theory proposed by Persson and Lang in the year 1981 where the FL quenching of an oscillating dipole on a metal surface was illustrated (Scheme 1.10) [17].



**Scheme 1.10.** NSET model for the fluorophore-metal NP as the donor-acceptor system.

## Chapter 1

---

The metal is treated within the jellium approximation. The frequency of oscillation of the dipole ( $\omega_D$ ) is smaller than the plasma frequency ( $\omega_p$ ) of the metal as only in this region the conduction electrons of the metal can respond adiabatically to the slowly varying external field and adjust to the instantaneous static configuration. The theory explains the effects of the metal surface on the emitter in the long distance range such that  $D \gg \omega_F / \omega_D k_F$ , where  $\omega_F$  is the Fermi frequency and  $k_F$  is the Fermi wave-vector for the metal. The theory also assumes that the surface of the metal NP is going to affect the emitter differently than the volume, therefore the effects of surface and core electrons are considered separately. This makes the theory extremely applicable to the metal NP quenching as the surface and core electrons behave differently. The rate of surface quenching is a function of the electron gas density parameter while the volume damping is a function of the bulk dielectric function arising from the scattering of the electrons against the phonons, impurities etc.

The generalized damping rate can be written as,

$$k_{ET} = \frac{\mu^2}{4 d^3 \hbar} \cdot F \quad (9)$$

where  $\mu$  is the dipole moment of the emitter,  $d$  is the distance from the center of the emitter to the metal NP surface and  $F$  is the surface or volume dependent quenching term such that,

$$F_{Surface} = 1.2 \frac{\omega_D}{\omega_F} \cdot \frac{1}{k_F d} \quad (10)$$

and,

$$F_{Volume} = 3 \frac{\omega_D}{\omega_F} \cdot \frac{1}{k_F l} \quad (11)$$

The volume quenching is thus a function of  $1/d^3$  and the mean free path ( $l$ ) for the metal while the surface quenching is a  $1/d^4$  dependent phenomenon. For very small particles where the surface and the volume are indistinguishable, only surface quenching is observed while for large particles which have a well-formed surface and a distinguishable volume, surface quenching is observed at shorter distances while volume quenching plays a dominant role at longer distances. Also, for metals with extremely long mean free paths such as the noble metals, surface quenching is the dominant player at distances as long as 30 nm [122]. With these approximations and results the rate of NSET ( $k_{\text{NSET}}$ ) is given by the following equation:

$$k_{\text{NSET}} = 0.225 \frac{c^3}{\omega_D^2 \omega_F k_F d^4} \frac{\phi_D}{\tau_D} \quad (12)$$

where  $c$  is the speed of light,  $\phi_D$  is the quantum yield of the donor,  $\omega_D$  is the angular frequency of the donor,  $\omega_F$  is the angular frequency of the bulk metal,  $k_F$  is the Fermi wave-factor for the bulk metal,  $\tau_D$  is the excited state lifetime of the donor in the absence of acceptor and  $d$  is the distance from the centre of the donor to the surface of metal NP. This can be expressed in more simplified form with measurable parameters [121, 122]:

$$k_{\text{NSET}} = \frac{1}{\tau_D} \left( \frac{d_0}{d} \right)^4 \quad (13)$$

where  $d_0$  is the separation distance between the center of donor and the surface of metal NP at which the energy transfer efficiency is 50%. For the Persson and Lang NSET model, the distance ( $d_0$ ) at which donor display equal probabilities for energy transfer and spontaneous emission is expressed as [15, 17, 120, 121]:

$$d_0 = \left(0.225 \frac{c^3 \phi_D}{\omega_D^2 \omega_F k_F}\right)^{1/4} \quad (14)$$

Several reports have demonstrated that the nonradiative EET from photoexcited donors to metal NPs is best modeled by the NSET, showing a fair correlation between the experimental and theoretical results [114-116, 121].

### 1.7. Resonance EET from Photoexcited Donors to Metal NPs and NCs

Earlier, the resonance EET has been studied in simple dye-based donor-acceptor systems having significant spectral overlap between the emission spectrum of donor dye and the absorption spectrum of the acceptor dye. This spectral overlap criterion for an efficient EET led to the limited choice of donor-acceptor pairs in dye-based energy transfer systems. However, this limitation has been overcome by the development of new quantum confined nanomaterials showing size-dependent emission properties such as QDs, CDs, and metal NCs [43, 44, 79, 80, 86, 87, 92, 94]. The development of these nanomaterials has extended the applications of resonance EET due to their extremely tunable and size-dependent optical properties spanning from UV to near IR region with high quantum yields. Over the past few years, several reports have illustrated the EET involving photoexcited semiconductor and carbon-based QDs as donors and metal NPs and NCs as acceptors [18, 21, 107, 108, 114-116, 121-123]. The EET from photoexcited QDs and CDs to ultrasmall metal NCs follows the FRET mechanism, as these are treated as point dipoles due to their smaller sizes. However, the EET from photoexcited donor to nearby metal NP (2-100 nm) is best described by NSET rather than FRET mechanism.

Extensive studies have been performed to demonstrate the mechanism and dynamics of the quenching of photoexcited fluorophores in the close proximity of metal NPs and NCs [18, 21, 114-116, 121-124]. For example, Singh et al. (2010), directly correlated spectral overlap between the LSPR of a 2 nm gold nanoparticle (Au NP) and emission spectra of the different donor dyes ( $\lambda_{em} = 520-780$  nm) as well as the separation distance with the magnitude of FL quenching of different dyes by Au NPs [115]. The dyes and Au NPs were separated by synthetic DNA sequences of different lengths. They compared their experimental results with the theoretical predictions from classical FRET, GN, CPS-Kuhn, and NSET models for energy transfer from different photoexcited dye to Au NP. Comparison of the models suggested that the NSET model best described the observed spectral overlap dependent quenching of donor dyes by a 2 nm Au NP, whereas CPS-Kuhn over-predicts the distance dependence, and FRET as well as GN under-predict the distance. Recently, Liu et al. (2015) demonstrated the NSET based biosensor for selective fluorimetric and colorimetric detection of hyaluronidase using amino-functionalized CDs as donor and hyaluronate stabilized AuNPs as acceptor [125].

In another study, Xavier et al. (2010) utilized the protein lactoferrin as a stabilizer to synthesize AuNCs and demonstrated the EET from the fluorescent protein residues to the clusters using FRET [124]. Similarly, Pu et al. (2011) reported FRET between blue-fluorescent conjugated oligomer-substituted polyhedral oligomeric silsesquioxane (POSSFF) and red-emitting bovine serum albumin (BSA)-encapsulated gold NCs (Au NCs) [126]. Subsequently, they demonstrated the mercury-ion sensing both in solution and in cell. Recently, Russell et al. (2015) estimated a tryptophan-AuNC donor-

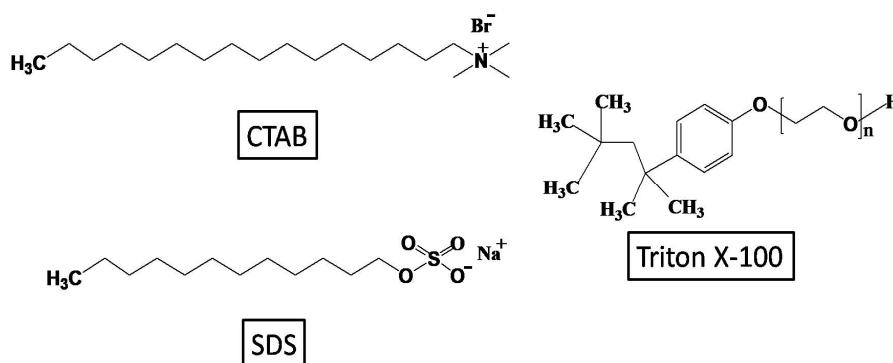
acceptor separation distance using FRET for human serum albumin-(HSA) stabilized AuNCs [127]. This information was then used to correlate where the clusters were nucleating on the protein structure. In this thesis, the PL quenching of Si QD and CD in the presence of citrate-capped Ag NPs showing broad LSPR bands has been rationalized on the basis of NSET theory. In both the cases, the estimated Förster distances ( $R_0$ ) were beyond the detection limit of FRET theory, signifying that the EET from photoexcited Si QD and CD to citrate-capped Ag NPs does not follow conventional FRET process. On the other hand, it has been demonstrated that the FL quenching of DAPI in the presence of ultrasmall luminescent Ag NC is due to the FRET from photoexcited DAPI to Ag NC.

Since EET is sensitive to the donor-acceptor distance and spectral properties, it has been extensively studied in various microheterogeneous environments such as micelles, polymers, biomolecules, etc. to probe the structure and dynamics of chemically and biologically relevant systems [21, 113-115, 119, 122, 124-132]. These microheterogeneous environments have been illustrated as excellent bio-mimetic. The energy transfer studies in such environments extend the applicability of FRET and NSET techniques in various important fields such as sensing, molecular imaging, drug delivery systems, etc [21, 110, 113, 123-125, 127, 128, 131]. A brief description of the various microheterogeneous environments such as surfactant assemblies, polymer, and DNA followed by illustration of FRET and NSET studies in these environments has been provided in the next section.

## 1.8. Microheterogeneous Environments

### 1.8.1. Surfactant Assemblies

The surfactant is an amphiphilic molecule containing the nonpolar hydrocarbon tail and the polar head group. The hydrocarbon tail of a surfactant can be linear, branched or aromatic and the polar head group can be neutral or ionic depending upon the charge it carries. Surfactants are classified based on the charge of the polar head group. The non-ionic surfactant contains the neutral polar head group, whereas polar head groups with net positive and negative charge are known as cationic and anionic surfactants, respectively. If the polar head group contains both, the negatively and positively charged head group, it is called as the zwitterionic surfactant. The chemical structures of the cationic surfactant cetyltrimethylammonium bromide (CTAB), anionic surfactant sodium dodecyl sulfate (SDS), and neutral surfactant triton X-100 (TX-100) are presented in scheme 1.11.



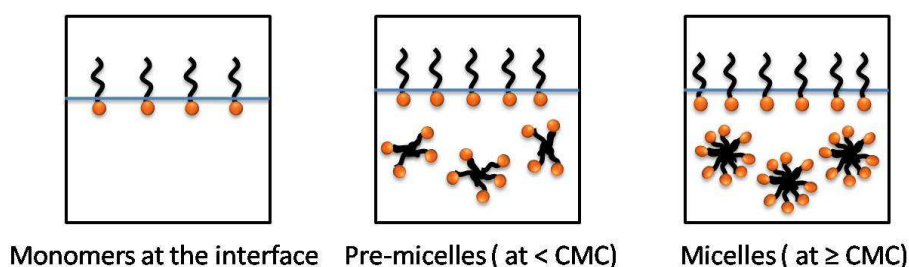
**Scheme 1.11.** The chemical structures of CTAB, SDS, and TX-100.

At very low concentrations, the surfactant molecules due to their amphiphilic nature form a monolayer at the air-water interface (Scheme 1.12) [133, 134]. The polar head groups remain in the

## Chapter 1

---

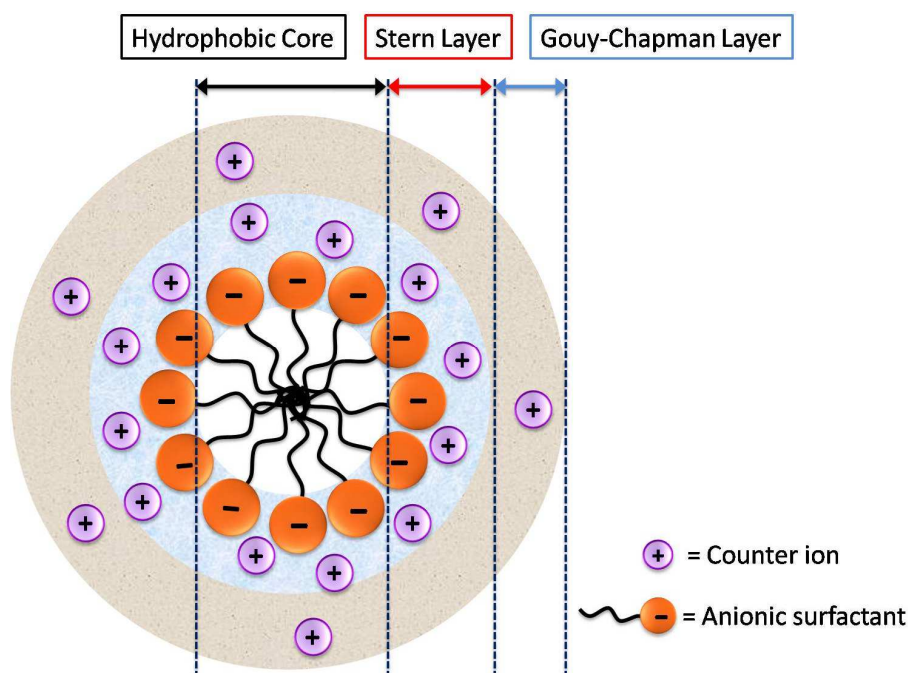
aqueous phase with hydrophobic tails pointing towards the air. Addition of further surfactant molecules results into the formation of pre-micellar aggregates in the solution, followed by the formation of spherical aggregates at or beyond the critical micelle concentration (CMC) (Scheme 1.12) [133, 134]. These spherical aggregates are known as micelles, in which the hydrophobic tails form the core of the aggregate and the hydrophilic heads are in contact with the surrounding aqueous medium. The CMC of above-mentioned surfactants CTAB, SDS, and TX-100 is 1, 8, and 0.22 mM, respectively..



**Scheme 1.12.** Representation of the surfactant assemblies in solution.

The physicochemical properties and structure of micelles are strongly dependent on the nature and size of polar head groups, the length of the hydrocarbon chains, type of counterion, electrolyte addition, solution pH, and temperature [133-137]. The number of surfactant molecules forming a micelle is known as the aggregation number (N). The aggregation number of the above-mentioned surfactants CTAB, SDS, and TX-100 is 61, 64, and 140, respectively. The typical diameter of ionic micelles ranges from 3 to 5 nm, depending on the nature of surfactants. Scheme 1.13 shows the structure of the anionic micelle which consists of a hydrophobic core composed of the hydrocarbon chains of the surfactant molecules, a

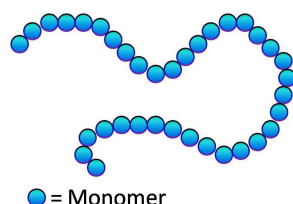
Stern layer surrounding the core, and a Gouy-Chapman layer surrounding the Stern layer.



**Scheme 1.13.** Schematic illustration of the structure of an anionic micelle.

### 1.8.2. Polymer

The polymer is a long-chain molecule which is prepared via polymerization of several small molecules which are known as monomers (Scheme 1.14) [138]. Polymers are classified in number of ways based on their origin, synthetic methods, thermal response, line structure, charge, tacticity, crystallinity, applications, and physical properties [138].



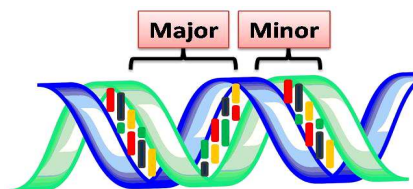
**Scheme 1.14.** *Illustration of a polymer composed of small monomeric units.*

The well-known examples of polymers include polyethylene, proteins, polysaccharides, methyl cellulose, nylons, resins, rubbers, etc [138]. Due to the recent technological advancements, the applications of polymers have extended from everyday materials and processes to various complex and challenging fields such as drug delivery, bio-sensing, biomedical devices, optoelectronics, etc [139-142].

### 1.8.3. Deoxyribonucleic acid (DNA)

DNA consists of two long polynucleotide chains, which are composed of monomeric units known as nucleotides [143]. A nucleotide is made up of a sugar (deoxyribose), a phosphate group, and one of four nitrogenous bases: adenine (A), thymine (T), guanine (G) or cytosine (C). The nucleotides are joined to one another in a chain by covalent bonds between the sugar of one nucleotide and the phosphate of the next, resulting in an alternate sugar-phosphate backbone. The nitrogenous bases of the two separate polynucleotide strands are bound together, according to base pairing rules (A with T, and C with G), with hydrogen bonds to make double-stranded DNA (Scheme 1.15) [143]. When the strands are far apart, major grooves are formed and when the strands are closer, minor grooves are formed (Scheme 1.15). Major grooves are wider than minor grooves which

mean that the edges of the bases are more accessible in the major groove than in the minor groove.



**Scheme 1.15.** Schematic representation of a double-stranded DNA.

According to Ortiz et al. (2011), there are three ways a molecule can bind to double-stranded DNA, namely intercalation, groove binding and external electrostatic binding [144]. Intercalation involves insertion of the planar molecule between the DNA base pairs. In groove binding, the molecule resides in the major or minor groove via hydrophobic interaction and/or hydrogen bonding. The external electrostatic binding leads to the binding of the molecule with the DNA sugar-phosphate backbone via electrostatic interaction. The information regarding these binding modes of DNA with various biologically important molecules is vital for several important fields such as medical diagnosis, cellular imaging, DNA quantification, etc [145-149].

### 1.9. FRET and NSET in Microheterogeneous Environments

Over the past few decades, several investigations have been executed on the structural and photophysical aspects of molecules entrapped in microheterogeneous environments due to the promising role of confined assemblies in numerous chemically and biologically important systems [149-152]. Recently, due to the explicit distance dependence of EET, it has been extensively studied in various

microheterogeneous environments [21, 113-115, 119, 122, 124-132]. For example, Mondal et al. (2013) reported a very simple approach for the measurement of the surfactant bilayer thickness by using FRET as a tool, where carbon NP acted as a donor and the different dyes as acceptors. The authors proposed that the synthesized core-shell carbon NPs may have applications in bio-nanotechnology and such a carbon NP-dye conjugate can be utilized as a drug carrier and can be mapped through fluorescence imaging [153]. Similarly, Mandal et al. (2011) synthesized Au NPs into the surface cavities of P123 micellar assemblies together with the fluorescent dye molecules and investigated NSET from confined donor dye to metal NP [122]. They also demonstrated a comparative study on quenching efficiencies of different dyes (coumarin 480, coumarin 343, and rhodamine 6G) having different locations inside micelles in order to probe different regions of Au-P123 hybrid nanospheres. They concluded that their results can be helpful to further explore the potential applicability of their energy transfer system in sensing and medicinal chemistry.

In another study, Kundu et al. (2014) designed organic-inorganic light harvesting assemblies in which highly efficient FRET from CdTe quantum dots (donors) to Nile Red dye (acceptor) encapsulated poly(methyl methacrylate) (PMMA) polymer NPs [154]. The negatively charged thioglycolic acid capped CdTe QDs were attached to the surface of the polymer NPs by electrostatic interaction. The authors suggested that their fundamental investigation of FRET from the surface to the core of the assemblies may find applications in artificial light harvesting systems. Recently, Xiao et al. (2013) demonstrated distance-dependent FRET from different photoexcited donors to Ag NCs by designing a hybridized DNA duplex model [21].

The separation distance between the donor and Ag NC was adjusted by changing the DNA duplex model and the number of hybridized pairs. They also employed their FRET-based energy transfer system for biosensing applications. In some other studies, Strouse and co-workers (2005, 2006 and 2013) investigated the fluorescence behavior of various molecular dyes in the presence of different-sized Au NPs [118, 115, 116, 121]. The separation distance between the dyes and Au NPs was varied using the double-stranded DNA of different lengths. They demonstrated that quenching behavior of dyes was consistent with  $1/d^4$  separation distance in accordance with the NSET model. They proposed that NSET from a dipole to a metal nanosurface may provide a new paradigm for the design of optical-based molecular ruler strategies at larger distances desirable for diverse biological applications.

In this thesis, along with the demonstration of the mechanism and dynamics of EET from various photoexcited donors to Ag NP and Ag NC, the influence of microheterogeneous environments of CTAB, SDS, poly(diallyldimethylammonium chloride) (PDADMAC) and calf thymus DNA (CT-DNA) on the efficiency of EET has also been illustrated.

### **1.10. Organization of Thesis**

The overall objective of the work described in the thesis is to unveil the fundamental mechanism and dynamics of resonance EET from various photoexcited donors such as Si QDs, CDs, and DAPI to Ag NPs and Ag NCs. Moreover, the influence of various microheterogeneous environments such as surfactant assemblies,

## ***Chapter 1***

---

polymer, and DNA on the efficiency of energy transfer has also been illustrated.

**Chapter 1** discusses the unique optical properties of Ag NP, Ag NC, and quantum dots such as Si QD and CD. The effect of metal NPs and NCs on the PL properties of various fluorophores has been briefly explained. The mechanism and dynamics of various EET theories have been discussed in detail. Finally, the importance of spectroscopic nanorulers such as FRET and NSET, in numerous biologically relevant microheterogeneous environments has been illustrated.

**Chapter 2** includes details of the chemicals and complete synthetic procedures of citrate-stabilized Ag NP, dihydrolipoic acid-capped Ag NC, allylamine-functionalized Si QD, and CD. A brief description of the sample preparations and experimental techniques used to complete the entire work of this thesis has been provided here.

**Chapter 3** demonstrates the influence of Ag NP on the PL properties of water-dispersed biocompatible Si QD in the absence and presence of CTAB. The mechanism and dynamics of nonradiative EET from Si QD to Ag NP has been illustrated and the influence of CTAB on this nonradiative EET has been explored.

**Chapter 4** investigates the effect of three different sized citrate-capped Ag NPs having distinct LSPR bands on the PL properties of the nearby CDs. The dynamics of the PL quenching of CDs in the presence Ag NPs has been quantitatively discussed, establishing the mechanism of nonradiative EET and demonstrating the influence of the size of Ag NP on the efficiency of EET.

## ***Chapter 1***

---

**Chapter 5** addresses the fundamental mechanism and dynamics behind the FL quenching of DAPI by DHLA-capped Ag NCs and demonstrates the influence of cationic water-soluble PDADMAC and CT-DNA on the FL quenching.

**Chapter 6** illustrates the specific concentration-dependent interaction between DAPI and SDS and investigates the influence of surfactant assemblies of SDS on the FRET between DAPI and Ag NC.

**Chapter 7** concludes the work done in this thesis along with their scope for future applications.

### 1.11. References

1. Stewart M. E., Anderton C. R., Thompson L. B., Maria J., Gray S. K., Rogers J. A., Nuzzo R. G. (2008), Nanostructured plasmonic sensors, *Chem. Rev.*, 108, 494-521. (DOI: 10.1021/cr068126n)
2. Ozbay E. (2006), Plasmonics: Merging photonics and electronics at nanoscale dimensions, *Science*, 311, 189-193. (DOI: 10.1126/science.1114849)
3. Polman A. (2008), Plasmonics applied, *Science*, 322, 868-869. (DOI: 10.1126/science.1163959)
4. Duyne R. P. V. (2004), Molecular plasmonics, *Science*, 306, 985-986. (DOI: 10.1126/science.1104976)
5. Jin R., Zeng C., Zhou M., Chen Y. (2016), Atomically precise colloidal metal nanoclusters and nanoparticles: fundamentals and opportunities, *Chem. Rev.*, 116, 10346-10413 (DOI: 10.1021/acs.chemrev.5b00703)
6. Eustis S., El-Sayed M. A. (2006), Why gold nanoparticles are more precious than pretty gold: Noble metal surface plasmon resonance and its enhancement of the radiative and nonradiative properties of nanocrystals of different shapes, *Chem. Soc. Rev.*, 35, 209-217 (DOI: 10.1039/b514191e)
7. Goswami N., Yao Q., Luo Z., Li J., Chen T., Xie J. (2016), Luminescent metal nanoclusters with aggregation-induced emission, *J. Phys. Chem. Lett.*, 7, 962-975 (DOI: 10.1021/acs.jpcclett.5b02765)

8. Kreibig U., Vollmer M. (1995), Optical properties of metal clusters, Springer, Berlin, Germany (ISBN: 978-3-662-09109-8)
9. Zhen J., Nicovich P. R., Dickson R. M. (2007), Highly fluorescent noble-metal quantum dots, *Annu. Rev. Phys. Chem.*, 58, 409-431 (DOI : 10.1146/annurev.physchem.58.032806.104546)
10. Lakowicz J. R. (2005), Radiative decay engineering 5: Metal-enhanced fluorescence and plasmon emission, *Anal. Biochem.*, 337, 171-194. (DOI : 10.1016/j.ab.2004.11.026)
11. Ray K., Badugu R., Lakowicz J. R. (2007), Sulforhodamine adsorbed Langmuir-Blodgett layers on silver island films: Effect of probe distance on the metal-enhanced fluorescence, *J. Phys. Chem. C*, 111,7091–7097. (DOI: 10.1021/jp067635q)
12. Thomas K. G., Kamat P. V. (2000), Making gold nanoparticles glow: Enhanced emission from a surface-bound fluorophore, *J. Am. Chem. Soc.*, 122, 2655-2656. (DOI: 10.1021/ja9941835)
13. Tovmachenko O. G., Graf C., Heuvel D. J. V. D., Blaaderen A. V., Gerristen H. C. (2006), Fluorescence enhancement by metal core/silica-shell nanoparticles, *Adv. Mater.*, 18, 91-95. (DOI: 10.1002/adma.200500451)
14. Chen Y., Munechika K., Ginger D. S. (2007), Dependence of fluorescence intensity on the spectral overlap between fluorophores and plasmon resonant single silver nanoparticles, *Nano Lett.*, 7, 690-696. (DOI: 10.1021/nl062795z)
15. Chance R. R., Prock A., Silbey R. (1978) Molecular fluorescence and energy transfer near interfaces. In: Prigogine I., Rice S. A. (Eds.),

## Chapter 1

---

Adv. Chem. Phys., 37, John Wiley & Sons, Inc., Hoboken, NJ, USA, 1-65. ( ISBN: 9780471034599)

16. Gersten J. I., Nitzan A. (1985), Photophysics and photochemistry near surfaces and small particles, Surf. Sci., 158, 165-189. (DOI: 10.1016/0039-6028(85)90293-6)

17. Persson B. N. J., Lang N. D. (1982), Electron-hole-pair quenching of excited states near a metal, Phys. Rev. B, 26, 5409-5415. (DOI: 10.1103/PhysRevB.26.5409)

18. Yun C. S., Javier A., Jennings T., Fisher M., Hira S., Peterson S., Hopkins B., Reich N. O., Strouse G. F. (2005), Nanometal surface energy transfer in optical rulers, breaking the FRET barrier, J. Am. Chem. Soc., 127, 3115-3119. (DOI: 10.1021/ja043940i)

19. Ghosh S. K., Pal A., Kundu S., Nath S., Pal T. (2004), Fluorescence quenching of 1-methylaminopyrene near gold nanoparticles: Size regime dependence of the small metallic particles, Chem. Phys. Lett., 395, 366-372. (DOI: 10.1016/j.cplett.2004.08.016)

20. Dulkeith E., Morteani A. C., Niedereichholz T., Klar T. A., Feldmann J., Moller M., Gittins D. I. (2002), Fluorescence quenching of dye molecules near gold nanoparticles: Radiative and nonradiative effects. Phys. Rev. Lett., 89, 203002. (DOI: 10.1103/PhysRevLett.89.203002)

21. Xiao Y., Shu F., Wong K.-Y., Liu Z. (2013), Förster resonance energy transfer-based biosensing platform with ultrasmall silver nanoclusters as energy acceptors, Anal. Chem., 85, 8493-8497. (DOI: 10.1021/ac402125g)

22. Banerjee C., Kuchlyan J., Banik D., Kundu N., Roy A., Ghosh S., Sarkar N. (2014), Interaction of gold nanoclusters with IR light emitting cyanine dyes: A systematic fluorescence quenching study, *Phys. Chem. Chem. Phys.*, 16, 17272-17283. (DOI: 10.1039/C4CP02563F)
23. Devadas M. S., Kwak K., Park J.-W., Choi J.-H., Jun C.-H., Sinn E., Ramakrishna G., Lee D. (2010), Directional electron transfer in chromophore-labeled quantum-sized Au<sub>25</sub> clusters: Au<sub>25</sub> as an electron donor, *J. Phys. Chem. Lett.*, 1, 1497-1503. (DOI: 10.1021/jz100395p)
24. Jain P. K., Huang X., El-Sayed I. H., El-Sayed M. A. (2007), Review of some interesting surface plasmon resonance-enhanced properties of noble metal nanoparticles and their applications to biosystems, *Plasmonics*, 2, 107-118. (DOI 10.1007/s11468-007-9031-1)
25. Agnihotri S., Mukherji S., Mukherji S. (2014), Size-controlled silver nanoparticles synthesized over the range 5-100 nm using the same protocol and their antibacterial efficacy, *RSC Adv.*, 4, 3974-3983. (DOI: 10.1039/c3ra44507k)
26. Rycenga M., Cobley C. M., Zeng J., Li W., Moran C. H., Zhang Q., Qin D., Xia Y. (2011), Controlling the synthesis and assembly of silver nanostructures for plasmonic applications, *Chem. Rev.*, 111, 3669-3712. (DOI: 10.1021/cr100275d)
27. Bastús N. G., Merkoçi F., Piella J., Puntès V. (2014), Synthesis of highly monodisperse citrate-stabilized silver nanoparticles of up to 200 nm: Kinetic control and catalytic properties, *Chem. Mater.*, 26, 2836-2846. (DOI: 10.1021/cm500316k)

## Chapter 1

---

28. Ditlbacher H., Hohenau A., Wagner D., Kreibig U., Rogers, M., Hofer F., Aussenegg F. R., Krenn J. R. (2005), Silver nanowires as surface plasmon resonators, *Phys. Rev. Lett.*, 95, 257403. (DOI: 10.1103/PhysRevLett.95.257403)
29. Nie S., Emory S. R. (1997), Probing single molecules and single nanoparticles by surface-enhanced Raman scattering, *Science*, 275, 1102-1106. (DOI: 10.1126/science.275.5303.1102)
30. Zhang J., Fu Y., Lakowicz J. R. (2007), Enhanced Förster resonance energy transfer (FRET) on a single metal particle, *J. Phys. Chem. C*, 111, 50-56. (DOI: 10.1021/jp062665e)
31. Gill R., Tian L., Somerville W. R. C., Ru E. C. L., Amerongen H. V., Subramaniam V. (2012), Silver nanoparticle aggregates as highly efficient plasmonic antennas for fluorescence enhancement, *J. Phys. Chem. C*, 116, 16687-16693. (DOI: 10.1021/jp305720q)
32. Braun E., Eichen Y., Sivan U., Ben-Yoseph G. (1998), DNA-templated assembly and electrode attachment of a conducting silver wire, *Nature*, 391, 775-778. (DOI: 10.1038/35826)
33. Zhang J., Li S., Wu J., Schatz G. C., Mirkin C. A. (2009), Plasmon-mediated synthesis of silver triangular bipyramids, *Angew. Chem. Int. Ed. Engl.*, 48, 7787-7791. (DOI: 10.1002/anie.200903380)
34. Yin B., Ma H., Wang S., Chen S. (2003), Electrochemical synthesis of silver nanoparticles under protection of poly(N-vinylpyrrolidone), *J. Phys. Chem. B*, 107, 8898-8904. (DOI: 10.1021/jp0349031)

35. Pietrobon B., Kitaev V. (2008), Photochemical synthesis of monodisperse size-controlled silver decahedral nanoparticles and their remarkable optical properties, *Chem. Mater.* 2008, 20, 5186-5190. (DOI: 10.1021/cm800926u)
36. Biswal J., Misra N., Borde L. C., Sabharwal S. (2013), Synthesis of silver nanoparticles in methacrylic acid solution by gamma radiolysis and their application for estimation of dopamine at low concentrations, *Rad. Phys. Chem.*, 83, 67-73. (DOI: 10.1016/j.radphyschem.2012.10.003)
37. Ortega-Arroyo L., Martin-Martinez E. S., Aguilar-Mendez M. A., Cruz-Orea A., Hernandez-Pérez I. and Glorieux C. (2013), Green synthesis method of silver nanoparticles using starch as capping agent applied the methodology of surface response, *Starch*, 65, 814-821. (DOI:10.1002/star.201200255)
38. Patil R. S., Kokate M. R., Jambhale C. L., Pawar S. M., Han S. H., Kolekar S. S. (2012), One-pot synthesis of PVA-capped silver nanoparticles their characterization and biomedical application, *Adv. Nat. Sci.: Nanosci. Nanotechnol.*, 3, 015013. (DOI:10.1088/2043-6262/3/1/015013)
39. Sasidharan A., Riviere J. E., Monteiro-Riviere N. A. (2015) Gold and silver nanoparticle interactions with human proteins: Impact and implications in biocorona formation, *J. Mater. Chem. B*, 3, 2075-2082. (DOI:10.1039/C4TB01926A)
40. Wiley B. J., Im S. H., Li Z.-Y., McLellan J. M., Siekkinen A., Xia Y. (2006), Maneuvering the surface plasmon resonance of silver

## Chapter 1

---

nanostructures through shape-controlled synthesis, *J. Phys. Chem. B*, 110, 15666-15675. (DOI: 10.1021/jp0608628)

41. Wiley B. J., Chen Y., McLellan J. M., Xiong Y., Li Z-Y., Ginger D., Xia Y. (2007), Synthesis and optical properties of silver nanobars and nanorice, *Nano Lett.*, 7, 1032-1036. (DOI: 10.1021/nl070214f)

42. Lee P. C., Meisel D. (1982), Adsorption and surface-enhanced Raman of dyes on silver and gold sols, *J. Phys. Chem.*, 86, 3391-3395. (DOI: 10.1021/j100214a025)

43. Zheng J., Nicovich P. R., Dickson R. M. (2007), Highly fluorescent noble-metal quantum dots, *Annu. Rev. Phys. Chem.*, 58, 409-431. (DOI: 10.1146/annurev.physchem.58.032806.104546)

44. Díez I., Ras R. H. A. (2011), Fluorescent silver nanoclusters, *Nanoscale*, 3, 1963-1970. (DOI: 10.1039/c1nr00006c)

45. Linnert T., Mulvaney P., Henglein A., Weller H. (1990), Long-lived nonmetallic silver clusters in aqueous-solution; preparation and photolysis. *J. Am. Chem. Soc.*, 112, 4657-4664. (DOI: 10.1021/ja00168a005)

46. Zheng J., Dickson R. M. (2002), Individual water-soluble dendrimer-encapsulated silver nanodot fluorescence, *J. Am. Chem. Soc.*, 124, 13982-13983. (DOI: 10.1021/ja028282l)

47. Zhang J. G., Xu S. Q., Kumacheva E. (2005), Photogeneration of fluorescent silver nanoclusters in polymer microgels, *Adv. Mater.*, 17, 2336-2340. (DOI: 10.1002/adma.200501062)

48. Shang L., Dong S. J. (2008), Facile preparation of water-soluble fluorescent silver nanoclusters using a polyelectrolyte template, *Chem. Commun.*, 1088-1090. (DOI:10.1039/B717728C)
49. Xu H. X., Suslick K. S. (2010), Sonochemical synthesis of highly fluorescent Ag nanoclusters, *ACS Nano*, 4, 3209-3214. (DOI: 10.1021/nn100987k)
50. Richards C. I., Choi S., Hsiang J. C., Antoku Y., Vosch T., Bongiorno A., Tzeng Y. L., Dickson R. M. (2008), Oligonucleotide-stabilized Ag nanocluster fluorophores, *J. Am. Chem. Soc.*, 130, 5038-5039. (DOI: 10.1021/ja8005644)
51. Petty J. T., Zheng J., Hud N. V., Dickson R. M. (2004), DNA templated Ag nanocluster formation, *J. Am. Chem. Soc.*, 126, 5207-5212. (DOI: 10.1021/ja031931o)
52. Adhikari B., Banerjee A. (2010), Facile synthesis of water-soluble fluorescent silver nanoclusters and Hg(II) sensing, *Chem. Mater.*, 22, 4364-4371. (DOI: 10.1021/cm1001253)
53. Yu J., Patel S. A., Dickson R. M. (2007), In vitro and intracellular production of peptide-encapsulated fluorescent silver nanoclusters, *Angew. Chem., Int. Ed.*, 46, 2028-2030. (DOI: 10.1002/anie.200604253)
54. Guo C. L., Irudayaraj J. (2011), Fluorescent Ag clusters via a protein-directed approach as a Hg(II) ion sensor, *Anal. Chem.*, 83, 2883-2889. (DOI: 10.1021/ac1032403)

## Chapter 1

---

55. Rao T. U. B., Pradeep T. (2010), Luminescent Ag<sub>7</sub> and Ag<sub>8</sub> clusters by interfacial synthesis, *Angew. Chem., Int. Ed.*, 49, 3925-3929. (DOI: 10.1002/anie.200907120)
56. Li L., Guo Q., Li J., Yan W., Leng C., Tang H., Lu Q., Tan B. (2013), Design of a polymer ligand for the one-step preparation of highly stable fluorescent Ag<sub>5</sub> clusters for tissue labelling, *J. Mater. Chem. B*, 1, 3999-4004. (DOI: 10.1039/C3TB20546K)
57. Cathcart N., Kitaev V. (2010), Silver nanoclusters: Single-stage scaleable synthesis of monodisperse species and their chiroptical properties, *J. Phys. Chem. C*, 114, 16010-16017. (DOI: 10.1021/jp101764q)
58. Reed M. A., Randall J. N., Aggarwal R. J., Matyi R. J., Moore T. M., Wetsel A. E. (1988), Observation of discrete electronic states in a zero-dimensional semiconductor nanostructure, *Phys. Rev. Lett.*, 60, 535-537. (DOI: 10.1103/PhysRevLett.60.535)
59. Alivisatos A. P. (1996), Semiconductor clusters, nanocrystals, and quantum dots, *Science*, 271, 933-937 (DOI: 10.1126/science.271.5251.933)
60. Smith A. M., Nie S. (2010), Semiconductor nanocrystals: structure, properties, and band gap engineering, *Acc. Chem. Res.*, 43, 190-200. (DOI: 10.1021/ar9001069)
61. Venkatram N., Sathyavathi R., Rao D. N. (2007), Size dependent multiphoton absorption and refraction of CdSe nanoparticles, *Opt. Express*, 15, 12258-12263. (DOI: 10.1364/OE.15.012258)

62. Kapitonov A. M., Stupak A. P., Gaponenko S. V., Petrov E. P., Rogach A. L., Eychmüller A. (1999), Luminescence properties of thiol-stabilized CdTe nanocrystals, *J. Phys. Chem. B*, 103, 10109-10113. (DOI: 10.1021/jp9921809)
63. Lee J., Sundar V. C., Heine J. R., Bawendi M. G., Jensen K. F. (2000), Full color emission from II–VI semiconductor quantum dot–polymer composites, *Adv. Mater.*, 12, 1102-1105. (DOI: 10.1002/1521-4095(200008)12:15<1102::AID-ADMA1102>3.0.CO;2-J)
64. Battaglia D., Peng X. (2002), Formation of high quality InP and InAs nanocrystals in a noncoordinating solvent, *Nano Lett.*, 2, 1027-1030. (DOI: 10.1021/nl025687v)
65. Freeman R., Liu X., Willner I. (2011), Chemiluminescent and chemiluminescence resonance energy transfer (CRET) detection of DNA, metal ions, and aptamer–substrate complexes using hemin/G-quadruplexes and CdSe/ZnS quantum dots, *J. Am. Chem. Soc.*, 133, 11597-11604. (DOI: 10.1021/ja202639m)
66. Medintz I. L., Uyeda H. T., Goldman E. R., Mattoussi H. (2005), Quantum dot bioconjugates for imaging, labelling and sensing, *Nat. Mater.*, 4, 435-446. (DOI: 10.1038/nmat1390)
67. Bronstein N. D., Li L., Xu L., Yao Y., Ferry V. E., Alivisatos A. P., Nuzzo R. G. (2014), Luminescent solar concentration with semiconductor nanorods and transfer-printed micro-silicon solar cells, *ACS Nano*, 8, 44-53. (DOI: 10.1021/nn404418h)
68. Jang E., Jun S., Jang H., Lim J., Kim B., Kim Y. (2010), White-light-emitting diodes with quantum dot color converters for display

## Chapter 1

---

backlights, *Adv. Mater.*, 22, 3076-3080. (DOI: 10.1002/adma.201000525)

69. Derfus A. M., Chan W.C. W., Bhatia S. N. (2004), Probing the cytotoxicity of semiconductor quantum dots, *Nano Lett.*, 4, 11-18. (DOI: 10.1021/nl0347334)

70. Kirchner C., Liedl T., Kudera S., Pellegrino T., Javier A. M., Gaub H. E., Stölzle S., Fertig N., Parak W. J. (2005), Cytotoxicity of colloidal CdSe and CdSe/ZnS nanoparticles, *Nano Lett.*, 5, 331-338. (DOI: 10.1021/nl047996m)

71. Cho S. J., Maysinger D., Jain M., Roder B., Hackbarth S., Winnik F. M. (2007), Long-term exposure to CdTe quantum dots causes functional impairments in live cells, *Langmuir*, 23, 1974-1980. (DOI: 10.1021/la060093j)

72. Chen N., He Y., Su Y., Li X., Huang Q., Wang H., Zhang X., Tai R., Fan C. (2012), The cytotoxicity of cadmium-based quantum dots, *Biomaterials*, 33, 1238-1244. (DOI: 10.1016/j.biomaterials.2011.10.070)

73. Cheng X., Lowe S. B., Reece P. J., Gooding J. J. (2014), Colloidal silicon quantum dots: From preparation to the modification of self-assembled monolayers (SAMs) for bio-applications, *Chem. Soc. Rev.*, 43, 2680-2700. (DOI: 10.1039/c3cs60353a)

74. Hata K., Yoshida S., Fujita M., Yasuda S., Makimura T., Murakami K., Shigekawa H. (2001), Self-assembled monolayer as a template to deposit silicon nanoparticles fabricated by laser ablation, *J. Phys. Chem. B*, 105, 10842-10846. (DOI: 10.1021/jp010760b)

75. Liu S.-m., Sato S., Kimura K. (2005), Synthesis of luminescent silicon nanopowders redispersible to various solvents, *Langmuir*, 21, 6324-6329. (DOI: 10.1021/la050346t)
76. Shiohara A., Prabakar S., Faramus A., Hsu C.-Y., Lai P.-S., Northcote P. T., Tilley R. D. (2011), Sized controlled synthesis, purification, and cell studies with silicon quantum dots, *Nanoscale*, 3, 3364-3370. (DOI: 10.1039/C1NR10458F)
77. Tilley R. D., Warner J. H., Yamamoto K., Matsui I., Fujimori H. (2005), Micro-emulsion synthesis of monodisperse surface stabilized silicon nanocrystals, *Chem. Commun.*, 1833-1835. (DOI: 10.1039/B416069J)
78. Mangolini L., Thimsen E., Kortshagen U. (2005), High-yield plasma synthesis of luminescent silicon nanocrystals, *Nano Lett.*, 5, 655-659. (DOI: 10.1021/nl050066y)
79. Warner J. H., Hoshino A., Yamamoto K., Tilley R. D. (2005), Water-soluble photoluminescent silicon quantum dots, *Angew. Chem. Int. Ed.*, 44, 4550-4554. (DOI: 10.1002/anie.200501256)
80. Lie L. H., Duerdin M., Tuite E. M., Houlton A., Horrocks B. R. J. (2002), Preparation and characterisation of luminescent alkylated-silicon quantum dots, *Electroanal. Chem.*, 538, 183-190. (DOI: 10.1016/S0022-0728(02)00994-4)
81. Clark R. J., Dang M. K. M., Veinot J. G. C. (2010), Exploration of organic acid chain length on water-soluble silicon quantum dot surfaces, *Langmuir*, 26, 15657-15664. (DOI: 10.1021/la102983c)

82. Xu X., Ray R., Gu Y., Ploehn H. J., Gearheart L., Raker K., Scrivens W. A. (2004), Electrophoretic analysis and purification of fluorescent single-walled carbon nanotube fragments, *J. Am. Chem. Soc.*, 126, 12736-12737. (DOI: 10.1021/ja040082h)
83. Ding C., Zhu A., Tian Y. (2014), Functional surface engineering of C-Dots for fluorescent biosensing and in vivo bioimaging, *Acc. Chem. Res.*, 47, 20-30. (DOI: 10.1021/ar400023s)
84. Hola K., Zhang Y., Wang Y., Giannelis E. P., Zboril R., Rogach A. L. (2014), Carbon dots-emerging light emitters for bioimaging, cancer therapy and optoelectronics. *Nano Today*, 9, 590-603. (DOI: 10.1016/j.nantod.2014.09.004)
85. Zhu S., Song Y., Zhao X., Shao J., Zhang J., Yang B. (2015), The photoluminescence mechanism in carbon dots (graphene quantum dots, carbon nanodots, and polymer dots): Current state and future perspective, *Nano Res.*, 8, 355-381 (DOI: 10.1007/s12274-014-0644-3).
86. Cao L., Meziani M. J., Sahu S., Sun Y-P. (2013), Photoluminescence properties of graphene versus other carbon nanomaterials, *Acc. Chem. Res.*, 46, 171-180. (DOI: 10.1021/ar300128j)
87. Bao L., Liu C., Zhang Z-L., Pang D-W. (2015), Photoluminescence-tunable carbon nanodots: Surface-state energy-gap tuning, *Adv. Mater.*, 27, 1663-1667. (DOI: 10.1002/adma.201405070)
88. Li H., He X., Kang Z., Huang H., Liu Y., Liu J., Lian S., Tsang C. H. A., Yang X. Lee S.-T. (2010), Water-soluble fluorescent carbon

quantum dots and photocatalyst design. *Angew. Chem. Int. Ed.*, 49, 4430-4434. (DOI: 10.1002/anie.200906154)

89. Wen X., Yu P., Toh Y-R., Hao X., Tang J. (2012), Intrinsic and extrinsic fluorescence in carbon nanodots: Ultrafast time-resolved fluorescence and carrier dynamics, *J. Adv. Opt. Mater.*, 1, 173-178. (DOI: 10.1002/adom.201200046)

90. Hsu P.-C., Chang H.-T. (2012), Synthesis of high-quality carbon nanodots from hydrophilic compounds: Role of functional groups, *Chem. Commun.*, 48, 3984-3986. (DOI: 10.1039/C2CC30188A)

91. Bao L., Zhang, Z.-L., Tian Z.-Q., Zhang L., Liu C., Lin Y., Qi B., Pang D.-W. (2011), Electrochemical tuning of luminescent carbon nanodots: From preparation to luminescence mechanism, *Adv. Mater.*, 23, 5801-5806. (DOI: 10.1002/adma.201102866)

92. Sun Y.-P., Zhou B., Lin Y., Wang W., Fernando K. A. S., Pathak P., Mezziani M. J., Harruff B. A., Wang X., Wang H., Luo P. G., Yang H., Kose M. E., Chen B., Veca L. M., Xie S.-Y. (2006), Quantum-sized carbon dots for bright and colorful photoluminescence, *J. Am. Chem. Soc.*, 128, 7756-7757. (DOI: 10.1021/ja062677d)

93. Demchenko A. P., Dekaliuk M. O. (2016), The origin of emissive states of carbon nanoparticles derived from ensemble-averaged and single-molecular studies, *Nanoscale*, 8, 14057-14069. (DOI: 10.1039/C6NR02669A)

94. Thiyagarajan S. K., Raghupathy S., Palanivel D., Raji K., Ramamurthy P. (2016), Fluorescent carbon nanodots from lignite:

## Chapter 1

---

Unveiling the impeccable evidence for quantum confinement, *Phys. Chem. Chem. Phys.*, 18, 12065-12073. (DOI: 10.1039/c6cp00867d)

95. Zhu H., Wang X., Li Y., Wang Z., Yang F., Yang X. (2009), Microwave synthesis of fluorescent carbon nanoparticles with electrochemiluminescence properties, *Chem. Commun.*, 5118-5120. (DOI:10.1039/B907612C)

96. Martindale B. C. M., Hutton G. A. M., Caputo C. A., Reisner E. (2015), Solar hydrogen production using carbon quantum dots and a molecular nickel catalyst, *J. Am. Chem. Soc.*, 137, 6018-6025. (DOI: 10.1021/jacs.5b01650)

97. Ding H., Yu S.-B., Wei J.-S., Xiong H.-M. (2016), Full-color light-emitting carbon dots with a surface-state-controlled luminescence mechanism, *ACS Nano*, 10, 484-491. (DOI: 10.1021/acsnano.5b05406)

98. Zong J., Zhu Y., Yang X., Shen J., Li C. (2011), Synthesis of photoluminescent carbogenic dots using mesoporous silica spheres as nanoreactors, *Chem. Commun.*, 47, 764-766. (DOI:10.1039/C0CC03092A)

99. Jiang H., Chen F., Lagally M. G., Denes F. S. (2010), New strategy for synthesis and functionalization of carbon nanoparticles, *Langmuir*, 26, 1991-1995. (DOI: 10.1021/la9022163)

100. Xu X., Ray R., Gu Y., Ploehn H. J., Gearheart L., Raker K., Scrivens W. A. (2004), Electrophoretic analysis and purification of fluorescent single-walled carbon nanotube fragments, *J. Am. Chem. Soc.*, 126, 12736-12737. (DOI: 10.1021/ja040082h)

101. Wang J., Sahu S., Sonkar S. K., Ii K. N. T., Sun K. W., Liu Y., Maimaiti H., Anilkumar P., Sun Y.-P. (2013), Versatility with carbon dots-from overcooked BBQ to brightly fluorescent agents and photocatalysts, *RSC Adv.*, 3, 15604-15607. (DOI:10.1039/C3RA42302F)
102. Park S. Y., Lee H. U., Park E. S., Lee S. C., Lee J.-W., Jeong S. W., Kim C. H., Lee Y.-C., Huh Y. S., Lee J. (2014), Photoluminescent green carbon nanodots from food-waste-derived sources: Large-scale synthesis, properties, and biomedical applications., *ACS Appl. Mater. Interfaces*, 6, 3365-3370. (DOI: 10.1021/am500159p)
103. Cao L., Wang X., Meziani M. J., Lu F., Wang H., Luo P. G., Lin Y., Harruff B. A., Veca L. M., Murray D. (2007), Carbon dots for multiphoton bioimaging, *J. Am. Chem. Soc.*, 129, 11318-11319. (DOI: 10.1021/ja073527l)
104. Dua Y., Guo S. (2016), Chemically doped fluorescent carbon and graphene quantum dots for bioimaging, sensor, catalytic and photoelectronic applications, *Nanoscale*, 8, 2532-2543. (DOI: 10.1039/c5nr07579c)
105. Feng T., Ai X., An G., Yang P., Zhao Y. (2016), Charge-convertible carbon dots for imaging-guided drug delivery with enhanced in vivo cancer therapeutic efficiency, *ACS Nano*, 10, 4410-4420. (DOI: 10.1021/acsnano.6b00043)
106. Lakowicz J. R., (1999), Principles of fluorescence spectroscopy, 2nd ed., Academic Press, New York. (ISBN: 0-306-46093-9)

## Chapter 1

---

107. Nimmo M. T., Caillard L. M., Benedetti W. D., Nguyen H. M., Seitz O., Gartstein, Y. N., Chabal Y. J., Malko A. V. (2013), Visible to near-infrared sensitization of silicon substrates via energy transfer from proximal nanocrystals: Further insights for hybrid photovoltaics, *ACS Nano*, 7, 3236-3245. (DOI: 10.1021/nn400924y)
108. Shan T., Liu Y., Tang X., Bai Q., Gao Y., Gao Z., Li J., Deng J., Yang B., Lu P., Ma Y. (2016), Highly efficient deep blue organic light-emitting diodes based on imidazole: Significantly enhanced performance by effective energy transfer with negligible efficiency roll-off, *ACS Appl. Mater. Interfaces*, 8, 28771-28779. (DOI: 10.1021/acsami.6b10004)
109. Wu X., Song Y., Yan X., Zhu C., Ma Y., Du D., Lin Y. (2017), Carbon quantum dots as fluorescence resonance energy transfer sensors for organophosphate pesticides determination, *Biosens. Bioelectron.*, 94, 292-297. (DOI: 10.1016/j.bios.2017.03.010)
110. Kulkarni B., Jayakannan M. (2017), Fluorescent-tagged biodegradable polycaprolactone block copolymer FRET probe for intracellular bioimaging in cancer cells, *ACS Biomater. Sci. Eng.*, 3, 2185–2197. (DOI: 10.1021/acsbiomaterials.7b00426)
111. Förster T. (1948), Intermolecular energy migration and fluorescence, *Ann. Phys.*, 2, 55-75. (DOI: 10.1002/andp.19484370105)
112. Kuhn H. (1970), Classical aspects of energy transfer in molecular systems, *J. Chem. Phys.*, 53, 101-108. (DOI: 10.1063/1.1673749)
113. Chiu Y.-L., Chen S.-A., Chen J.-H., Chen K.-J., Chen H.-L., Sung H.-W. (2010), A dual-emission Förster resonance energy transfer

nanoprobe for sensing/imaging pH changes in the biological environment, *ACS Nano*, 4, 7467-7474. (DOI: 10.1021/nn102644u)

114. Samanta A., Zhou Y., Zou S., Yan H., Liu Y. (2014), Fluorescence quenching of quantum dots by gold nanoparticles: A potential long range spectroscopic ruler, *Nano Lett.*, 14, 5052–5057. (DOI: 10.1021/nl501709s)

115. Singh M. P., Strouse G. F. (2010), Involvement of the LSPR spectral overlap for energy transfer between a dye and Au nanoparticle, *J. Am. Chem. Soc.*, 132, 9383-9391. (DOI: 10.1021/ja1022128)

116. Breshike C. J., Riskowski R. A., Strouse G. F. (2013), Leaving Förster resonance energy transfer behind: Nanometal surface energy transfer predicts the size-enhanced energy coupling between a metal nanoparticle and an emitting dipole, *J. Phys. Chem. C*, 117, 23942-23949. (DOI: 10.1021/jp407259r)

117. Dulkeith E., Ringler M., Klar T. A., Feldmann J., Javier A. M., Parak W. J. (2005), Gold nanoparticles quench fluorescence by phase induced radiative rate suppression, *Nano Lett.*, 5, 585-589. (DOI: 10.1021/nl0480969)

118. Gersten J., Nitzan A. (1981), Spectroscopic properties of molecules interacting with small dielectric particles, *J. Chem. Phys.*, 75, 1139-1152. (DOI: 10.1063/1.442161)

119. Inacker O., Kuhn H. (1974), Energy transfer from dye to specific singlet or triplet energy acceptors in monolayer assemblies, *Chem. Phys. Lett.*, 27, 317-321. (DOI: 10.1016/0009-2614(74)90232-2)

## **Chapter 1**

---

120. Chance R. R., Miller A. H., Prock A., Silbey R. (1975), Fluorescence and energy transfer near interfaces: The complete and quantitative description of the Eu<sup>3+</sup>/mirror systems, *J. Chem. Phys.*, 63, 1589-1595. (DOI: 10.1063/1.431483)
121. Jennings T. L., Singh M. P., Strouse G. F. (2006), Fluorescent lifetime quenching near  $d = 1.5$  nm gold nanoparticles: Probing NSET validity, *J. Am. Chem. Soc.*, 128, 5462-5467. (DOI: 10.1021/ja0583665)
122. Mandal S., Ghatak C., Rao V. G., Ghosh S., Sarkar N. (2012), Pluronic micellar aggregates loaded with gold nanoparticles (Au NPs) and fluorescent dyes: A study of controlled nanometal surface energy transfer, *J. Phys. Chem. C*, 116, 5585-5597. (DOI: 10.1021/jp2093127)
123. Kikkeri R., Padler-Karavani V., Diaz S., Verhagen A., Yu H., Cao H., Langereis M. A., Groot R. J. D., Chen X., Varki A. (2013), Quantum dot nanometal surface energy transfer based biosensing of sialic acid compositions and linkages in biological samples, *Anal. Chem.*, 85, 3864-3870. (DOI: 10.1021/ac400320n)
124. Xavier P. L., Chaudhari K., Verma P. K., Pal S. K., Pradeep T. (2010), Luminescent quantum clusters of gold in transferrin family protein, lactoferrin exhibiting FRET, *Nanoscale*, 2, 2769-2776. (DOI: 10.1039/c0nr00377h)
125. Liu S., Zhao N., Cheng Z., Liu H. (2015), Amino-functionalized green fluorescent carbon dots as surface energy transfer biosensors for hyaluronidase, *Nanoscale*, 7, 6836-6842. (DOI: 10.1039/c5nr00070j)

126. Pu K.-Y., Luo Z., Li K., Xie J., Liu B. (2011), Energy transfer between conjugated-oligoelectrolyte-substituted POSS and gold nanocluster for multicolor intracellular detection of mercury ion, *J. Phys. Chem. C*, 115, 13069-13075. (DOI: 10.1021/jp203133t)
127. Russell B. A., Kubiak-Ossowska K., Mulheran P. A., Bircha D. J. S., Chen Y. (2015), Locating the nucleation sites for protein encapsulated gold nanoclusters: A molecular dynamics and fluorescence study, *Phys. Chem. Chem. Phys.*, 17, 21935-21941.(DOI: 10.1039/c5cp02380g)
128. Raut S., Rich R., Fudala R., Butler S., Kokate R., Gryczynski Z., Luchowski R., Gryczynski I. (2014), Resonance energy transfer between fluorescent BSA protected Au nanoclusters and organic fluorophores, *Nanoscale*, 6, 385-391. (DOI:10.1039/c3nr03886f)
129. Liu L., Fei X., Zhu S., Yu L., Zhang B. (2013), Self-assembly of anionic Gemini surfactant: Fluorescence resonance energy transfer and simulation study, *Langmuir*, 29, 5132-5137. (DOI: 10.1021/la304980r)
130. Sahu K., Ghosh S., Mondal S. K., Ghosh B. C., Sen P., Roy D., Bhattacharyya K. (2006), Ultrafast fluorescence resonance energy transfer in a micelle, *J. Chem. Phys.*, 125, 044714. (DOI: 10.1063/1.2218847)
131. Tang J., Kong B., Wu H., Xu M., Wang Y., Wang Y., Zhao D., Zhen G. (2013), Carbon nanodots featuring efficient FRET for real-time monitoring of drug delivery and two-photon imaging, *Adv. Mater.*, 25, 6569-6574. (DOI:10.1002/adma.201303124)

## **Chapter 1**

---

132. Sarkar P. K., Polley N., Chakrabarti S., Lemmens P., Pal S. K. (2016), Nanosurface energy transfer based highly selective and ultrasensitive “turn on” fluorescence mercury sensor, *ACS Sens.*, 1, 789-797. (DOI: 10.1021/acssensors.6b00153)
133. Moulik S. P. (1996), Micelles: Self-organized surfactant assemblies, *Curr. Sci.*, 71, 368-376.
134. Stigter D. (1974), Micelle formation by ionic surfactants. II. Specificity of head groups, micelle structure, *J. Phys. Chem.*, 78, 2480-2485. (DOI: 10.1021/j100617a013)
135. Mazer N. A., Benedek G. B., Carey M. C. (1976), An investigation of the micellar phase of sodium dodecyl sulfate in aqueous sodium chloride solutions using quasielastic light scattering spectroscopy, *J. Phys. Chem.*, 80, 1075-1085. (DOI: 10.1021/j100551a011)
136. Dawson D. R., Offen H. W., Nicoli D. F. (1981), Pressure effects on micellar size, *J. Colloid Interface Sci.*, 81, 396-401. (DOI: 10.1016/0021-9797(81)90421-5)
137. Bonincontro A., Cametti C., Marchetti S., Onori G. (2003), Influence of the pH-induced ionization on the conformation of dodecyltrimethylamine oxide micelles: A radiowave dielectric relaxation and light-scattering study, *J. Phys. Chem. B*, 107, 10671-10676. (DOI: 10.1021/jp034193z)
138. [www.study.com/academy/lesson/what-are-polymers-properties-applications-examples](http://www.study.com/academy/lesson/what-are-polymers-properties-applications-examples)

139. Wagh A., Qian S.Y., Law B. (2012), Development of biocompatible polymeric nanoparticles for in vivo NIR and FRET imaging, *Bioconjugate Chem.*, 23, 981-992. (DOI: 10.1021/bc200637h)
140. Kost J., Langer R. (2001), Responsive polymeric delivery systems, *Adv. Drug Deli. Rev.*, 46, 125-148. (DOI: 10.1016/S0169-409X(00)00136-8)
141. Liechty W.B., Kryscio D.R., Slaughter B.V., Peppas N.A. (2010), Polymers for drug delivery systems, *Annu. Rev. Chem. Biomol. Eng.*, 1, 149-173. (DOI: 10.1146/annurev-chembioeng-073009-100847)
142. Wu W., Aiello M., Zhou T., Berliner A., Banerjee P., Zhou S. (2010), In-situ immobilization of quantum dots in polysaccharide-based nanogels for integration of optical pH-sensing, tumor cell imaging, and drug delivery, *Biomaterials*, 31, 3023-3031. (DOI: 10.1016/j.biomaterials.2010.01.011)
143. Watson J. D., (2003), *DNA: The secret of life*, Alfred A. Knopf. (ISBN: 0375415467, 9780375415463)
144. Ortiz M., Fragoso A., Ortiz P. J., O'Sullivan C. K. (2011), Elucidation of the mechanism of single-stranded DNA interaction with methylene blue: A spectroscopic approach, *J. Photochem. Photobiol. A: Chem.*, 218, 26-32. (DOI: 10.1016/j.jphotochem.2010.11.020)
145. Kricka L. J., Fortina P. (2009), Analytical ancestry: "Firsts" in fluorescent labeling of nucleosides, nucleotides, and nucleic acids, *Clin. Chem.*, 55, 670-683. (DOI: 10.1373/clinchem.2008.116152)
146. Law G.-L., Man C., Parker D., Walton J. W. (2010), Observation of the selective staining of chromosomal DNA in dividing cells using a

## Chapter 1

---

luminescent terbium(III) complex, *Chem. Commun.*, 46, 2391-2393.

(DOI: 10.1039/B924679G)

147. Erve A., Saoudi Y., Thiroit S., Guetta-Landras C., Florent J.-C., Nguyen C.-H., Grierson D. S., Popov A. V. (2006), BENA435, a new cell-permeant photoactivated green fluorescent DNA probe, *Nucleic Acids Res.*, 34, e43. (DOI: 10.1093/nar/gkl011)

148. Feng S., Kim Y. K., Yang S., Chang Y. T. (2010), Discovery of a green DNA probe for live-cell imaging, *Chem. Commun.*, 46, 436-438. (DOI:10.1039/B916858C)

149. Barni E., Savarino P., Viscardi G. (1991), Dye-surfactant interactions and their applications, *Acc. Chem. Res.*, 24, 98-103. (DOI: 10.1021/ar00004a002)

150. Maiti N. C., Krishna M. M. G., Britto P. J., Periasamy N. (1997), Fluorescence dynamics of dye probes in micelles, *J. Phys. Chem. B*, 101, 11051-11060. (DOI: 10.1021/jp9723123)

151. Raja S. N., Zhrebetskyy D., Wu S., Ercius P., Powers A., Olson A. C. K., Du D. X., Lin L., Govindjee S., Wang L.-W., Xu T., Alivisatos A. P., Ritchie R. O. (2016), Mechanisms of local stress sensing in multifunctional polymer films using fluorescent tetrapod nanocrystals, *Nano Lett.*, 16, 5060-5067. (DOI: 10.1021/acs.nanolett.6b01907)

152. Lu C.-H., Willner B., Willner I. (2013), DNA nanotechnology: From sensing and DNA machines to drug-delivery systems, *ACS Nano*, 7, 8320-8332. (DOI: 10.1021/nn404613v)

153. Mondal S., Das T., Ghosh P., Maity A., Mallick A., Purkayastha P. (2013), FRET-based characterisation of surfactant bilayer protected core-shell carbon nanoparticles: Advancement toward carbon nanotechnology, *Chem. Commun.*, 49, 7638-7640. (DOI: 10.1039/c3cc43443e)

154. Kundu S., Bhattacharyya S., Patra A. (2014), Photoinduced energy transfer in dye encapsulated polymer nanoparticle-CdTe quantum dot light harvesting assemblies, *Mater. Horiz.*, 2, 60-67. (DOI: 10.1039/c4mh00138a)



**Chapter 2**

*Materials and  
Experimental Techniques*

### 2.1. Introduction

This chapter mentions all the chemicals used for the synthesis of Si QD, CD, Ag NP, and Ag NC along with the chemicals utilized to study the mechanism of resonance energy transfer in different restricted environments such as surfactant assemblies, polymer, and DNA. The complete synthesis procedures of allylamine-capped Si QDs, CDs, citrate-stabilized Ag NPs and dihydrolipoic acid capped Ag NCs have been discussed in detail. All the sample preparation methods opted during the work of this thesis have been mentioned here. This chapter also covers the detailed experimental techniques used to complete the entire thesis work.

### 2.2. Chemicals

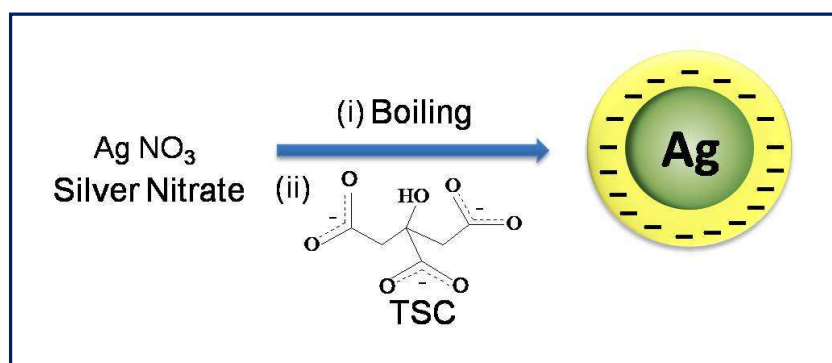
Silver nitrate ( $\text{Ag NO}_3$ ,  $\geq 99\%$ ), cetyltrimethylammonium bromide (CTAB,  $\geq 98\%$ ), triton X-100 (TX-100, AR grade), tetraoctylammonium bromide (TOAB, 98%), chloroplatinic acid hexahydrate, sodium dodecyl sulfate (SDS, 98.5%), quinine sulphate dihydrate, isopropyl alcohol (99%), coumarin 152, ethylenediamine (EDA,  $\geq 99.5\%$ ), Pur-A-Lyzert Dialysis Kit (MWCO 3.5 kDa), ( $\pm$ )- $\alpha$ -lipoic acid, 4',6-diamidino-2-phenylindole dihydrochloride (DAPI,  $\geq 95\%$ , HPLC), methanol, poly(diallyldimethylammoniumchloride) (PDADMAC, MW= 100000-200000), and deoxyribonucleic acid sodium salt from Calf Thymus (type 1 fibers, CT-DNA) were purchased from Sigma-Aldrich. Tri-sodium citrate dihydrate (TSC), silicon tetra-chloride ( $\text{SiCl}_4$ , 99%), sulphuric acid ( $\text{H}_2\text{SO}_4$ , 98%), tetrahydrofuran (THF, 99.5%), and citric acid monohydrate (99.5%) were purchased from Merck (Germany). Allylamine (99%) was purchased from Spectrochem (India). Lithium aluminum hydride (LAH, 97%) and toluene (99%) were purchased from SD Fine Chemicals (India).

Sodium borohydride ( $\text{NaBH}_4$ ) was purchased from SRL. Milli-Q water was obtained from a Millipore water purifier system (Milli-Q integral).

### 2.3. Synthesis

#### 2.3.1. Citrate-Stabilized Silver Nanoparticles (Ag NPs)

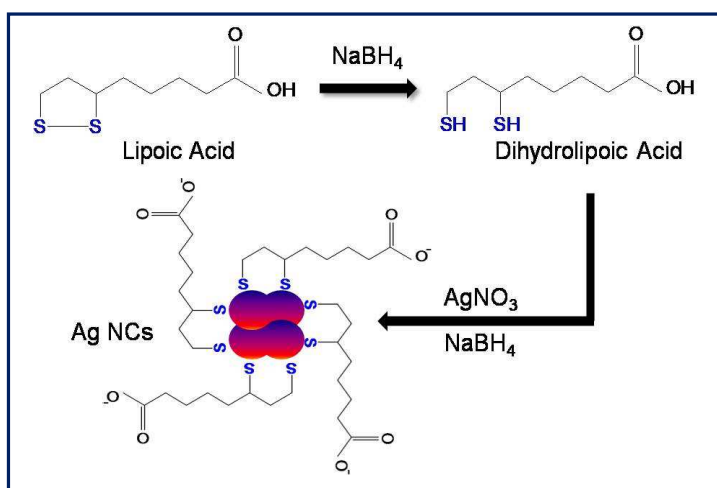
Different sized Ag NPs were prepared by the well-known Lee and Meisels method by slightly varying the amount of  $\text{AgNO}_3$  and TSC in order to synthesize Ag NPs having sizes from 35 to 75 nm [1]. A solution of  $\text{AgNO}_3$  (25 mL) in deionized water was heated to boiling. Then, 4 mL tri-sodium citrate (TSC) solution was added drop-wise to the boiling silver nitrate solution, accompanied by vigorous stirring. The color of the solution slowly turned into greyish yellow, indicating the reduction of the  $\text{Ag}^+$  ions. The heating was continued for an additional 15 min and finally, a green-grey silver colloid was obtained (Scheme 2.1). The solution was removed from the heating element and stirred until cooled to room temperature. The final concentration of synthesized Ag NPs was estimated using the molar extinction coefficient at maximum LSPR wavelength [2].



**Scheme 2.1.** Synthesis of citrate stabilized Ag NPs.

### 2.3.2. Dihydrolipoic Acid-Capped Silver Nanoclusters (Ag NCs)

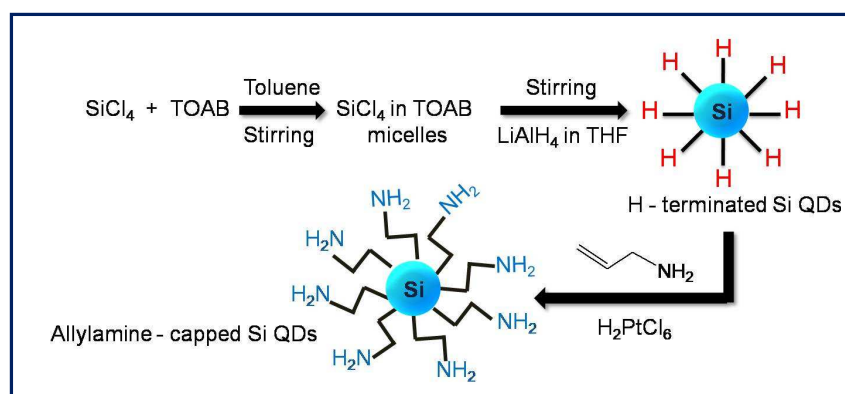
Ag NCs were synthesized according to the earlier literature with minor modification (Scheme 2.2) [3]. 26.30 mg of lipoic acid and 10 mL of Milli-Q water were placed in a round bottom flask. To this insoluble mixture, ~1.5 mg of pure sodium borohydride was added and stirred well until a clear solution was obtained. In this step, the insoluble mixture of lipoic acid is reduced to water-soluble dihydrolipoic acid (DHLA). Next, to prepare fluorescent Ag NCs, 500  $\mu\text{L}$  of 25 mM aqueous  $\text{AgNO}_3$  solution is added to the freshly prepared above aqueous DHLA solution and this mixture was stirred well for 1 min. To this, a slight excess of dilute aqueous sodium borohydride solution was added slowly and the stirring was continued for 3 h. The color of the solution changes from colorless to deep orange marking the completion of the reaction. The concentration of as-synthesized Ag NCs was estimated ~0.2 mM based on the assumption that all the silver in silver nitrate was reduced to form Ag NCs.



**Scheme 2.2.** Synthesis of DHLA-capped Ag NCs.

### 2.3.3. Allylamine-Capped Silicon Quantum Dots (Si QDs)

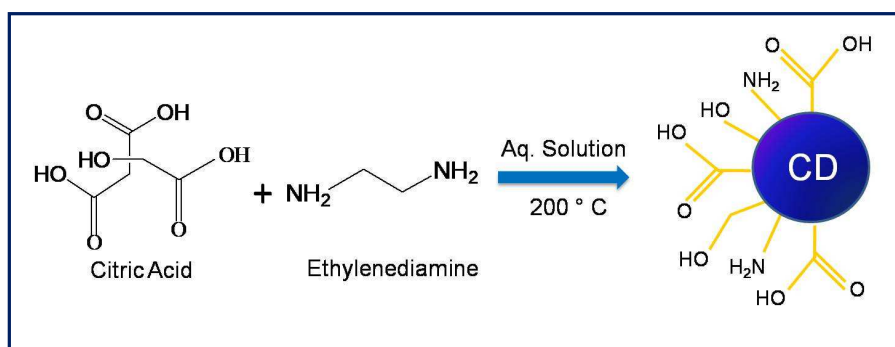
The allylamine-capped Si QDs were synthesized under an argon atmosphere according to the literature (Scheme 2.3) [4]. Initially, TOAB (1.5 g) was dispersed in dry toluene (100 mL) by stirring for 30 min. Then 92  $\mu\text{L}$  of  $\text{SiCl}_4$  was added through a gastight syringe, followed by stirring for 1 h. The hydrogen-terminated Si-QDs were then formed by adding 2 mL of 1 M LAH in THF. After 3 h, anhydrous methanol (20 mL) was added to oxidize the excess LAH. The hydrophilic particles were then formed by modifying the surface Si-H bond by the reaction with 100  $\mu\text{L}$  of 0.1 M chloroplatinic acid hexahydrate in isopropanol as a catalyst and 2 mL of allylamine. After 3 h of stirring, the solvent was then removed by rotary evaporation to produce a white dry powder consisting of mainly TOAB and Si-QDs. The hydrophilic allylamine-capped Si QDs were then redispersed in 20 mL of distilled water followed by its sonication for 30 min. Then the allylamine-capped Si-QDs were dissolved in water, and the undissolved TOAB was removed by successive filtration through a 0.22  $\mu\text{m}$  membrane filter. The concentration of the synthesized Si-QD solution was estimated spectrophotometrically using  $\epsilon_{260}$  of  $2.6 \times 10^5 \text{ M}^{-1} \text{ cm}^{-1}$  [5].



**Scheme 2.3.** Synthesis of allylamine-capped Si QDs in TOAB micelles.

### 2.3.4. Carbon Dots (CDs)

The synthesis of CD was carried out according to the literature (Scheme 2.4) [6]. In brief, citric acid (1.015 g) and ethylenediamine (335 mL) were dissolved in Milli-Q water (10 mL) and sonicated for 5 min. Then the solution was transferred to a teflon-coated stainless steel autoclave (25 mL) and heated at 200 °C for 5 h. Subsequently, the reactor was cooled to room temperature and the solution was dialyzed in the Pur-A-Lyzert Dialysis Kit (MWCO3.5 kDa) (Sigma-Aldrich) for 48 h. The water for dialysis was changed after every 6 h. Finally, the black-brown CD solution was obtained.



**Scheme 2.4.** Synthesis of CDs using citric acid and ethylenediamine.

### 2.4. Sample Preparations

The synthesized Si QDs, CDs, Ag NPs, and Ag NCs were further diluted as per the experimental requirements using pH 7.4 phosphate buffer. The aqueous stock solutions of DAPI, SDS, TX-100, and CTAB were prepared by dissolving the desired amount in Milli-Q water. For further experiments, the aqueous stock solutions of DAPI, SDS, TX-100, and CTAB were diluted using phosphate buffer (pH 7.4). PDADMAC was

used directly from the stock according to the weight percentage. CT-DNA solution was prepared by dissolving 0.5 mg/mL in phosphate buffer (pH 7.4). The DNA purity was estimated  $\sim 1.76$  ( $A_{260}/A_{280}$ ) and the concentration of the CT-DNA stock was determined using  $\epsilon_{260}=13200$  bp  $M^{-1} cm^{-1}$ . For microscopy experiment, the samples were spin coated on a clean cover slide with a spin coater (Apex Instruments, Spin NXG-P1). Cleaning of the cover slides was done by using chromic acid, followed by 2% Hellmanex III (Sigma-Aldrich). Each of the cleaning steps was followed by repeated washing with Milli-Q water. Finally, the washed slides were rinsed with methanol and dried in vacuum oven. The samples were spin cast on cover slides at 1000 rpm for 3 min.

The fluorescence quantum yields ( $\phi$ ) of Si QDs, CDs and DAPI were estimated by using the following equation:

$$\phi_S = \phi_{ST} \left( \frac{I_S}{I_{ST}} \right) \left( \frac{\eta_S^2}{\eta_{ST}^2} \right) \left( \frac{A_{ST}}{A_S} \right)$$

where  $\phi$  is the QY,  $I$  is the integrated fluorescence intensity,  $\eta$  is the refractive index of the solvent, and  $A$  is the optical density. The subscript “ST” stands for standard and “S” stands for the sample. For Si QDs and DAPI, the QY was estimated using quinine sulfate ( $\phi= 0.54$  in 0.1M  $H_2SO_4$ ) as the standard [7]. The QY of CD at 400 nm excitation wavelength, was estimated relative to coumarin 152 dye ( $\phi= 0.19$  in ethanol) [8].

### **2.5. Instrumentation**

#### **2.5.1. Fourier Transform Infrared (FTIR) Spectrometer**

FTIR technique was used to confirm the formation of Si QDs, CDs, Ag NPs, and Ag NCs. The characteristic bond frequencies of the surface ligands were measured with the help of a Bruker spectrometer (Tensor-27) on a thin KBr pellet and were collected in the wavenumber range of 800 to 4000  $\text{cm}^{-1}$ .

#### **2.5.2. Atomic Force Microscope (AFM)**

The morphologies and sizes of the synthesized Si QDs and Ag NPs were determined by AFM technique. AFM images were recorded on a cleaned glass coverslip using a scanning probe microscope AIST-NT microscope (model SmartSPM-1000). The samples were deposited on the coverslips by spin-coating at 1000 rpm for 5 min.

#### **2.5.3. Field-Emission Scanning Electron Microscope (FE-SEM)**

The morphologies and sizes of different sized Ag NPs were estimated using FE-SEM technique. The SEM images were recorded by using FE-SEM, Supra 55 Zeiss. The samples were spin-coated on the coverslips at 1500 rpm for 3 min followed by the gold coating.

#### **2.5.4. Transmission Electron Microscope (TEM)**

TEM was used to determine morphologies and sizes of the synthesized CDs and Ag NCs as well as to visualize the morphology of Ag NCs-PDADMAC composite. The images were recorded on a JEOL electron microscope (JEM-2100 F) operating at an accelerating voltage of

200 kV. Samples were placed on the holey carbon lacey grid and air dried prior to imaging.

### **2.5.5. Liquid Chromatography-Mass Spectrometer (LC-MS)**

In order to confirm the exact molecular mass and composition of the as-synthesized Ag NC core, mass spectrometric analysis was performed. Mass spectrum was recorded using electrospray ionization (ESI) quadrupole time-of-flight liquid chromatography-mass spectrometer (Bruker Daltonik) in 1:1 water-methanol mixture as a solvent by positive-mode ESI.

### **2.5.6. Powder X-Ray Diffractometer (PXRD)**

The powder X-ray diffraction pattern of CDs was recorded on a Rigaku SmartLab, Automated Multipurpose X-ray Diffractometer with a Cu K $\alpha$  source (the wavelength of X-rays was 0.154 nm).

### **2.5.7. X-ray Photoelectron Spectrometer (XPS)**

The chemical nature and composition of Ag NCs were determined by using XPS. The X-ray photoelectron spectrum was recorded using Mg K-alpha (1253.6 eV) source and DESA-150 electron analyzer (Staub Instruments, Germany). The binding-energy scale was calibrated to Au-4f<sub>7/2</sub> line of 83.95 eV. The sample was drop cast on a glass plate and dried in air under IR lamp. Chamber pressure during XPS measurement was  $1 \times 10^{-8}$  Torr.

### **2.5.8. Dynamic Light Scattering (DLS) and Zeta Potential**

DLS was used to estimate the hydrodynamic diameter of CDs, Ag NPs and Ag NCs. For CDs and Ag NCs, the diameters were determined

using the Brookhaven particle size analyzer (model 90 Plus). The DLS and zeta potential measurements for different sized Ag NPs were performed on the NanoPlus zeta/particle size analyzer (NanoPlus-3 model). The zeta potential of CDs was also estimated using the same set-up. All the samples for DLS and zeta potential measurements were prepared in phosphate buffer (pH 7.4) and were filtered through 0.22  $\mu\text{m}$  syringe filter (Whatman) prior to measurements.

### **2.5.9. UV-Vis Spectrophotometer**

Absorption spectra were recorded in a quartz cuvette ( $10 \times 10$  mm) using a Varian UV-Vis spectrophotometer (Carry 100 Bio) and were corrected using solvent absorption as the baseline.

### **2.5.10. Spectrofluorometer**

PL spectra were recorded using Fluoromax-4 spectrofluorometer (HORIBA JobinYvon, model FM-100) with excitation and emission slit width at 2 nm. All measurements were performed at room temperature.

### **2.5.11. Time-Correlated Single Photon Counting Technique (TCSPC)**

To estimate the PL lifetime, TCSPC technique was used. Photoluminescence (PL) decays were recorded on a HORIBA JobinYvon picosecond time-correlated single photon counting (TCSPC) spectrometer (model Fluorocube-01-NL). The PL decays were collected with the emission polarizer at a magic angle of  $54.7^\circ$  by a photomultiplier tube (TBX-07C). The instrument response function (IRF, FWHM~ 140 ps) was recorded using a dilute scattering solution. The PL decays were analyzed using IBH DAS 6.0 software by the iterative deconvolution

method, and the goodness of the fit was judged by reduced  $\chi$ -square ( $\chi^2$ ) value. All the decays were fitted with an exponential function:

$$F(t) = \sum_{i=1}^n a_i \exp(-t/\tau_i)$$

where  $F(t)$  denotes normalized PL decay,  $a_i$  is the normalized amplitude of decay component  $\tau_i$ , and  $n$  represents the number of decay components.

The average lifetime ( $\tau_{avg}$ ) was obtained from the equation:

$$\tau_{avg} = \sum_{i=1}^n a_i \tau_i$$

### 2.5.12. Femtosecond Fluorescence Upconversion

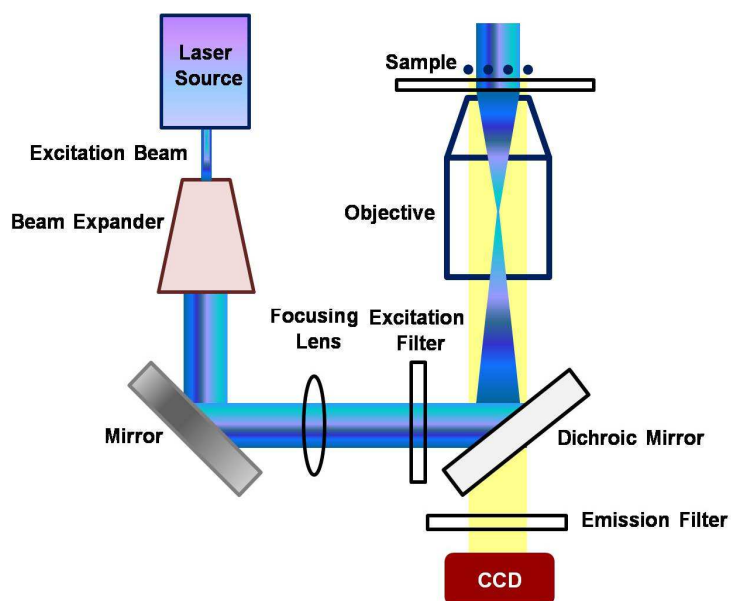
The femtosecond fluorescence upconversion measurements were performed to explore the dynamics of fluorescence quenching of DAPI in the presence of Ag NCs. The absorbance of the samples was kept  $\sim 1$  for the upconversion experiments. The output of a femtosecond pulsed oscillator from a mode-locked Ti:sapphire laser (Tsunami, Spectra Physics, USA) pumped by a 5 W DPSS laser (Millennia, Spectra Physics), centered at 740 nm with a repetition rate of 80 MHz, was used as the gate pulse for the femtosecond fluorescence upconversion experiments. The second harmonic (375 nm) of this pulse was used as the source of excitation for the sample placed in a rotating cell. The power of the second harmonic light was restricted to 5 mW at the sample in order to minimize photobleaching. The fluorescence from the sample was upconverted in a nonlinear crystal (0.5 mm BBO,  $\theta = 38^\circ$ ,  $\varphi = 90^\circ$ ) by mixing with the gate

pulse, which consists of a portion of the fundamental beam. The upconverted light was dispersed in a monochromator and detected using photon counting electronics. A cross-correlation function had FWHM of 300 fs which was obtained using the Raman scattering from ethanol. The femtosecond fluorescence decays were fitted using a Gaussian function of the same FWHM as the excitation pulse. The fluorescence decays were recorded at the magic angle polarization with respect to the excitation pulse on FOG 100 fluorescence optically gated upconversion spectrometer (CDP Systems Corp., Russia). The resolution was in appropriate multiples of the minimum step size of the instrument, i.e. 0.78 fs/step. The decays were analyzed by iterative reconvolution using a homemade program using Igor Pro software [9].

### 2.5.13. Single Molecule Epifluorescence Microscopy

Microscopy experiments were performed on a home-built epifluorescence microscopy setup (Scheme 2.5). An air-cooled argon ion laser (Melles Griot, model 400-A03) with excitation wavelength at 457 nm was used to excite the sample placed on an inverted microscope (Nikon, model Eclipse Ti-U). The laser beam was expanded and subsequently focused on the back-focal plane of an oil immersion objective (100× 1.49 NA Nikon) to illuminate  $60 \times 60 \mu\text{m}^2$  area of the sample. The PL from the sample was collected through a B2A filter cube (Nikon) with a 505 nm dichroic mirror and a 520 nm long-pass filter and finally imaged with a back-illuminated EMCCD camera (Andor, model iXon X3 897). The exposure time was 200 ms. The images were analyzed with ImageJ (Version 1.46r) NIH. All PL measurements were performed at room temperature. For microscopy experiments, the samples were spin-

casted with a spin-coater (Apex Instruments, Spin NXG-P1) on a clean cover slide.



**Scheme 2.5.** Schematic representation of our home-built epifluorescence microscope.

### 2.5. References

1. Lee P. C., Meisel D. (1982), Adsorption and surface-enhanced Raman of dyes on silver and gold sols, *J. Phys. Chem.*, 86, 3391-3395. (DOI: 10.1021/j100214a025)
2. Paramelle D., Sadovoy A., Gorelik S., Free P., Hobley J., Fernig D. G. (2014), A rapid method to estimate the concentration of citrate capped silver nanoparticles from UV-visible light spectra. *Analyst*, 139, 4855-4861. (DOI:10.1039/C4AN00978A)
3. Adhikari B. and Banerjee A. (2010), Facile synthesis of water-soluble fluorescent silver nanoclusters and HgII sensing, *Chem. Mater.*, 22, 4364-4371. (DOI: 10.1021/cm1001253)
4. Warner J. H., Hoshino A., Yamamoto K., Tilley R. D. (2005), Water-soluble photoluminescent silicon quantum dots, *Angew. Chem. Int. Ed.*, 44, 4550-4554. (DOI: 10.1002/anie.200501256)
5. Rosso-Vasic M., Cola L. D., Zuilhof H. (2009), Efficient energy transfer between silicon nanoparticles and a Ru-polypyridine complex, *J. Phys. Chem. C*, 113, 2235-2240. (DOI: 10.1021/jp804623w)
6. Zhu S., Meng Q., Wang L., Zhang J., Song Y., Jin H., Zhang K., Sun H., Wang H., Yang B. (2013), Highly photoluminescent carbon dots for multicolor patterning, sensors, and bioimaging, *Angew. Chem. Int. Ed.*, 52, 3953-3957. (DOI: 10.1002/anie.201300519)
7. Lakowicz J. R., (1999), *Principles of fluorescence spectroscopy*, 2nd ed., Academic Press, New York. (ISBN: 0-306-46093-9)

8. Nad S., Kumbhakar M., Pal H. (2003), Photophysical properties of coumarin-152 and coumarin-481 dyes: Unusual behavior in nonpolar and in higher polarity solvents. *J. Phys. Chem. A*, 107, 4808-4816. (DOI: 10.1021/jp021543t)
9. Chatterjee S., Karuso P., Boulangé A., Peixoto P. A., Franck X. and Datta A. (2013), Ultrafast dynamics of epicocconone, a second generation fluorescent protein stain, *J. Phys. Chem. B*, 117, 14951-14959. (DOI: 10.1021/jp205634)



**Chapter 3**

*Surfactant-Induced Modulation of  
Nanometal Surface Energy Transfer  
from Silicon Quantum Dots to Silver  
Nanoparticles*

### 3.1. Introduction

Excitation energy transfer from various photo-excited donors to ground state acceptors has been studied thoroughly in the recent past due to its importance in photovoltaics, light-emitting diodes, sensors, and bioimaging [1-8]. The nonradiative energy transfer from a photo-excited donor to an acceptor via dipole-dipole interactions is well known as Förster resonance energy transfer (FRET). Over the past few years, metal and semiconductor NPs based donor-acceptor nanocomposite systems have gained considerable attention due to their unique optoelectronic properties which allow easy tuning of energy transfer efficiency [9-14]. Extensive theoretical and experimental studies have been performed to understand the highly efficient quenching of molecular excitation energy of various fluorophores by metal nanoparticles. The quenching of excited donor in the presence of metal NP is demonstrated earlier by Chance et al. (1978) and later extended by Persson and Lang (1982) by using a Fermi Golden Rule [15, 16]. This dipole to metal surface excitation energy transfer is known as nanometal surface energy transfer (NSET). The details related to both the energy transfer mechanisms have been mentioned in the introduction of this thesis.

The fundamental difference between FRET and NSET is that for the later process it is not necessary to have a spectral overlap between donor emission and the acceptor absorption. For example, Jennings et al. (2006) have demonstrated the distance-dependent fluorescence quenching of different dyes attached to 1.5 nm Au NPs, which lack characteristic SPR band. They have observed a  $1/d^4$  distance-dependent quenching mechanism irrespective of the length of the dsDNA and assigned it due to nonradiative energy transfer to the metal surface, while the radiative rate

remains unchanged [17]. In another study, Haldar et al. (2010) have demonstrated that the significant spectral overlap between the emission spectrum of CdSe QDs and the LSPR of Au NPs leads to an efficient nonradiative FRET between them [18]. Similarly, Li et al. (2011) have demonstrated the effect of metal NPs size and the degree of spectral overlap on the energy transfer process between CdSe/ZnS QDs and Au NPs [12]. It has been observed that 3 nm sized Au NPs with negligible LSPR quench the PL of QDs with a  $1/d^4$  distance dependence, while 15 and 80 nm sized Au NPs with strong LSPR band that overlaps with the PL band of the QDs quench the PL with a  $1/d^6$  distance dependence, which is dominated by the dipole-dipole interaction according to FRET.

In this chapter, we have investigated the influence of Ag NPs on the PL properties of water-dispersed biocompatible Si QDs in the absence and presence of cetyltrimethylammonium bromide (CTAB) and shown that even with significant spectral overlap between the luminescence spectra of Si QDs and LSPR of Ag NPs, the nonradiative EET process follows NSET theory rather than conventional FRET theory. Moreover, easy tuning of the EET efficiency has been achieved by using CTAB surfactant.

### 3.2. Results and Discussion

#### 3.2.1. Characterization of Si QDs and Ag NPs

Synthesized allylamine-capped Si QDs were characterized by Fourier transform infrared (FTIR) spectroscopy, atomic force microscopy (AFM), UV-Vis and PL spectroscopy. The chemical attachment of allylamine moieties at the Si QDs surface is confirmed by FTIR spectroscopy (Figure 3.1). The most characteristic peak at  $1640\text{ cm}^{-1}$

indicates the attachment of allylamine moiety at the surface of Si QDs, which is very close to the reported value. Other noticeable peaks between 2500 and 3500  $\text{cm}^{-1}$  are assigned due to symmetric and asymmetric vibration of C-CH<sub>2</sub> and C-NH<sub>2</sub> moieties. Two weak peaks at 1460 and 1260  $\text{cm}^{-1}$  arise due to vibration scissoring and symmetric bending of Si-CH<sub>2</sub>. No detectable signal is observed from the Si-H bond at 2100  $\text{cm}^{-1}$ .

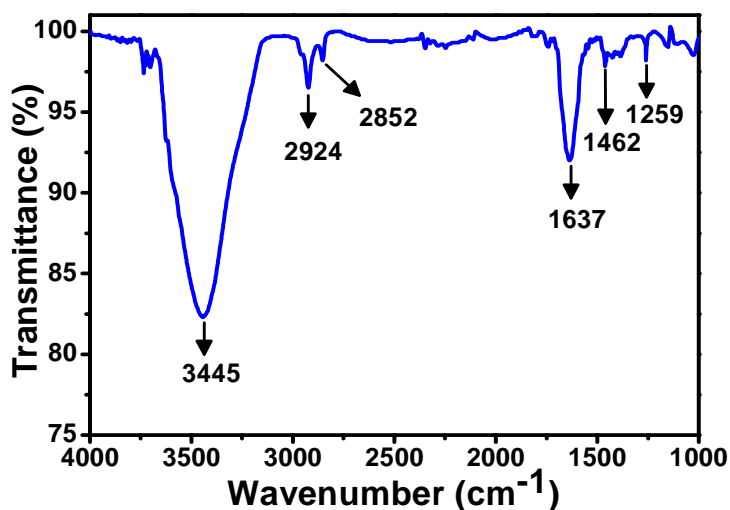


**Figure 3.1.** FTIR spectrum of synthesized allylamine-capped Si QDs.

The morphology and the mean size of the synthesized Si QDs are estimated from AFM measurements. The AFM image reveals the spherical nature of the synthesized Si QDs (Figure 3.2A). The size distribution histogram generated from the height profiles of 265 Si QDs gives a mean size of  $3.04 \pm 1.65$  nm (Figure 3.2B). The sizes of these Si QDs vary from 1.50 to 6.80 nm.

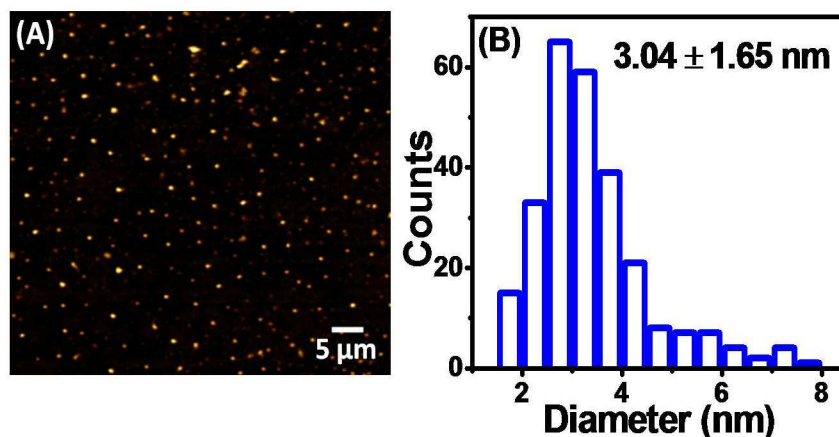


**Figure 3.2.** (A) AFM image and (B) size distribution histogram of allylamine-capped Si QDs.

The absorption spectrum of Si QDs shows a broad continuous absorption between 200 and 600 nm with two distinct shoulders at 265 and 310 nm (Figure 3.3), which is similar to that previously reported [19]. Excitation at 375 nm wavelength results in an intense PL band centered at 455 nm.

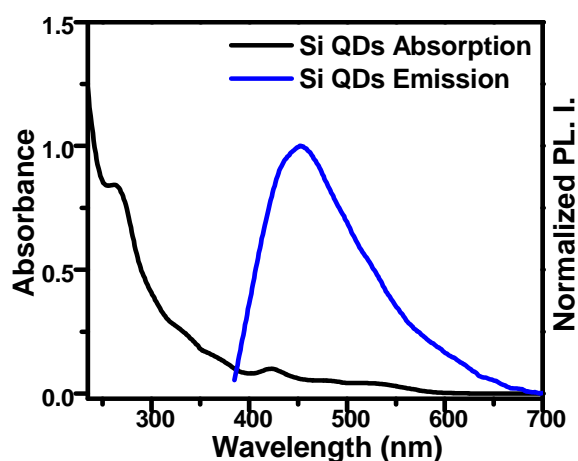


**Figure 3.3.** Absorption and PL ( $\lambda_{ex} = 375$  nm) spectra of Si QDs.

## Chapter 3

The synthesized citrate-capped silver nanoparticles (Ag NPs) were characterized by AFM, dynamic light scattering (DLS) and UV-Vis spectroscopy. Figure 3.4A displays the AFM image of as-synthesized citrate-capped Ag NPs. The AFM height profiles of two selected spherical Ag NPs are shown in the inset of Figure 3.4A. It is clear from the image that these Ag NPs are spherical in nature and the size varies from 38 to 82 nm. To estimate the mean hydrodynamic diameter of these Ag NPs, we performed DLS measurements. Figure 3.4B shows the size distribution histogram from DLS measurements. The diameter varies from 47 to 99 nm with a mean diameter of  $70 \pm 17$  nm. The absorption spectrum of Ag NPs is characterized by a strong LSPR band centered at 449 nm (Figure 3.4C). Here it is important to mention that the position of the LSPR peak is in accordance with the estimated mean size of synthesized Ag NPs [20]. These citrate-capped Ag NPs do not show any PL in bulk aqueous solution.

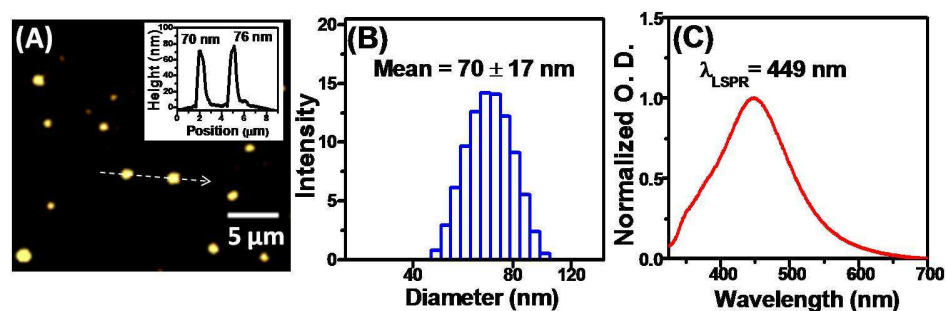


**Figure 3.4.** (A) AFM image of synthesized Ag NPs. The inset shows the height profile of two Ag NPs marked with an arrow. (B) The size distribution histogram of Ag NPs from DLS measurement. The mean hydrodynamic diameter is mentioned with the standard deviation. (C) The absorption spectrum of Ag NPs.

### 3.2.2. Interaction of Si QDs and Ag NPs with CTAB

The absorption spectrum of Si QDs remains unaltered in the presence of CTAB surfactant (Figure 3.5A). Previously, we have shown that allylamine functionalized Si QDs do not show any specific interactions with the positively charged CTAB surfactants in the concentration range of 0.1 to 2 mM at pH 7.6 [19]. However, significant spectral changes have been observed in the LSPR band of Ag NPs in the presence of CTAB surfactants (Figure 3.5A). In the absence of CTAB, the LSPR band of Ag NPs is centered at 449 nm. The peak position as well as the absorbance of Ag NPs change progressively upon gradual addition of CTAB upto a concentration of 0.5 mM (Figure 3.5A and B). In the presence of 0.5 mM CTAB, Ag NPs show a broad LSPR band centered at 504 nm with a 55 nm red shift (Figure 3.5A). Figure 3.5B shows the changes in LSPR peak intensity with CTAB concentrations in the range of 0 to 2 mM. It is important to note that both the peak position as well as the intensity of LSPR band saturate at 0.5 mM CTAB. Importantly, no such spectral changes of Ag NPs have been observed in the presence of negatively charged SDS and neutral TX 100 surfactants (Figure 3.5C and D).

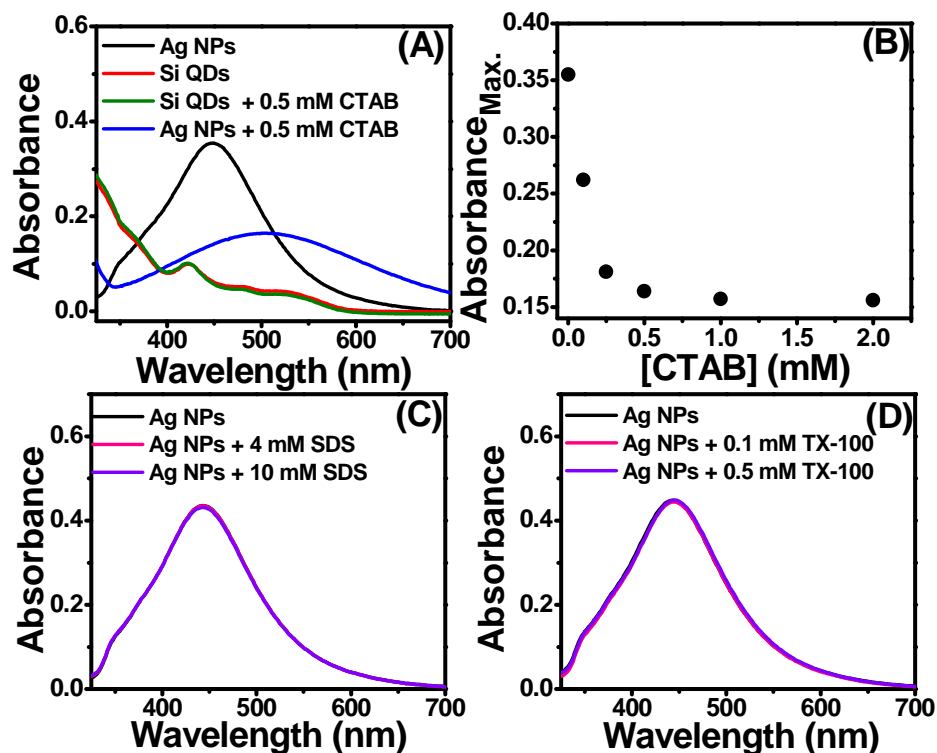


**Figure 3.5.** (A) Changes in the LSPR of Ag NPs (black and blue line) and absorption spectra of Si QDs (red and green line) in the presence of 0.5 mM CTAB. (B) The maximum absorbance of Ag NPs versus CTAB concentrations. Changes in the LSPR of Ag NPs upon addition of (C) SDS and (D) TX-100.

These spectral changes in the LSPR of Ag NPs in the presence of CTAB indicate the formation of surfactant-induced aggregates of Ag NPs. The noticeable amount of red shift observed with significant spectral broadening in the LSPR of Ag NPs can be attributed to the coupling of the surface plasmon of the closely spaced Ag NPs in the aggregates. Moreover, the absence of any such spectral changes in the presence of negatively charged SDS and neutral TX-100 surfactant indicate that the

aggregates are formed due to the specific electrostatic interactions between the negatively charged citrate molecules on the surface of Ag NPs and positively charged CTAB head groups. Previously, similar kind of spectral changes have been observed for different metal NPs in the presence of CTAB surfactant due to the formation of various types of surfactant-induced aggregates [21-23].

To get further insights into this surfactant-induced aggregation of Ag NPs, we performed DLS experiment. Figure 3.6A shows the size-distribution histogram of Ag NPs in the presence of 0.5 mM CTAB from DLS measurements. The sizes of Ag NPs vary from 96 to 305 nm with a mean hydrodynamic diameter of  $182 \pm 66$  nm. This increase in mean hydrodynamic diameter from  $70 \pm 17$  to  $182 \pm 66$  nm of Ag NPs in the presence of 0.5 mM CTAB clearly substantiates our claim that these Ag NPs undergo surfactant-induced random aggregation. Further evidence comes from zeta potential measurements. The estimated zeta potential of citrate-capped Ag NPs is -38 mV, while that in the presence of 0.5 mM CTAB shows a value of 4.3 mV (Figure 3.6B). This drastic change of zeta potential with reversal of surface charge indicates the presence of CTAB molecules on the surface of Ag NPs.

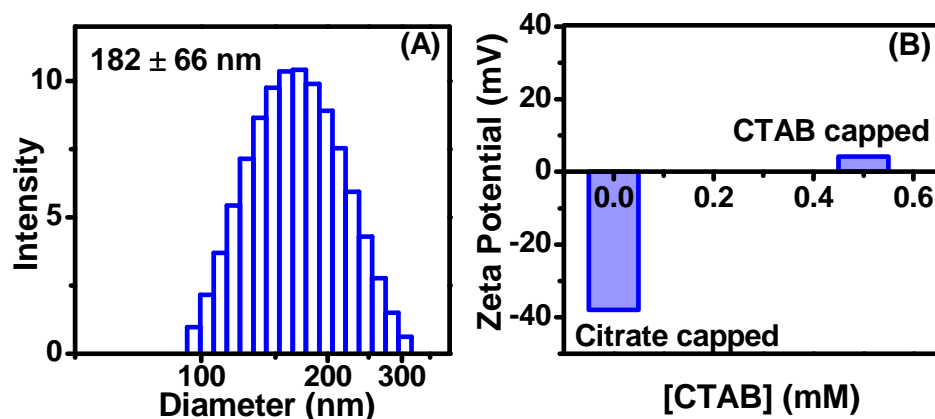
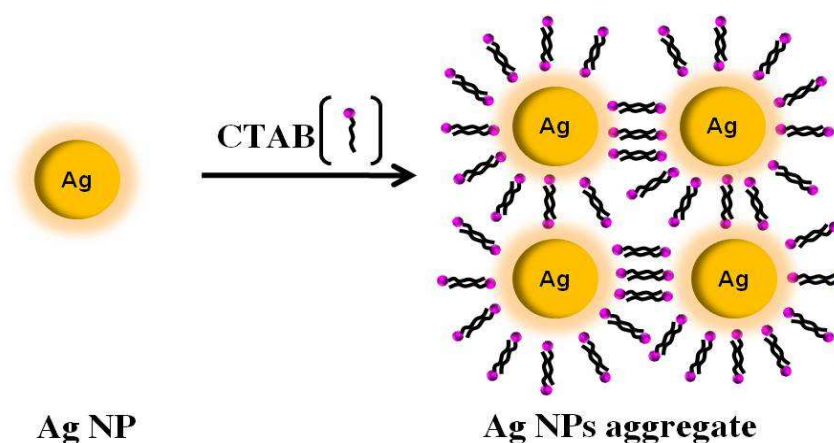


**Figure 3.6.** (A) Size distribution histogram of Ag NPs in the presence of 0.5 mM CTAB from DLS measurement. The mean diameter with standard deviation is mentioned in the figure. (B) The estimated zeta potentials of citrate-capped Ag NPs in the absence and presence of 0.5 mM CTAB.

Here it is important to comment on the structural arrangements of individual surfactant molecules on the surface of Ag NPs. The self-assembly of surfactant molecules on the surface of Ag NPs could result in either a micellar or a bilayer structure in the aqueous medium. In the micellar structure, a monolayer of surfactant encapsulates the Ag NPs, where the hydrophobic tails of surfactant molecules interact with the Ag NPs with their charged head groups faced toward the aqueous medium. However, in the present study, the micellar arrangements of CTAB surfactant are highly unlikely, as we have used citrate-capped Ag NPs and not the bare Ag NPs. Moreover, the absence of such aggregation in the presence of SDS and TX-100 surfactants indicates that the hydrophobic

interactions between hydrocarbon chains of surfactant and the surface of Ag NPs are negligible. A more realistic arrangement could be the formation of CTAB bilayer on the surface of Ag NPs due to the favorable electrostatic interactions. Moreover, CTAB bilayer can also act as a cross-linker between several Ag NPs to induce random aggregation. Previously, Nikoobakht et al. (2001) proposed similar kind of bilayer arrangements of CTAB surfactant on the Au NPs surface in which the inner layer is bound to the Au surface via the surfactant headgroups and is connected to the outer layer through hydrophobic interactions [21]. Similarly, Yang et al. (2007) have reported CTAB bilayer-induced aggregation and subsequent formation of silver nanochains on the glass slide [22]. Hence, on the basis of the previous literature and our present results, we propose a model where the citrate-capped Ag NPs are encapsulated by CTAB bilayer, which cross-links several such Ag NPs and results in aggregation (Scheme 3.1).



**Scheme 3.1.** Proposed model for CTAB bilayer-induced aggregation of Ag NPs.

Single-particle PL microscopy experiments have been performed to get the PL characteristics of individual Ag NPs in the absence and presence of CTAB. The synthesized Ag NPs do not show any luminescence in solution. This is in agreement with the previously reported results [24]. However, we have observed localized diffraction limited (FWHM  $\sim$ 1 to 2 pixels) luminescent spots when these Ag NPs are deposited on the air-glass interface. Figure 3.7A shows the PL image of Ag NPs on the glass coverslip. Most of these bright diffraction limited spots arise from PL of a single Ag NP. In addition, these localized luminescent spots show distinct luminescent blinking (fluorescence on/off) that persists over several minutes. Figure 3.7B shows the time traces of three selected luminescent spots. The random luminescence bursts observed in these time traces indicate the on-events from the citrate-capped Ag NPs. However, the number of luminescent spots decreases significantly in the presence of 0.5 mM CTAB. Figure 3.7C shows the PL image of Ag NPs in the presence of 0.5 mM CTAB. It is evident that in the presence of 0.5 mM CTAB, Ag NPs show very few bright and bigger sized luminescent spots with FWHM varying from 4 to 9 pixels. These luminescent spots of Ag NPs in the presence of CTAB do not show any characteristic luminescent blinking (Figure 3.7D). Importantly, it has been observed that each of these bright spots consists of several small luminescent spots.

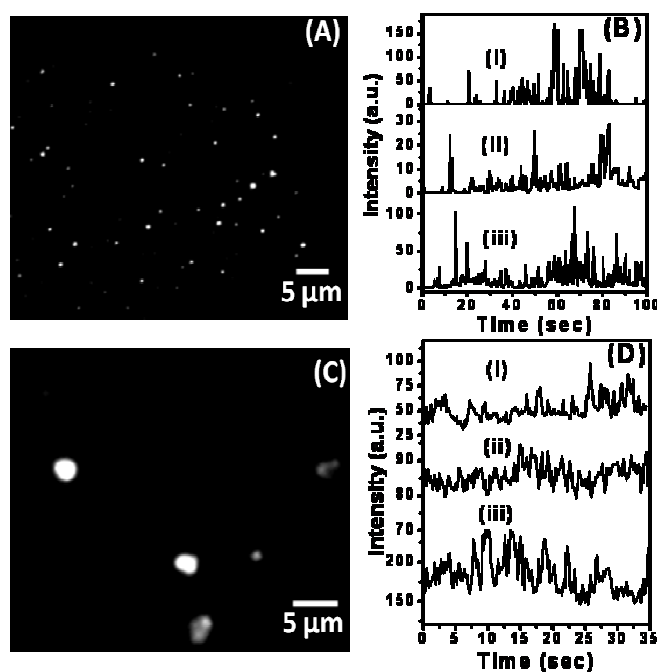


**Figure 3.7.** (A) PL image and (B) PL intensity profiles of Ag NPs. (C) PL image and (D) PL intensity profiles of Ag NPs in the presence of 0.5mM CTAB.

It is well-established that the luminescence of Ag NPs arises due to the formation of emitting Ag nanoclusters from silver oxides on the surface of Ag NPs [25-27]. Previously, it has been shown that only those nanoclusters that consist of 2 to 8 Ag atoms can show intense luminescence in the visible region of the electromagnetic spectrum [25]. Hence, the absence of luminescence from Ag NPs solution in the present study indicates the lack of silver oxide formation in solution. However, when these Ag NPs are deposited on the air-glass interface they exhibit intense luminescence due to the formation of silver oxides on the surface of Ag NPs which triggers photoactivated emission from Ag nanoclusters. In addition, the distinct luminescence bursts observed in the time traces of

Ag NPs indicate the on-events from these Ag nanoclusters. However, diffusion and subsequent aggregation of these Ag nanoclusters on the surface of Ag NPs result in the off-events due to the formation of non-luminescent Ag nanoclusters [23]. On the contrary, the bigger-sized non-blinking luminescent spots of Ag NPs in the presence of 0.5 mM CTAB arise due to the formation of surfactant-induced aggregates of Ag NPs. The absence of any distinct photon bursts clearly signifies the lack of silver oxide formation on the Ag NPs surface due to the presence of an extra surfactant bilayer on top of the citrate-capped Ag NPs. Moreover, the presence of multiple luminescent spots in each of these non-blinking bigger sized luminescent spot clearly justifies our earlier proposed model of CTAB bilayer-induced cross-linking of several Ag NPs.

### 3.2.3. Steady-State PL Quenching of Si QDs in the Presence of Ag NPs

Figure 3.8A shows excellent spectral overlap between PL spectrum of Si QDs ( $\lambda_{\text{ex}}= 375$  nm) and LSPR band of Ag NPs. Figure 3.8B displays the changes in absorption spectra of Si QDs in the presence of Ag NPs. It is evident that the LSPR of Ag NPs appears at 460 nm upon the addition of Ag NPs in the Si QDs solution. Si QDs show an intense PL band centered at 455 nm at an excitation wavelength of 375 nm (Figure 3.8C). The quantum yield of this band decreases significantly upon addition of Ag NPs (Figure 3.8C). Importantly, similar kind of PL quenching has been observed irrespective of the excitation wavelength in the range 375-460 nm. Here it is important to mention that the PL spectrum of Si QDs in the presence of Ag NPs was corrected for the absorbance at 375 nm, as the LSPR band of Ag NPs appears in the wavelength range of 320-700 nm [28]. A control experiment with only tri-sodium citrate dihydrate ligand shows no changes in the absorption and PL spectra of Si QDs (Figure

3.8D), which suggests that the surface of Ag NP interacts with Si QDs instead of the surface citrate ligands.

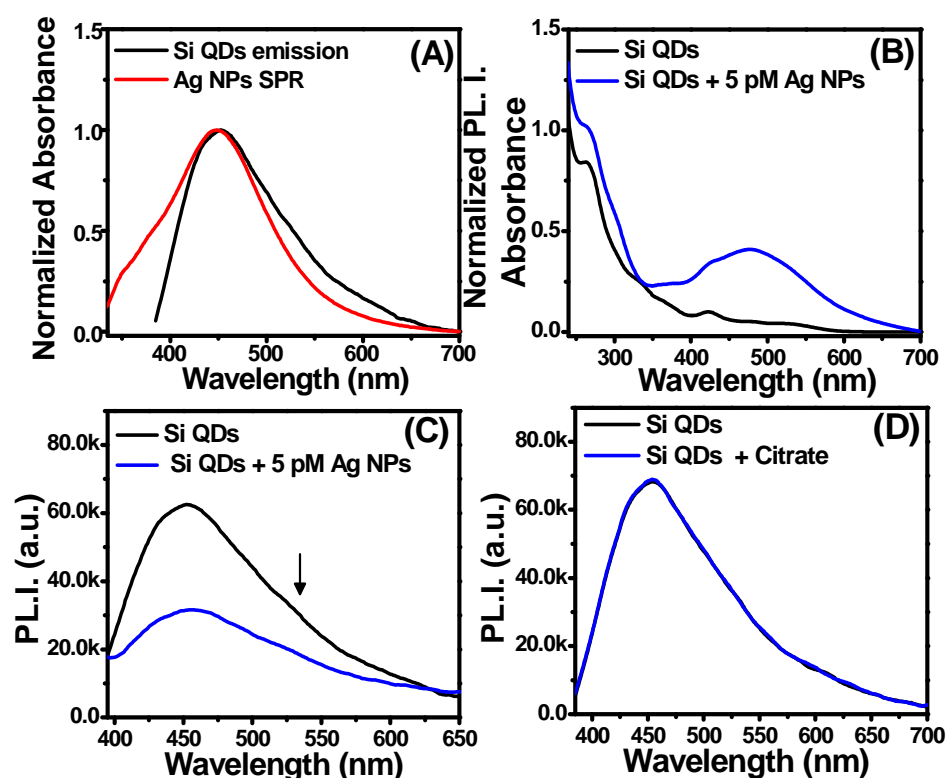


**Figure 3.8.** (A) Spectral overlap between PL spectrum ( $\lambda_{ex}=375$  nm) of Si QDs and LSPR band of Ag NPs. Changes in the (B) absorption spectra and (C) PL spectra ( $\lambda_{ex}=375$  nm) of Si QDs in the presence of 5 pM Ag NPs. (D) PL spectra of Si QDs in the presence of tri-sodium citrate dihydrate at an excitation wavelength of 375 nm.

However, negligible changes have been observed in the absorption spectrum of Si QDs upon addition of similar concentration of Ag NPs in the presence of 0.5 mM CTAB (Figure 3.9A). No noticeable LSPR band of Ag NPs has been observed from the nanocomposite solution in the presence of 0.5 mM CTAB. Moreover, negligible PL quenching of Si QDs

has been observed upon addition of Ag NPs in the presence of 0.5 mM CTAB (Figure 3.9B).

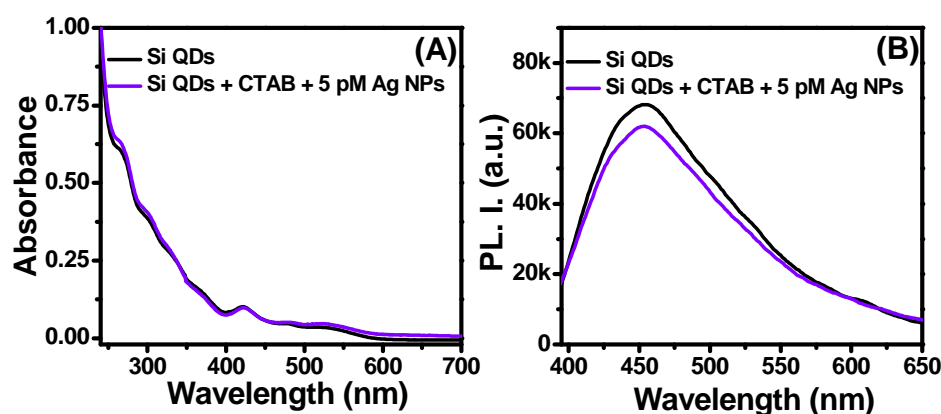


**Figure 3.9.** Changes in the (A) absorption spectra and (B) PL spectra ( $\lambda_{ex}=375$  nm) of Si QDs in the absence and presence of 5 pM Ag NPs with 0.5 mM CTAB.

The significant spectral overlap between the PL spectrum of Si QDs and LSPR band of Ag NPs signifies that the observed PL quenching of Si QDs in presence of Ag NPs might be due to EET from Si QDs to Ag NPs. Previously, it has been observed that noble metal NP acts as an efficient fluorescence quencher for various organic dyes and quantum dots [29-33]. Notably, the quenching efficiency of Ag NPs drastically reduces in the presence of 0.5 mM CTAB. This can be explained on the basis of the presence of an extra CTAB bilayer shell on the surface of these Ag NPs aggregates. As it has been previously discussed, these Ag NPs undergo surfactant-induced aggregation in the presence of 0.5 mM CTAB, where positively charged head groups of CTAB molecules interact with negatively charged citrate molecules at the Ag NPs surface. Our DLS results indicate that the CTAB molecules not only induce aggregation of

Ag NPs, but also provide an extra bilayer shell on top of the citrate-capped Ag NPs. As a result of this extra CTAB bilayer shell on the aggregated Ag NPs, the mean separation distance between Si QDs and the surface of Ag NPs increases. To further substantiate this claim and to establish the mechanism of EET from Si QDs to Ag NPs, we performed PL decay measurements.

### **3.2.4. Time-Resolved PL Quenching of Si QDs in the Presence of Ag NPs**

Figure 3.10A shows the PL decay traces of Si QDs in the absence and presence of Ag NPs monitored at 460 nm emission wavelength. All the decays were fitted with a three-exponential decay function. The average PL lifetime of Si QDs is  $0.84 \pm 0.03$  ns with lifetime components of 0.17 ns (74%), 1.24 ns (18%), and 6.14 ns (8%), which is very close to the previously reported value [19]. The addition of Ag NPs results in significant changes in the decay trace of Si QDs. The average lifetime decreases from  $0.84 \pm 0.03$  ns to  $0.37 \pm 0.01$  ns upon addition of 5 pM Ag NPs with lifetime components of 0.11 ns (86%), 0.75 ns (10%), and 4.77 ns (4%) (Table 3.1).

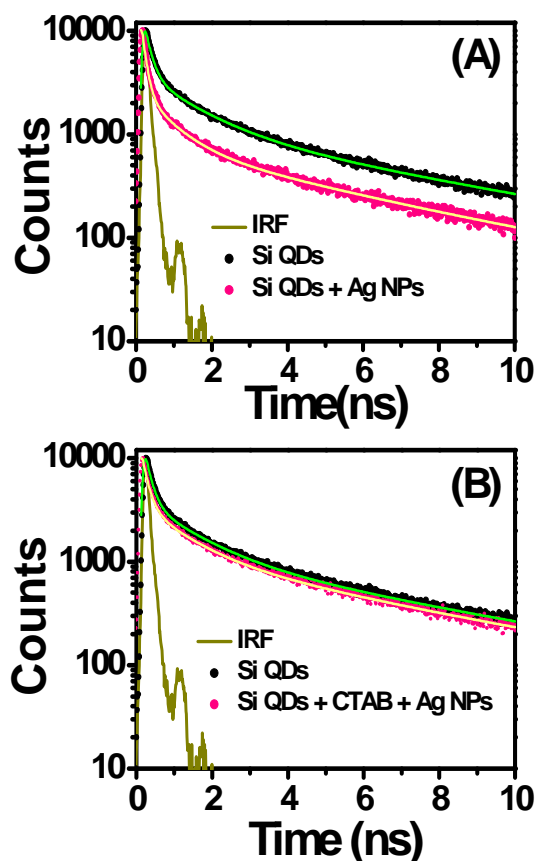


**Figure 3.10.** PL decay traces ( $\lambda_{ex} = 376 \text{ nm}$ ) of Si QDs in the absence and presence of (A) 5 pM Ag NPs and (B) 5 pM Ag NPs with 0.5 mM CTAB.

However, minimal changes have been observed in the PL decay traces of Si QDs with Ag NPs in the presence of 0.5 mM CTAB (Figure 3.10B). The average lifetime decreases marginally from  $0.84 \pm 0.03 \text{ ns}$  to  $0.74 \pm 0.02 \text{ ns}$  with lifetime components of 0.16 ns (76%), 1.07 ns (16%), and 5.58 ns (8%) (Table 3.1). The rate of EET is calculated from the average lifetime of Si QDs and has a value of  $1.51 \times 10^9 \text{ s}^{-1}$  and  $0.16 \times 10^9 \text{ s}^{-1}$  in the absence and presence of 0.5 mM CTAB, respectively (Table 3.2).

**Table 3.1.** PL decay parameters of Si QDs, and Si QDs with Ag NPs in the absence and presence of 0.5 mM CTAB.

System	$\tau_1$	$a_1$	$\tau_2$	$a_2$	$\tau_3$	$a_3$	$\langle\tau\rangle$	$\chi^2$
	(ns)		(ns)		(ns)		(ns)	
<b>Si QDs</b>	0.17	0.74	1.24	0.18	6.14	0.08	0.84	1.12
<b>+ Ag NPs</b>	0.11	0.86	0.75	0.10	4.77	0.04	0.37	1.20
<b>+ Ag NPs- CTAB</b>	0.16	0.76	1.07	0.16	5.58	0.08	0.74	1.12

It is well known that metal NPs influence the intrinsic radiative and nonradiative decay rates of nearby fluorophores [17, 34-41]. The shortened PL lifetime of Si QDs indicates that either the radiative or nonradiative decay rate is increased in the presence of Ag NPs. We have estimated the radiative and nonradiative decay rates of Si QDs in the presence of Ag NPs according to the following equations:

$$k_r = \frac{\phi_D}{\tau} \quad (1)$$

$$k_{nr} = \left(\frac{1-\phi_D}{\tau}\right) \quad (2)$$

where  $k_r$  and  $k_{nr}$  are the radiative and nonradiative decay rates, respectively.  $\phi_D$  is the quantum yield and  $\tau$  is the average lifetime of the donor. It is evident from Table 3.2 that the nonradiative decay rate of Si QDs increases by a factor of 2.34 in the presence of Ag NPs. Importantly, no appreciable change has been observed in the radiative decay rate of Si QDs upon addition of Ag NPs in the absence and presence of CTAB. Hence, the observed shortening of PL lifetime of Si QDs in the presence

## Chapter 3

of Ag NPs is due to the increased nonradiative decay rate rather than radiative decay rate. This increase in nonradiative decay rate in the presence of Ag NPs can be explained by considering the nonradiative EET from Si QDs to Ag NPs. Similarly, minimal but noticeable increase by a factor of 1.14 in the nonradiative decay rate of Si QDs has been observed upon addition of Ag NPs in the presence of 0.5 mM CTAB.

We have estimated the efficiency ( $\phi_{\text{Eff}}$ ) of this nonradiative EET process from the PL lifetimes of Si QDs in the presence and absence of Ag NPs using the following equation:

$$\phi_{\text{Eff}} = 1 - \frac{\tau_{\text{D-A}}}{\tau_{\text{D}}} \quad (3)$$

where  $\tau_{\text{D-A}}$  and  $\tau_{\text{D}}$  are the excited state lifetimes of Si QDs in the presence and absence of Ag NPs, respectively. It is evident from Table 3.2 that the efficiency of EET decreases significantly from 56% to 12% in the presence of 0.5 mM CTAB.

**Table 3.2.** *Estimated quantum yields, average lifetimes, radiative rates, nonradiative rates, energy transfer rates, and efficiency of energy transfer from Si QDs to Ag NPs in the absence and presence of CTAB.*

System	$\phi_{\text{D}}$	$\langle\tau\rangle$ (ns)	$k_{\text{r}}$ ( $\times 10^8 \text{ s}^{-1}$ )	$k_{\text{nr}}$ ( $\times 10^8 \text{ s}^{-1}$ )	$k_{\text{ET}}$ ( $\times 10^9 \text{ s}^{-1}$ )	$\phi_{\text{ET}}$
Si QDs	0.052	0.84	0.62	11.3	-	-
+ Ag NPs	0.024	0.37	0.64	26.4	1.51	0.56
+ Ag NPs- CTAB	0.047	0.74	0.63	12.9	0.16	0.12

### 3.2.5. Mechanism of EET from Si QDs to Ag NPs

To establish the mechanism behind this EET from the Si QDs to the Ag NPs, we have compared the experimentally obtained EET efficiencies with the theoretical curves calculated from NSET and FRET theory for the Si QDs-Ag NPs system. Persson's NSET theory is based on the collective interactions of all dipoles in a thin film near the metal surface and results in a  $1/d$  coupling instead of the conventional  $1/d^3$  coupling [16]. According to the NSET mechanism, the rate of EET can be expressed as

$$k_{\text{NSET}} = \frac{1}{\tau_{\text{D}}} \left( \frac{d_0}{d} \right)^4 \quad (4)$$

where  $\tau_{\text{D}}$  is the excited state lifetime of the donor in the absence of acceptor,  $d$  is the distance between the donor and surface of the acceptor, and  $d_0$  is the separation distance at which the energy transfer efficiency is 50%. The distance  $d_0$  can be calculated by using the following equation:

$$d_0 = \left( \frac{0.225 \phi_{\text{D}} c^3}{\omega_{\text{D}}^2 \omega_{\text{F}} k_{\text{F}}} \right)^{1/4} \quad (5)$$

where  $\phi_{\text{D}}$  is the quantum yield of the donor,  $c$  is the velocity of light,  $\omega_{\text{D}}$  is the angular frequency of the donor electronic transition,  $\omega_{\text{F}}$  is the Fermi frequency, and  $k_{\text{F}}$  is the Fermi wave vector of the metal. For the present system, the  $d_0$  value is calculated using  $\phi_{\text{D}} = 0.052$ ,  $c = 3 \times 10^{10} \text{ cm s}^{-1}$ ,  $\omega_{\text{D}} = 4.14 \times 10^{15} \text{ s}^{-1}$ ,  $\omega_{\text{F}} = 8.3 \times 10^{15} \text{ s}^{-1}$ , and  $k_{\text{F}} = 1.2 \times 10^8 \text{ cm}^{-1}$  [42]. The calculated  $d_0$  for the Si QDs-Ag NPs system is 3.81 nm. Similarly, the Förster distance  $R_0$  can be expressed as

$$R_0 = \left[ (8.8 \times 10^{-25}) (\kappa^2 \eta^{-4} \phi_{\text{D}} J(\lambda)) \right]^{1/6} \quad (6)$$

where  $\kappa^2$  is the orientation factor of the transition dipoles of the donor and the acceptor,  $\phi_D$  is the quantum yield of the donor,  $\eta$  is the refractive index of the medium, and  $J(\lambda)$  is the overlap integral between the donor emission and the acceptor absorption spectrum. For the present Si QDs-Ag NPs system, the calculated overlap integral is  $3.43 \times 10^{-8} \text{ M}^{-1} \text{ cm}^3$  and the estimated  $R_0$  is 26.55 nm. Here it is important to mention that for an ideal FRET pair, the typical Förster distance is in the range of 20-60 Å [43, 44]. Hence, for the present system the significantly higher value of  $R_0$  which is beyond the detection limit of FRET signifies that the present EET from Si QDs to Ag NPs does not follow the conventional FRET process.

On the basis of the estimated values of  $d_0$  and  $R_0$ , we have calculated the theoretical quenching efficiency as a function of distance according to the following equation

$$\phi_{\text{ET}} = \frac{1}{1 + \left(\frac{d}{d_0}\right)^n} \quad (7)$$

where  $\phi_{\text{ET}}$  is the energy transfer efficiency and  $d$  is the separation distance between Si QD and Ag NP.  $n$  is a factor which depends on the mechanism of energy transfer and has a value of either 6 or 4 for the FRET and NSET model, respectively. In the case of FRET,  $d_0$  is equal to  $R_0$ . Figure 3.11 shows the theoretical plots of the quenching efficiency against the separation distance based on the NSET and FRET theory. Experimentally obtained quenching efficiencies in the absence and presence of CTAB are shown on the Y-axis of Figure 3.11.

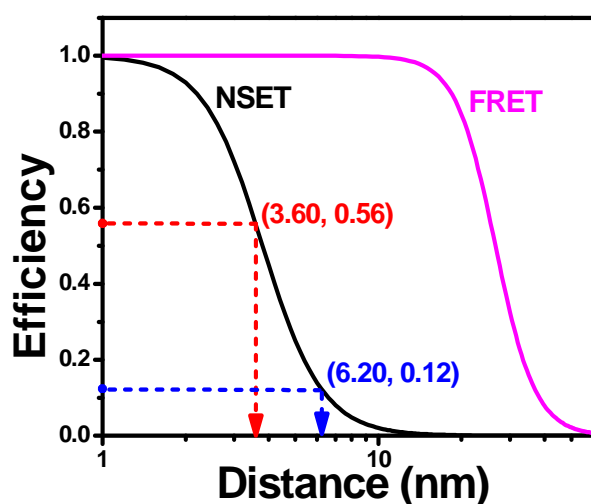
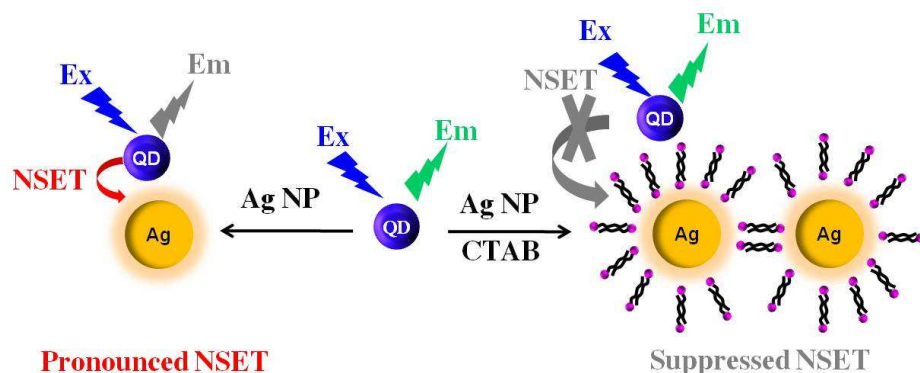


**Figure 3.11.** Correlation between experimentally obtained EET efficiencies for the Si QDs-Ag NPs system in the absence (red point) and presence (blue point) of 0.5 mM CTAB with the theoretical curves generated from NSET (black line) and FRET (magenta line) theory.

The estimated separation distance between Si QDs and the surface of Ag NPs is 3.60 and 6.20 nm in the absence and presence of 0.5 mM CTAB. This increase in distance in the presence of CTAB can only be explained if we consider the presence of CTAB bilayer shell on the surface of Ag NPs aggregates. The reported end to end length of CTAB is  $\sim 2.0$  nm and the measured thickness of CTAB bilayer at 0.5 mM concentration is  $\sim 2.99$  nm [45, 46]. Hence the observed 2.60 nm increase in separation distance between Si QDs and the surface of Ag NPs in the presence of 0.5 mM CTAB concentration strongly substantiate the presence of CTAB bilayer on the surface of Ag NPs. These obtained distances which correlate well with our proposed model strongly suggest that the observed EET quenching for the present system is due to the nanometal surface energy transfer from Si QDs to Ag NPs surface. Hence,

on the basis of our obtained results we propose that the long-range interactions between Si QDs and Ag NPs result in pronounced NSET, while in the presence of 0.5 mM CTAB, Ag NPs form CTAB bilayer-capped aggregates and as a result the efficiency of NSET decreases significantly due to the increased distance between Si QDs and the surface of Ag NPs (Scheme 3.2). Moreover, our present results demonstrate that it is possible to modulate the NSET efficiency from Si QDs to Ag NPs by tuning the nanoscale distance between them with simple surfactant molecules.



**Scheme 3.2.** Schematic illustration of the CTAB-induced modulation of the NSET between Si QDs and Ag NPs.

### 3.3. Conclusions

In summary, the observed PL quenching of Si QDs in the presence of Ag NPs is mainly due to the EET from Si QDs to the surface of Ag NPs. The quenching in steady-state PL yield as well as in the excited state lifetime of Si QDs in the presence of Ag NPs arises due to the increased nonradiative decay rate, while the radiative decay rate remains almost constant. The experimentally estimated quenching efficiency from the lifetime data correlates well with the NSET mechanism rather than FRET

mechanism. The drastic reduction in the EET efficiency observed in the presence of 0.5 mM CTAB is due to the increased distance between Si QDs and the surface of Ag NPs as a result of an extra CTAB bilayer in the CTAB-induced aggregates of Ag NPs.

### 3.4. References

1. Trinh C., Kirlikovali K. O., Bartynski A. N., Tassone C. J., Toney M. F., Burkhard G. F., McGehee M. D., Djurovich P. I., Thompson M. E. (2013), Efficient energy sensitization of C<sub>60</sub> and application to organic photovoltaics, *J. Am. Chem. Soc.*, 135, 11920-11928. (DOI: 10.1021/ja4043356)
2. Nimmo M. T., Caillard L. M., Benedetti W. D., Nguyen H. M., Seitz O., Gartstein Y. N., Chabal Y. J., Malko A. V. (2013), Visible to near-infrared sensitization of silicon substrates via energy transfer from proximal nanocrystals: Further insights for hybrid photovoltaics, *ACS Nano*, 7, 3236-3245. (DOI: 10.1021/nm400924y)
3. Lee B. R., Lee W., Nguyen T. L., Park J. S., Kim J. S., Kim J. Y., Woo H. Y., Song M. H. (2013), Highly efficient red-emitting hybrid polymer light-emitting diodes via Förster resonance energy transfer based on homogeneous polymer blends with the same polyfluorene backbone, *ACS Appl. Mater. Interfaces*, 5, 5690-5695. (DOI: 10.1021/am401090m)
4. Volyniuk D., Cherpak V., Stakhira P., Minaev B., Baryshnikov G., Chapran M., Tomkeviciene A., Keruckas J., Grazulevicius J. V. (2013), Highly efficient blue organic light-emitting diodes based on intermolecular triplet-singlet energy transfer, *J. Phys. Chem. C*, 117, 22538-22544. (DOI: 10.1021/jp407397y)
5. Dennis A. M., Rhee W. J., Sotto D., Dublin S. N., Bao G. (2012), Quantum dot-fluorescent protein FRET probes for sensing intracellular pH, *ACS Nano*, 6, 2917-2924. (DOI: 10.1021/nm2038077)

6. Lee Y. H., Lee M. H., Zhang J. F., Kim J. S. (2010), Pyrene excimer-based calix[4]arene FRET chemosensor for mercury(II), *J. Org. Chem.*, 75, 7159-7165. (DOI: 10.1021/jo101113f)
7. Yuan L., Lin W., Zheng K., Zhu S. (2013), FRET-based small-molecule fluorescent probes: Rational design and bioimaging applications, *Acc. Chem. Res.*, 46, 1462-1473. (DOI: 10.1021/ar300273v)
8. Vafabakhsh R., Ha T. (2012), Extreme bendability of DNA less than 100 base pairs long revealed by single-molecule cyclization, *Science*, 337, 1097-1101. (DOI: 10.1126/science.1224139)
9. Clapp A. R., Medintz I. L., Mauro J. M., Fisher B. R., Bawendi M. G., Mattoussi H. (2004), Fluorescence resonance energy transfer between quantum dot donors and dye-labeled protein acceptors, *J. Am. Chem. Soc.*, 126, 301-310. (DOI: 10.1021/ja037088b)
10. Medintz I. L., Clapp A. R., Mattoussi H., Goldman E. R., Fisher B., Mauro J. M. (2003), Self-assembled nanoscale biosensors based on quantum dot FRET donors, *Nat. Mater.*, 2, 630-638. (DOI: 10.1038/nmat961)
11. Naiki H., Masuhara A., Masuo S., Onodera T., Kasai H., Oikawa H. (2013), Highly controlled plasmonic emission enhancement from metal-semiconductor quantum dot complex nanostructures, *J. Phys. Chem. C*, 117, 2455-2459. (DOI: 10.1021/jp305408p)
12. Li M., Cushing S. K., Wang Q., Shi X., Hornak L. A., Hong Z., Wu N. (2011), Size-dependent energy transfer between CdSe/ZnS

quantum dots and gold nanoparticles, *J. Phys. Chem. Lett.*, 2, 2125-2129. (DOI: 10.1021/jz201002g)

13. Sen T., Patra A. (2012), Recent advances in energy transfer processes in gold-nanoparticle-based assemblies, *J. Phys. Chem. C*, 116, 17307-17317. (DOI: 10.1021/jp302615d)

14. Quach A. D., Crivat G., Tarr M. A., Rosenzweig Z. (2011), Gold nanoparticle-quantum dot-polystyrene microspheres as fluorescence resonance energy transfer probes for bioassays, *J. Am. Chem. Soc.*, 133, 2028-2030. (DOI: 10.1021/ja109348d)

15. Chance R. R., Prock A., Silbey R. (1978), Molecular fluorescence and energy transfer near interfaces, *Adv. Chem. Phys.*, 37, 1-65. (DOI: 10.1002/9780470142561.ch1)

16. Persson B. N. J., Lang N. D. (1982), Electron-hole-pair quenching of excited states near a metal, *Phys. Rev. B*, 26, 5409-5415. (DOI: 10.1103/PhysRevB.26.5409)

17. Jennings T. L., Singh M. P., Strouse G. F. (2006), Fluorescent lifetime quenching near  $d=1.5$  nm gold nanoparticles: Probing NSET validity, *J. Am. Chem. Soc.*, 128, 5462-5467. (DOI: 10.1021/ja0583665)

18. Haldar K. K., Sen T., Patra A. (2010), Metal conjugated semiconductor hybrid nanoparticle-based fluorescence resonance energy transfer, *J. Phys. Chem. C*, 114, 4869-4874. (DOI: 10.1021/jp911348n)

19. Chatterjee S., Mukherjee T. K. (2013), Size-dependent differential interaction of allylamine-capped silicon quantum dots with surfactant assemblies studied using photoluminescence spectroscopy and imaging technique, *J. Phys. Chem. C*, 117, 10799-10808. (DOI: 10.1021/jp402408d)
20. Paramelle D., Sadovoy A., Gorelik S., Free P., Hobley J., Fernig D. G. (2014), A rapid method to estimate the concentration of citrate capped silver nanoparticles from UV-Visible light spectra, *Analyst*, 139, 4855-4861. (DOI: 10.1039/C4AN00978A)
21. Nikoobakht B., El-Sayed M. A. (2001), Evidence for bilayer assembly of cationic surfactants on the surface of gold nanorods, *Langmuir*, 17, 6368-6374. (DOI: 10.1021/la010530o)
22. Yang Y., Shi J., Tanaka T., Nogami M. (2007), Self-assembled silver nanochains for surface-enhanced Raman scattering, *Langmuir*, 23, 12042-12047. (DOI: 10.1021/la701610s)
23. Sun L., Zhao D., Ding M., Xu Z., Zhang Z., Li B., Shen D. (2011), Controlled synthesis of silver nanoparticle aggregates for surface-enhanced Raman scattering studies, *J. Phys. Chem. C*, 115, 16295-16304. (DOI: 10.1021/jp205545g)
24. Wu X., Yeow E. K. L. (2008), Fluorescence blinking dynamics of silver nanoparticle and silver nanorod films, *Nanotechnology*, 19, 035706. (DOI: 10.1088/0957-4484/19/03/035706)
25. Peyser L. A., Vinson A. E., Bartko A. P., Dickson R. M. (2001), Photoactivated fluorescence from individual silver nanoclusters, *Science*, 291, 103-106. (DOI: 10.1126/science.291.5501.103)

## Chapter 3

---

26. Zheng J., Dickson R. M. (2002), Individual water-soluble dendrimer-encapsulated silver nanodot fluorescence, *J. Am. Chem. Soc.*, 124, 13982-13983. (DOI: 10.1021/ja028282i)
27. Geddes C. D., Parfenov A., Gryczynski I., Lakowicz J. R. (2003), Luminescent blinking from silver nanostructures, *J. Phys. Chem. B*, 107, 9989-9993. (DOI: 10.1021/jp030290g)
28. Birdsall B., King R. W., Wheeler M. R., Lewis C. A. Jr., Goode S. R., Dunlap B., Roberts G. C. K. (1983), Correction for light absorption in fluorescence studies of protein-ligand interactions, *Anal. Biochem.*, 132, 353-361. (DOI: 10.1016/0003-2697(83)90020-9)
29. Kuhnke K., Becker R., Epple M., Kern K. (1997), C<sub>60</sub> exciton quenching near metal surfaces, *Phys. Rev. Lett.*, 79, 3246-3249. (DOI: 10.1103/PhysRevLett)
30. Dulkeith E., Morteani A. C., Niedereichholz T., Klar T. A., Feldmann J., Levi S. A., van Veggel F. C. J. M., Reinhoudt D. N., Moller M., Gittins D. I. (2002), Fluorescence quenching of dye molecules near gold nanoparticles: Radiative and nonradiative effects, *Phys. Rev. Lett.*, 89, 203002. (DOI: 10.1103/PhysRevLett.89.203002)
31. Dulkeith E., Ringler M., Klar T. A., Feldmann J., Muñoz Javier A., Parak W. J. (2005), Gold nanoparticles quench fluorescence by phase induced radiative rate suppression, *Nano Lett.*, 5, 585-589. (DOI: 10.1021/nl0480969)
32. Cannone F., Chirico G., Bizzarri A. R., Cannistraro S. (2006), Quenching and blinking of fluorescence of a single dye molecule

bound to gold nanoparticles, *J. Phys. Chem. B*, 110, 16491-16498. (DOI: 10.1021/jp0625816)

33. Kim K. S., Kim J. H., Kim H., Laquai F., Arifin E., Lee J. K., Yoo S., Sohn B. H. (2012), Switching off FRET in the hybrid assemblies of diblock copolymer micelles, quantum dots, and dyes by plasmonic nanoparticles, *ACS Nano*, 6, 5051-5059. (DOI: 10.1021/nm301893e)

34. Shimizu K. T., Woo W. K., Fisher B. R., Eisler H. J., Bawendi M. G. (2002), Surface-enhanced emission from single semiconductor nanocrystals, *Phys. Rev. Lett.*, 89, 117401. (DOI: 10.1103/PhysRevLett.89.117401)

35. Kühn S., Håkanson U., Rogobete L., Sandoghdar V. (2006), Enhancement of single-molecule fluorescence using a gold nanoparticle as an optical nanoantenna, *Phys. Rev. Lett.*, 97, 017402. (DOI: 10.1103/PhysRevLett.97.017402)

36. Chen Y., Munechika K., Ginger D. S. (2007), Dependence of fluorescence intensity on the spectral overlap between fluorophores and plasmon resonant single silver nanoparticles, *Nano Lett.*, 7, 690-696. (DOI: 10.1021/nl062795z)

37. Munechika K., Chen Y., Tillack A. F., Kulkarni A. P., Plante I. J. L., Munro A. M., Ginger, D. S. (2010), Spectral control of plasmonic emission enhancement from quantum dots near single silver nanoprisms, *Nano Lett.*, 10, 2598-2603. (DOI: 10.1021/nl101281a)

38. Pan S. L., Wang Z. J., Rothberg L. J. (2006), Enhancement of adsorbed dye monolayer fluorescence by a silver nanoparticle overlayer, *J. Phys. Chem. B*, 110, 17383-17387.
39. Xie F., Baker M. S., Goldys E. M. (2006), Homogeneous silver-coated nanoparticle substrates for enhanced fluorescence detection, *J. Phys. Chem. B*, 110, 23085-23091. (DOI: 10.1021/jp062170p)
40. Thomas K. G., Kamat P. V. (2000), Making gold nanoparticles glow: Enhanced emission from a surface-bound fluoroprobe, *J. Am. Chem. Soc.*, 122, 2655-2656. (DOI: 10.1021/ja9941835)
41. Yun C. S., Javier A., Jennings T., Fisher M., Hira S., Peterson S., Hopkins B., Reich N. O., Strouse, G. F. (2005), Nanometal surface energy transfer in optical rulers, breaking the FRET barrier, *J. Am. Chem. Soc.*, 127, 3115-3119. (DOI: 10.1021/ja043940i)
42. Saraswat S., Desireddy A., Zheng D., Guo L., Lu H. P., Bigioni T. P., Isailovic D. (2011), Energy transfer from fluorescent proteins to metal nanoparticles, *J. Phys. Chem. C*, 115, 17587-17593. (DOI: 10.1021/jp2029246)
43. Lakowicz J. R., (1999), *Principles of fluorescence spectroscopy*, 2nd ed., Academic Press, New York. (ISBN: 0-306-46093-9)
44. Mandal S., Ghatak C., Rao V. G., Ghosh S., Sarkar N. (2012), Pluronic micellar aggregates loaded with gold nanoparticles (Au NPs) and fluorescent dyes: A study of controlled nanometal surface energy transfer, *J. Phys. Chem. C*, 116, 5585-5597. (DOI: 10.1021/jp2093127)

45. Jr. Hubbard F. P., Abbott N. L. (2008), A small angle neutron scattering study of the thickness of vesicle bilayers formed from mixtures of alkyl sulfates and cationic bolaform surfactants, *Soft Matter*, 4, 2225-2231. (DOI: 10.1039/b801981a)
46. Speranza F., Pilkington G. A., Dane T. G., Cresswell P. T., Li P., Jacobs R. M. J., Arnold T., Bouchenoire L., Thomas R. K., Briscoe W. H. (2013), Quiescent bilayers at the mica-water interface, *Soft Matter*, 9, 7028-7041. (DOI: 10.1039/c3sm50336d)



**Chapter 4**

*Resonant Excitation Energy Transfer  
from Carbon Dots to Different Sized  
Silver Nanoparticles*

### 4.1. Introduction

Noble metal nanoparticles (NPs) with characteristic localized surface plasmon resonances (LSPRs) have attracted considerable attention in the past few decades due to their potential applications in miniature optical devices, sensors, medical diagnostics and therapeutics [1-4]. It has often been observed that noble metal NPs with distinct LSPR significantly alter the emission properties of nearby fluorophores. This phenomenon is either observed as enhancement or quenching of the fluorescence quantum yield of nearby fluorophores. The enhancement occurs either due to an increase in the radiative decay rate of fluorophores or the enhanced electromagnetic field at the NP surface [5-8]. On the other hand, fluorescence quenching in the presence of metal NPs is due to modulation of either a radiative or a nonradiative decay or both [9-12].

The luminescence quenching mechanism of various dyes and quantum dots in the presence of metal NPs has been extensively studied, to understand the dipole to the metal surface energy transfer which is known as nanometal surface energy transfer (NSET). This is quite different from the conventional Förster resonance energy transfer (FRET) between two molecular dyes via dipole-dipole interaction [9, 11, 13-17]. Earlier, Pons et al. (2007) demonstrated the validity of the NSET mechanism for the excitation energy transfer (EET) from CdSe/ZnS QDs to gold NPs (Au NPs) separated via a variable-length polypeptide [14]. Similarly, Breshike et al. (2013) studied the distance-dependent NSET from various fluorophores to different sized Au NPs [15]. Although these earlier studies are very informative and describe the NSET mechanism from various donors to different nanometal surfaces in detail, the role of spectral overlap in the NSET process still remains obscure.

It has often been observed that energy transfer processes involving a significant spectral overlap follow the FRET mechanism, while processes having no spectral overlap follow the NSET mechanism. Earlier, Strouse and co-workers (2005 and 2006) demonstrated NSET from various dyes to ultrasmall Au NPs (< 2 nm) having no noticeable LSPR band [9, 11]. In another study, Saraswat et al. (2011) showed that the spectral overlap plays no role in NSET from fluorescent proteins to Au and Ag NPs [18]. In contrast, a number of recent studies have shown that the NSET mechanism can still be valid for a donor-acceptor pair having a significant spectral overlap. For example, Singh et al. (2010) have recently demonstrated the importance of spectral overlap in the NSET process from various dyes to 2 nm sized Au NPs [19]. While substantial efforts have been made to understand the PL quenching of various fluorophores near the metal surface, a direct correlation between the extent of NSET from carbon dots (CDs) to Ag NPs with the particle size and spectral overlap has not been explored yet.

In the present study, we have investigated the effect of three different sized Ag NPs having a distinct LSPR band on the PL properties of nearby CDs and shown that the PL quenching of CDs is due to the nonradiative NSET from CDs to Ag NPs. Moreover, it has been observed that the EET efficiency increases with the increase in the size of Ag NPs.

## 4.2. Results and Discussion

### 4.2.1. Characterization of CDs and Ag NPs

Figure 4.1A shows the FTIR spectrum of CDs. The peak near 3420  $\text{cm}^{-1}$  arises due to the stretching vibrations of O-H and N-H moieties. The two characteristic peaks at 2925  $\text{cm}^{-1}$  and 1394  $\text{cm}^{-1}$  are assigned to the

stretching and bending vibrations of C-H moieties. Another prominent peak at  $1690\text{ cm}^{-1}$  arises due to the stretching vibration of C=O functional groups. The peak at  $1566\text{ cm}^{-1}$  arises from the bending vibration of the N-H moieties. Figure 4.1B shows the HRTEM image of synthesized CDs on a holey carbon lacey grid. It is evident that these CDs are spherical in shape with a mean size of  $3.80\text{ nm}$ . The inset of Figure 4.1B displays the magnified image of a single CD. Figure 4.1C shows the size distribution histogram of CDs from DLS measurements. The mean hydrodynamic diameter was estimated to be  $4.14\text{ nm}$ .

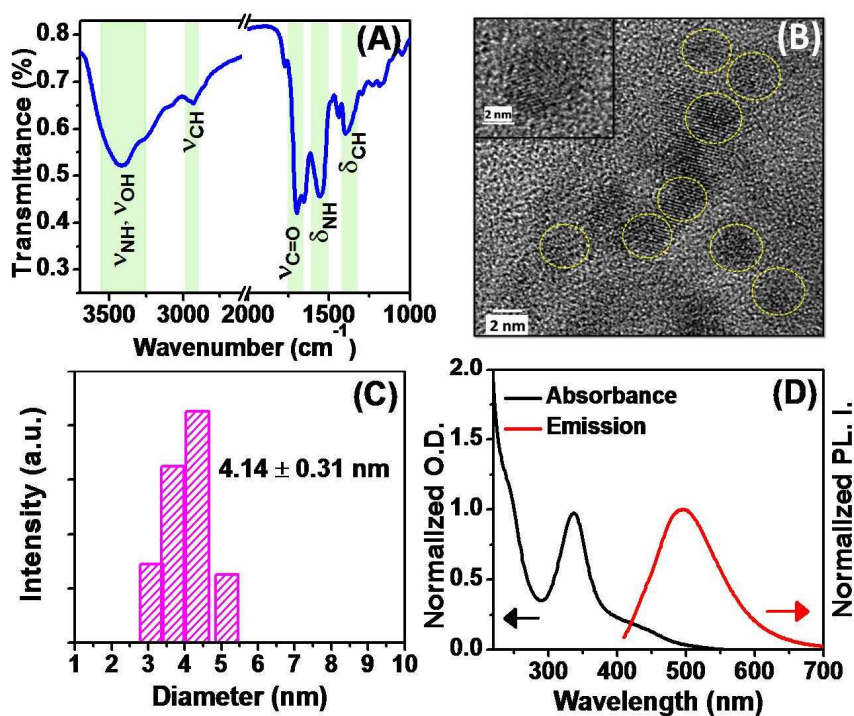


**Figure 4.1.** (A) FTIR spectrum, (B) HRTEM image, the inset shows the magnified image of single CD, (C) size distribution histogram of CDs from DLS measurements, and (D) normalized absorption (black line) and PL spectra (red line) of CDs at  $\lambda_{ex} = 400\text{ nm}$ .

The estimated zeta potential of these CDs is  $-25.45 \pm 1.23$  mV at pH 7.4. Figure 4.1D shows the absorption and PL spectra ( $\lambda_{\text{ex}} = 400$  nm) of the synthesized CD in pH 7.4 phosphate buffer. A prominent absorption peak at 337 nm is observed due to  $n-\pi^*$  transitions from C=O bond of CD [20, 21]. A weak shoulder near 240 nm appears due to the  $\pi - \pi^*$  transitions from the core of CD [21]. These CDs show an intense PL band centered at 495 nm upon excitation at 400 nm (Figure 4.1D). The elemental analysis reveals the composition of these synthesized CDs with 53.18% carbon, 14.13% nitrogen, 5.72% hydrogen and 26.97% oxygen (Figure 4.2A). Figure 4.2B displays the powder XRD spectrum of CDs. A broad peak at  $2\theta = 25^\circ$  ( $d = 0.35$  nm), which exactly matches with the earlier reported value signifies the amorphous nature of these CDs [20].

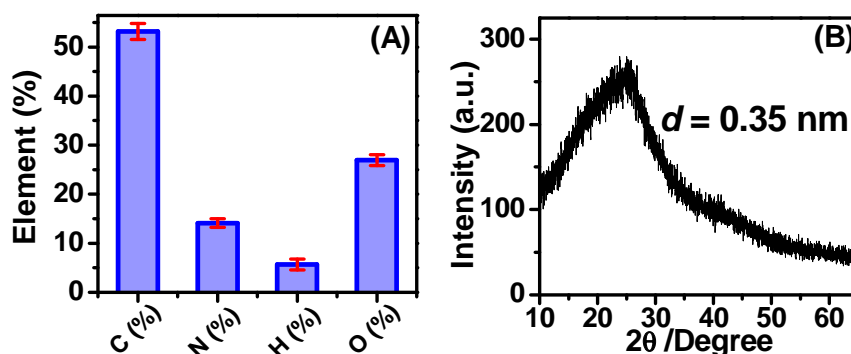


**Figure 4.2.** (A) The elemental analysis histogram and (B) powder XRD spectrum of the synthesized CDs.

For the present study, we have synthesized three different sized citrate-capped Ag NPs. The morphologies and mean hydrodynamic diameters of these three different sized Ag NPs are estimated from SEM and DLS measurements, respectively. The mean diameters estimated from

SEM measurements for smallest (s), medium (m) and largest (l) Ag NPs are  $36.58 \pm 2.98$ ,  $48.26 \pm 3.16$  and  $57.93 \pm 2.64$  nm, respectively (Figure 4.3A). The SEM images reveal spherical morphologies of all the three different sized Ag NPs (insets of Figure 4.3A).

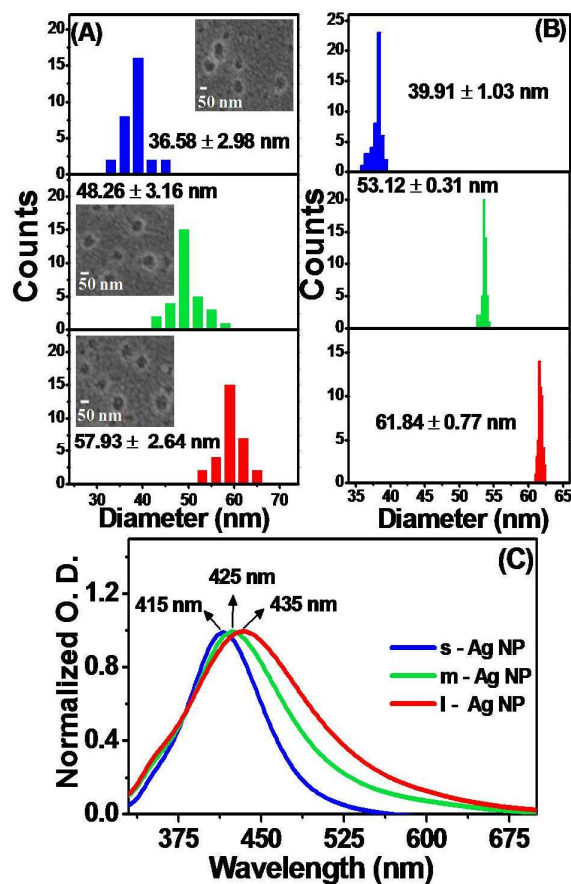


**Figure 4.3.** (A) Size distribution histograms estimated from SEM measurements for s-Ag NP (blue), m-Ag NP (green) and l-Ag NP (red). The inset of each graph shows SEM image of respective Ag NP. (B) The hydrodynamic size distribution histogram of synthesized s-, m- and l-Ag NPs estimated from DLS measurements. (C) Normalized LSPR of s-, m- and l-Ag NPs.

Figure 4.3B shows the size distribution histograms obtained from DLS measurements for the three different sized Ag NPs. The estimated mean hydrodynamic diameters of s-, m- and l-Ag NPs are  $39.91 \pm 1.03$ ,  $53.12 \pm 0.31$  and  $61.84 \pm 0.77$  nm, respectively. The LSPR bands of s-, m-, and l-Ag NPs are centered at 415, 425 and 435 nm, respectively (Figure 4.3C). These citrate-capped Ag NPs do not show any PL in bulk aqueous solution. The zeta potential of s-, m-, and l-Ag NPs is estimated to be  $-76.24 \pm 3.92$ ,  $-67.60 \pm 4.40$  and  $-58.01 \pm 3.10$  mV, respectively.

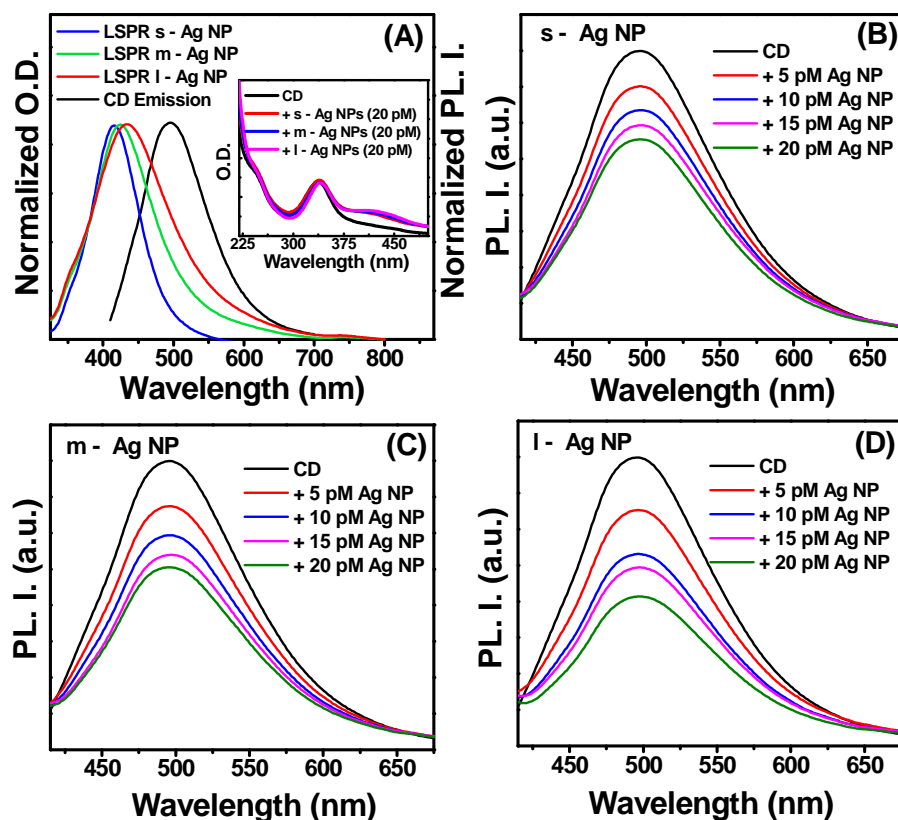
#### 4.2.2. Steady-State PL Measurements of CD in the Presence of Ag NPs

Figure 4.4A shows the extent of spectral overlap between LSPR of three different sized Ag NPs and the PL spectrum of CDs ( $\lambda_{\text{ex}} = 400$  nm). The spectral overlap integrals for the three different CD-Ag NP systems have been calculated using the following equation:

$$J(\lambda) = \frac{\int_0^{\infty} F_D(\lambda)\varepsilon_A(\lambda)\lambda^4 d\lambda}{\int_0^{\infty} F_D(\lambda) d\lambda} \quad (1)$$

where  $F_D(\lambda)$  is the PL intensity of CD in the wavelength range  $\lambda + \Delta\lambda$  with total intensity (area under the curve) normalized to unity,  $\varepsilon_A(\lambda)$  is the molar extinction coefficient of Ag NP at  $\lambda$ . The estimated values of the spectral overlap integral for CD-Ag NP system are  $1.52 \times 10^{-8}$ ,  $4.83 \times 10^{-8}$ , and  $11 \times 10^{-8} \text{ M}^{-1} \text{ cm}^3$  for s, m, and l- Ag NPs, respectively. Hence, it is evident from these results that the spectral overlap integral increases with the increase in the size of Ag NPs. The inset of Figure 4.4A shows the changes in the absorption spectrum of CD upon addition of 20 pM s-, m-, and l-Ag NPs. The characteristic LSPR of Ag NPs appears in the absorption spectrum of CDs upon addition of different sized Ag NPs. The PL intensity ( $\lambda_{\text{ex}} = 400$  nm) of CDs decreases gradually upon increasing

the concentrations of Ag NPs (Figure 4.4B-D). Here it is important to mention that a similar kind of PL quenching of CDs has been observed irrespective of the excitation wavelength in the range of 340-400 nm.



**Figure 4.4.** (A) Spectral overlap between LSPR bands of different sized Ag NPs and PL spectrum ( $\lambda_{ex} = 400$  nm) of CDs. The inset shows the changes in the absorption spectra of CDs in the presence of 20 pM s-, m-, and l-Ag NPs. Changes in the PL spectra ( $\lambda_{ex} = 400$  nm) of CDs upon addition of (B) s-, (C) m-, and (D) l-Ag NPs.

Next, we have analyzed these spectral changes in the form of Stern-Volmer plots in order to quantify the extent of quenching in the

presence of three different sized Ag NPs. Figure 4.5A shows the steady-state Stern-Volmer plots for the three different sized Ag NPs. All the plots are linear, suggesting a single kind of quenching mechanism. The estimated Stern-Volmer constants are  $2.3 \times 10^{10}$ ,  $3.1 \times 10^{10}$ , and  $4.5 \times 10^{10} \text{ M}^{-1}$  for s-, m-, and l-Ag NPs. Hence, these results clearly indicate that the quenching efficiency increases with the increase in the size of Ag NPs, having the maximum efficiency for the l-Ag NPs.

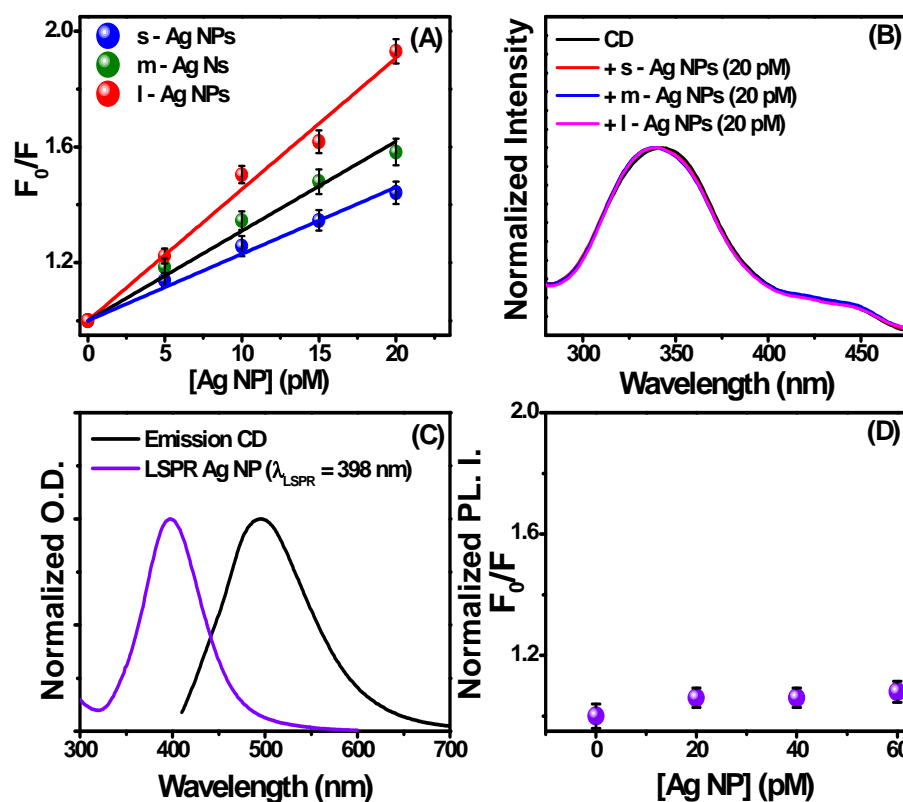


**Figure 4.5.** (A) Steady-state Stern-Volmer plots for CDs in the presence of s-, m- and l-Ag NPs. (B) Normalized excitation spectra of CD ( $\lambda_{em} = 495 \text{ nm}$ ) upon addition of 20 pM s, m, and l-Ag NPs. (C) Spectral overlap between the LSPR of Ag NP ( $\lambda_{\text{LSPR}} = 398 \text{ nm}$ ) and PL spectrum ( $\lambda_{ex} = 400 \text{ nm}$ ).

*nm) of CDs. (D) The steady-state Stern-Volmer plot for CDs in the presence of Ag NP having LSPR band at 398 nm.*

Previously, it has been reported that noble metal NPs act as efficient quenchers for various organics dyes and quantum dots [10, 22-25]. The observed PL quenching of CDs in the presence of three different sized Ag NPs could be due to various processes such as NP induced aggregation of CDs, electron transfer, and/or excitation energy transfer. As the estimated zeta potential of CDs and all the three different sized Ag NPs is highly negative, it is very unlikely that CDs will aggregate on the surface of Ag NPs. Moreover, the excitation spectrum ( $\lambda_{em} = 495$  nm) of CDs remains unaltered in the presence of different sized Ag NPs (Figure 4.5B). In addition, the PL peak position and full width at half maximum (FWHM) of the PL spectrum of CDs remain unaltered in the presence of different sized Ag NPs. These results clearly signify that the observed PL quenching of CDs in the presence of Ag NPs is not due to the aggregation of CDs at the surface of Ag NPs. CDs are well known for their electron donating and accepting properties [26]. In order to know the mechanism of quenching, we have performed a control experiment with citrate-capped Ag NPs having the LSPR band centered at 398 nm, which shows a minimal spectral overlap with the PL spectrum of CDs. Here, it is important to mention that if electron transfer is the mechanism for PL quenching of CDs, then we should expect a similar PL quenching of CDs in the presence of these Ag NPs ( $\lambda_{LSPR} = 398$  nm). However, if resonant excitation energy transfer is the mechanism behind the PL quenching of CDs, then the quenching efficiency should decrease significantly as a consequence of minimal spectral overlap. Figure 4.5C shows the minimal spectral overlap between the PL spectrum of CDs and LSPR of these Ag

NPs. Here it is important to note that the observed spectral overlap is only between the tails of LSPR of Ag NPs and the PL band of CDs. Interestingly, the PL intensity of CDs remains unaltered in the presence of these Ag NPs. Figure 4.5D displays the steady-state Stern-Volmer plot for CDs in the presence of Ag NPs ( $\lambda_{\text{LSPR}} = 398$  nm). The plot remains almost parallel to the x-axis signifying a lack of any PL quenching. These results clearly rule out the involvement of photo-induced electron transfer in the present system. To establish the mechanism behind this PL quenching of CDs, excited-state PL decay measurements have been performed.

### 4.2.3. Time-Resolved PL Measurements of CD in the Presence of Ag NPs

Figure 4.6 shows the PL decay traces of CD in the absence and presence of 20 pM s, m and l- Ag NPs at 495 nm emission wavelength. All the decays were fitted with a three exponential decay function. The average PL lifetime of CD is  $3.99 \pm 0.12$  ns with lifetime components of 0.44 (22%), 2.08 (35%), and 7.36 ns (43%), which is very close to the previously reported value [27]. The decay trace of CD changes significantly upon addition of different sized Ag NPs (Figure 4.6).

The average lifetime of CD decreases to  $3.12 \pm 0.08$ ,  $2.67 \pm 0.07$ , and  $1.80 \pm 0.05$  ns upon addition of 20 pM s, m, and l-Ag NPs, respectively (Table 4.1). These time-resolved results correlate well with our steady-state observation that the quenching efficiency increases with increase in the size of Ag NPs. All the fitted parameters are listed in table 4.1.

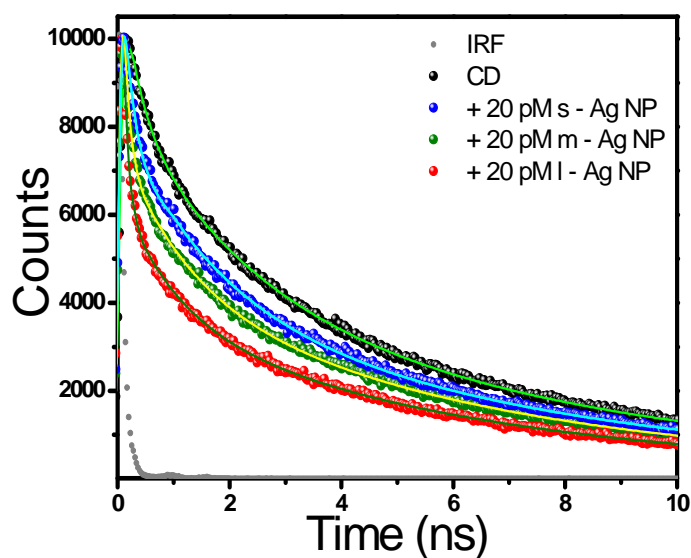


**Figure 4.6.** Changes in the PL decay traces ( $\lambda_{ex} = 405$  nm) of CD in the presence of *s*, *m*, and *l*-Ag NPs recorded at 495 nm emission wavelength.

**Table 4.1.** PL decay parameters of CD in the absence and presence of different sized Ag NPs.

System	$\tau_1$ (ns)	$a_1$	$\tau_2$ (ns)	$a_2$	$\tau_3$ (ns)	$a_3$	$\langle \tau \rangle$ (ns)	$\chi^2$
CD	0.44	0.22	2.08	0.35	7.36	0.43	3.99	1.14
+ <i>s</i> -Ag NP	0.26	0.41	2.36	0.31	8.10	0.28	3.12	1.20
+ <i>m</i> -Ag NP	0.19	0.46	1.88	0.26	7.33	0.28	2.67	1.18
+ <i>l</i> -Ag NP	0.12	0.61	1.50	0.18	6.89	0.21	1.80	1.21

The influence of LSPR of metal NPs on the intrinsic radiative and nonradiative decay rates of nearby fluorophores is well known in various

reports [9-12, 28-34]. The shortened lifetime of CD in the presence of Ag NPs suggests that either the radiative or nonradiative decay rate is increased. The radiative and nonradiative decay rates of CD in the presence of Ag NPs were estimated according to the following equations:

$$k_r = \frac{\phi_D}{\tau} \quad (2)$$

$$k_{nr} = \left( \frac{1 - \phi_D}{\tau} \right) \quad (3)$$

where  $k_r$  and  $k_{nr}$  are the radiative and nonradiative decay rates, respectively.  $\phi_D$  is the quantum yield and  $\tau$  is the average lifetime of the CD. All the estimated parameters are listed in Table 4.2. It is evident from Table 4.2 that the nonradiative decay rate of CD increases by a factor of 1.29, 1.50, and 2.25 in the presence of s, m, and l - Ag NPs, respectively. Importantly, no appreciable change has been observed in the radiative decay rate of CD upon addition of Ag NPs. This increase in nonradiative decay rate in the presence of Ag NPs can be explained by considering nonradiative EET from CD to Ag NP. The rate of this nonradiative EET is calculated from average lifetime of CD in the absence and presence of different sized Ag NPs by using the following equation:

$$k_{ET} = \frac{1}{\tau_{DA}} - \frac{1}{\tau_D} \quad (4)$$

where  $\tau_{DA}$  and  $\tau_D$  are the average PL lifetimes of CD in the presence and absence of Ag NPs, respectively. The estimated  $k_{ET}$  is  $0.07 \times 10^9$ ,  $0.12 \times 10^9$ , and  $0.30 \times 10^9 \text{ s}^{-1}$  for s, m, and l- Ag NPs, respectively (Table 4.2).

The efficiency ( $\phi_{\text{Eff}}$ ) of this nonradiative EET process is estimated using the following equations:

$$\phi_{\text{Eff}} = 1 - \frac{\phi_{\text{D-A}}}{\phi_{\text{D}}} = 1 - \frac{\tau_{\text{D-A}}}{\tau_{\text{D}}} \quad (5)$$

where  $\phi_{\text{D-A}}$  and  $\phi_{\text{D}}$  are the steady-state quantum yields of CD in the presence and absence of Ag NPs, respectively.  $\tau_{\text{D-A}}$  and  $\tau_{\text{D}}$  are the excited-state lifetimes of CD in the presence and absence of Ag NPs, respectively. The estimated EET efficiencies from the lifetime values are 22, 33, and 55% for s, m, and l-Ag NPs, respectively, which matches well with that estimated from steady-state measurements (Table 4.2). As expected from our steady-state PL quenching measurements, the efficiency of EET from CD to Ag NP increases with increase in the size of Ag NPs.

#### 4.2.4. Mechanism of EET from CD to Ag NPs

The observed resonant EET from CD to Ag NP could be due to either FRET or NSET process. These two most common resonant energy transfer theories have been extensively used to account EET for various donor-acceptor pairs. FRET is a nonradiative dipole-dipole through space interaction between two molecular dyes and is generally limited to distances up to 1-10 nm [13, 35, 36]. Hence, distances larger than 10 nm between center of donors and center of acceptors could not be accounted by FRET theory. The Förster distance  $R_0$  for CD-Ag NP system is estimated using the following equation:

$$R_0 = [(8.8 \times 10^{-25})(\kappa^2 \eta^{-4} \phi_{\text{D}} J(\lambda))]^{1/6} \quad (6)$$

where  $R_0$  is the distance from centre of donor to centre of acceptor at which the energy transfer efficiency is 50%,  $\kappa^2$  is the orientation factor of

the transition dipoles of the donor and the acceptor,  $\phi_D$  is the quantum yield of the donor,  $\eta$  is the refractive index of the medium, and  $J(\lambda)$  is the overlap integral between the donor emission and the acceptor absorption spectrum. The estimated Förster distance ( $R_0$ ) is 23.11, 28.02, and 32.13 nm for s, m, and l- Ag NPs, respectively which is well beyond the range of classical FRET theory. The theory of Persson and Lang, now referred to as NSET, has been highly successful in describing the recent experimental findings of fluorescence quenching near the metal NP surface [9, 11, 12, 14, 15, 19, 37]. Persson's NSET theory considers the collective interaction of all dipoles in a thin film near the surface of the metal, creating a  $1/d$  coupling [37]. Importantly, this empirical NSET theory has been experimentally verified by various groups for different donor-acceptor pairs [9, 11, 12, 14, 15, 19]. According to the NSET mechanism, the rate of EET can be expressed as

$$k_{\text{NSET}} = \frac{1}{\tau_D} \left( \frac{d_0}{d} \right)^4 \quad (7)$$

where  $\tau_D$  is the excited state lifetime of the donor in the absence of acceptor,  $d$  is the separation distance between the center of the donor and surface of the acceptor, and  $d_0$  is the separation distance at which the energy transfer is 50% efficient. The distance  $d_0$  can be calculated by using the following equation:

$$d_0 = \left( \frac{0.225 \phi_D c^3}{\omega_D^2 \omega_F k_F} \right)^{1/4} \quad (8)$$

where  $\phi_D$  is the quantum yield of the donor,  $c$  is the velocity of light,  $\omega_D$  is the angular frequency of the donor electronic transition,  $\omega_F$  is the Fermi frequency, and  $k_F$  is the Fermi wave vector of the metal. For the present

system, the  $d_0$  value is calculated using  $\phi_D = 0.053$ ,  $c = 3 \times 10^{10} \text{ cm s}^{-1}$ ,  $\omega_D = 3.8 \times 10^{15} \text{ s}^{-1}$ ,  $\omega_F = 8.3 \times 10^{15} \text{ s}^{-1}$ , and  $k_F = 1.2 \times 10^8 \text{ cm}^{-1}$  [18]. The calculated  $d_0$  for the CD-Ag NP system is 4.0 nm.

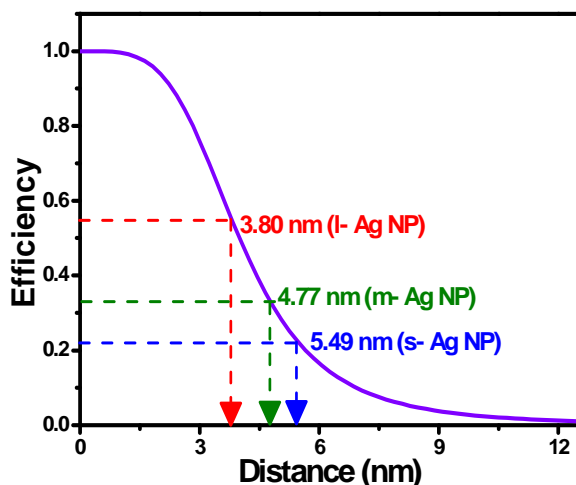


**Figure 4.7.** Theoretical curve of energy transfer efficiency against the distance between CD and Ag NP generated from NSET theory. Separation distances obtained from the experimentally determined energy transfer efficiencies are highlighted with blue, green and red arrows for s, m, and l- Ag NPs (20 pM) respectively.

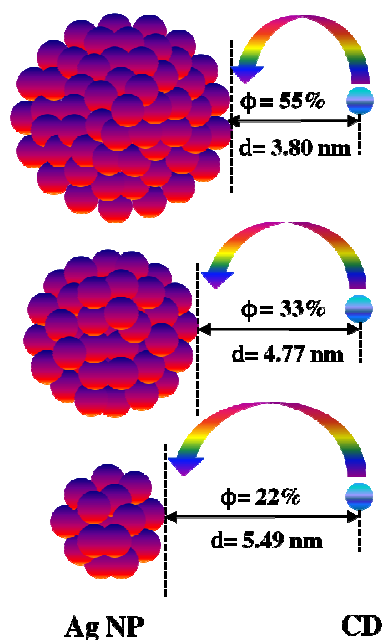
**Table 4.2.** Estimated quantum yields, radiative rates, nonradiative rates, energy transfer rates, efficiencies of energy transfer and estimated distance ( $d$ ) between CD and 20 pM Ag NPs.

System	$\phi_D$	$k_r$ ( $\times 10^9 \text{ s}^{-1}$ )	$k_{nr}$ ( $\times 10^9 \text{ s}^{-1}$ )	$k_{ET}$ ( $\times 10^9 \text{ s}^{-1}$ )	$\phi_{ET}$ ( $\tau$ )	$\phi_{ET}$ ( $\phi_D$ )	$d$ (nm)
CD	0.053	0.013	0.24	-	-	-	-
+ s-Ag NP	0.037	0.012	0.31	0.07	0.22	0.31	5.49
+ m-Ag NP	0.033	0.012	0.36	0.12	0.33	0.38	4.77
+ l-Ag NP	0.028	0.015	0.54	0.30	0.55	0.48	3.80

On the basis of this calculated value of  $d_0$ , quenching efficiencies are estimated as a function of distance according to the following equation:

$$\phi_{\text{ET}} = \frac{1}{1 + \left(\frac{d}{d_0}\right)^4} \quad (9)$$

where  $\phi_{\text{ET}}$  is the energy transfer efficiency and  $d$  is the separation distance between CD and Ag NP. Figure 4.7 shows the theoretical plot of the quenching efficiency against the separation distance based on NSET theory. By using the values of experimentally obtained quenching efficiencies, we have estimated the separation distance between CD and the surface of Ag NP which has a value of 5.49, 4.77, and 3.80 nm for s, m, and l- Ag NPs, respectively (Table 4.2, Scheme 4.1). Here it is important to compare the estimated average distance between CD and different sized Ag NPs and the corresponding NSET efficiencies. Notably, with the increase in the size of Ag NPs from s to l- Ag NPs the corresponding zeta potential decreases gradually from -76.24 to -58.01 mV. As a consequence of this reduced negative surface charge of larger sized Ag NPs, the effective electrostatic repulsion between CD and Ag NPs decreases and results in the shorter distance between CD and larger sized Ag NP. As a result of this reduced distance between CD and larger sized Ag NPs, the NSET efficiency increases (Scheme 4.1).



**Scheme 4.1.** Schematic representation of EET from CD to different sized Ag NPs.

### 4.3. Conclusions

The present results shine a light on the resonant NSET process between CD and different sized Ag NPs. The steady-state and time-resolved lifetime measurements reveal that the observed PL quenching of CD in the presence of Ag NPs arises due to the increased nonradiative decay rate while the radiative decay rate remains constant. This enhancement in the nonradiative decay rate of CD in the presence of Ag NPs arises mainly due to the EET from CD to Ag NPs. This nonradiative EET from CD to Ag NP has been explained by considering NSET theory. Moreover, it has been observed that the efficiency of this EET increases with increase in the size of Ag NPs. This phenomenon has been explained by considering the extent of spectral overlap and distance between CD and

different sized Ag NPs. It has been observed that with increase in the size of Ag NPs the spectral overlap increases. More importantly, the zeta potential of Ag NPs decreases with increase in the size and as a consequence the effective distance between CD and Ag NPs decreases due to reduced electrostatic repulsion. As the effective distance between CD and Ag NPs decreases, the NSET efficiency increases. Finally, our present study revealed that the efficiency of NSET process can be easily tuned as a function of NP size.

### 4.4. References

1. Stewart M. E., Anderton C. R., Thompson L. B., Maria J., Gray S. K., Rogers J. A., Nuzzo R. G. (2008), Nanostructured plasmonic sensors, *Chem. Rev.*, 108, 494-521. (DOI: 10.1021/cr068126n)
2. Ozbay E. (2006), Plasmonics: Merging photonics and electronics at nanoscale dimensions, *Science*, 311, 189-193. (DOI: 10.1126/science.1114849)
3. Polman A. (2008), Plasmonics applied, *Science*, 2008, 322, 868-869. (DOI: 10.1126/science.1163959)
4. Duyne R. P. V. (2004), Molecular plasmonics, *Science*, 306, 985-986. (DOI: 10.1126/science.1104976)
5. Naiki H., Masuhara A., Masuo S., Onodera T., Kasai H., Oikawa H. (2013), Highly controlled plasmonic emission enhancement from metal-semiconductor quantum dot complex nanostructures, *J. Phys. Chem. C*, 117, 2455-2459. (DOI: 10.1021/jp305408p)
6. Li C., Zhu Y., Zhang X., Yang X., Li C. (2012), Metal-enhanced fluorescence of carbon dots adsorbed Ag@SiO<sub>2</sub> core-shell nanoparticles, *RSC Adv.*, 2, 1765-1768. (DOI: 10.1039/C2RA01032A)
7. Liu Y., Wu P. (2013), Meditating metal coenhanced fluorescence and SERS around gold nanoaggregates in nanosphere as bifunctional biosensor for multiple DNA targets, *ACS Appl. Mater. Interfaces*, 5, 5832-5844. (DOI: 10.1021/am401468a)
8. Som T., Karmakar B. (2009), Nanosilver enhanced upconversion fluorescence of erbium ions in Er<sup>3+</sup>: Ag-antimony

glass nanocomposites, *J. Appl. Phys.*, 105, 013102. (DOI: 10.1063/1.3054918)

9. Yun C. S., Javier A., Jennings T., Fisher M., Hira S., Peterson S., Hopkins B., Reich N. O., Strouse G. F. (2005), Nanometal surface energy transfer in optical rulers, breaking the FRET barrier, *J. Am. Chem. Soc.*, 127, 3115-3119. (DOI: 10.1021/ja043940i)

10. Dulkeith E., Ringler M., Klar T. A., Feldmann J., Javier A. M., Parak W. J. (2005), Gold nanoparticles quench fluorescence by phase induced radiative rate suppression, *Nano Lett.*, 5, 585-589. (DOI: 10.1021/nl0480969)

11. Jennings T. L., Singh M. P., Strouse G. F. (2006), Fluorescent lifetime quenching near  $d = 1.5$  nm gold nanoparticles: Probing NSET validity, *J. Am. Chem. Soc.*, 128, 5462-5467. (DOI: 10.1021/ja0583665)

12. Sen T., Sadhu S., Patra A., Surface energy transfer from rhodamine 6G to gold nanoparticles: A spectroscopic ruler, *App. Phys. Lett.*, 91, 043104. (DOI: 10.1063/1.2762283)

13. Sapsford K. E., Berti L., Medintz I. L. (2006), Materials for fluorescence resonance energy transfer analysis: Beyond traditional donor-acceptor combinations, *Angew. Chem. Int. Ed.*, 45, 4562-4588. (DOI: 10.1002/anie.200503873)

14. Pons T., Medintz I. L., Sapsford K. E., Higashiya S., Grimes A. F., English D. S., Mattoussi H. (2007), On the quenching of semiconductor quantum dot photoluminescence by proximal gold nanoparticles, *Nano Lett.*, 7, 3157-3164. (DOI: 10.1021/nl071729+)

15. Breshike C. J., Riskowski R. A., Strouse G. F. (2013), Leaving Förster resonance energy transfer behind: Nanometal surface energy transfer predicts the size-enhanced energy coupling between a metal nanoparticle and an emitting dipole, *J. Phys. Chem. C*, 117, 23942-23949. (DOI: 10.1021/jp407259r)
16. Prajapati R., Chatterjee S., Bhattacharya A., Mukherjee T. K. (2015), Surfactant-induced modulation of nanometal surface energy transfer from silicon quantum dots to silver nanoparticles, *J. Phys. Chem. C*, 119, 13325-13334. (DOI: 10.1021/acs.jpcc.5b02903)
17. Li M., Cushing S. K., Wang Q., Shi X., Hornak L. A., Hong Z., Wu N. (2011), Size-dependent energy transfer between CdSe/ZnS quantum dots and gold nanoparticles, *J. Phys. Chem. Lett.*, 2, 2125-2129. (DOI: 10.1021/jz201002g)
18. Saraswat S., Desireddy A., Zheng D., Guo L., Lu H. P., Bigioni T. P., Isailovic D. (2011), Energy transfer from fluorescent proteins to metal nanoparticles, *J. Phys. Chem. C*, 115, 17587-17593. (DOI: 10.1021/jp2029246)
19. Singh M. P., Strouse G. F. (2010), Involvement of the LSPR spectral overlap for energy transfer between a dye and Au nanoparticle, *J. Am. Chem. Soc.*, 132, 9383-9391. (DOI: 10.1021/ja1022128)
20. Zhu S., Meng Q., Wang L., Zhang J., Song Y., Jin H., Zhang K., Sun H., Wang H., Yang B. (2013), Highly photoluminescent carbon dots for multicolor patterning, sensors, and bioimaging, *Angew. Chem. Int. Ed.*, 52, 3953-3957. (DOI: 10.1002/anie.201300519)

21. Yu P., Wen X., Toh Y. R., Tang J. (2012), Temperature-dependent fluorescence in carbon dots, *J. Phys. Chem. C*, 116, 25552-25557. (DOI: 10.1021/jp307308z)
22. Kuhnke K., Becker R., Epple M., Kern K. (1997), C<sub>60</sub> Exciton quenching near metal surfaces, *Phys. Rev. Lett.*, 79, 3246-3249. (DOI: 10.1103/PhysRevLett.79.3246)
23. Dulkeith E., Morteani A. C., Niedereichholz T., Klar T. A., Feldmann J., Moller M., Gittins D. I. (2002), Fluorescence quenching of dye molecules near gold nanoparticles: radiative and nonradiative effects. *Phys. Rev. Lett.*, 89, 203002. (DOI: 10.1103/PhysRevLett.89.203002)
24. Cannone F., Chirico G., Bizzarri A. R., Cannistraro S. (2006), Quenching and blinking of fluorescence of a single dye molecule bound to gold nanoparticles, *J. Phys. Chem. B*, 110, 16491-16498. (DOI: 10.1021/jp0625816)
25. Kim K. S., Kim J. H., Kim H., Laquai F., Arifin E., Lee J. K., Yoo S., Sohn B. H. (2012), Switching off FRET in the hybrid assemblies of diblock copolymer micelles, quantum dots, and dyes by plasmonic nanoparticles, *ACS Nano*, 6, 5051-5059. (DOI: 10.1021/nn301893e)
26. Mondal S., Das T., Maity A., Seth S. K., Purkayastha P. (2015), Synergic influence of reverse micelle confinement on the enhancement in photoinduced electron transfer to and from carbon nanoparticles, *J. Phys. Chem. C*, 119, 13887-13892. (DOI: 10.1021/acs.jpcc.5b02026)

27. Bhattacharya A., Chatterjee S., Khorwal V., Mukherjee T. K. (2016), Luminescence turn-on/off sensing of biological iron by carbon dots in transferring, *Phys. Chem. Chem. Phys.*, 18, 5148-5158. (DOI: 10.1039/C5CP05890B)
28. Shimizu K. T., Woo W. K., Fisher B. R., Eisler H. J., Bawendi M. G. (2002), Surface-enhanced emission from single semiconductor nanocrystals, *Phys. Rev. Lett.*, 89, 117401. (DOI: 10.1103/PhysRevLett.89.117401)
29. Kühn S., Håkanson U., Rogobete L., Sandoghdar V. (2006), Enhancement of single-molecule fluorescence using a gold nanoparticle as an optical nanoantenna, *Phys. Rev. Lett.*, 97, 017402. (DOI: 10.1103/PhysRevLett.97.017402)
30. Chen Y., Munechika K., Ginger D. S. (2007), Dependence of fluorescence intensity on the spectral overlap between fluorophores and plasmon resonant single silver nanoparticles, *Nano Lett.*, 7, 690-696. (DOI: 10.1021/nl062795z)
31. Munechika K., Chen Y., Tillack A. F., Kulkarni A. P., Plante I. J. L., Munro A. M., Ginger, D. S. (2010), Spectral control of plasmonic emission enhancement from quantum dots near single silver nanoprisms, *Nano Lett.*, 10, 2598-2603. (DOI: 10.1021/nl101281a)
32. Pan S. L., Wang Z. J., Rothberg L. J. (2006), Enhancement of adsorbed dye monolayer fluorescence by a silver nanoparticle overlayer, *J. Phys. Chem. B*, 110, 17383-17387.

33. Xie F., Baker M. S., Goldys E. M. (2006), Homogeneous silver-coated nanoparticle substrates for enhanced fluorescence detection, *J. Phys. Chem. B*, 110, 23085-23091. (DOI: 10.1021/jp062170p)
34. Thomas K. G., Kamat P. V. (2000), Making gold nanoparticles glow: Enhanced emission from a surface-bound fluorophore, *J. Am. Chem. Soc.*, 122, 2655-2656. (DOI: 10.1021/ja9941835)
35. Ghosh D., Chattopadhyay N. (2013), Gold nanoparticles: Acceptors for efficient energy transfer from the photoexcited fluorophores, *Opt. Photon. J.*, 3, 18-26. (DOI: 10.4236/opj.2013.31004 P)
36. Watrob H. M., Pan C. P., Barkley M. D. (2003), Two-step FRET as a structural tool, *J. Am. Chem. Soc.*, 125, 7336-7343. (DOI: 10.1021/ja034564p)
37. Persson B. N. J., Lang N. D. (1982), Electron-hole-pair quenching of excited states near a metal, *Phys. Rev. B*, 26, 5409-5415. (DOI: 10.1103/PhysRevB.26.5409)



**Chapter 5**

*Effect of Compartmentalization of  
Donor and Acceptor on the Ultrafast  
Resonance Energy Transfer from  
DAPI to Silver Nanoclusters*

### 5.1. Introduction

Nonradiative excitation energy transfer (EET) from a photo-excited donor to an acceptor via distance-dependent dipole-dipole interactions is well known as Förster resonance energy transfer (FRET). FRET is particularly important for measuring the dynamic changes in the distance between molecular donor and acceptor covalently attached to biological macromolecules and finds enormous application in single molecule biophysics [1, 2].

Over the last few years, semiconductor quantum dots and metal nanoparticle (NP) based donor-acceptor composite systems have gained considerable attention due to their size-dependent optoelectronic properties which allow easy tuning of energy transfer efficiency [3-8]. It has been observed that metal NP with distinct localized surface plasmon resonance (LSPR) often quenches the molecular excitation energy of nearby fluorophore due to modulation of either radiative or nonradiative decay rate or both [9-18]. Although the mechanism and dynamics of EET process are extensively studied in the presence of various metal NPs having distinct LSPR in the visible region of the electromagnetic spectrum, very less is known about the mechanism and dynamics of fluorescence quenching near the ultrasmall metal nanocluster (NC) surface, which lacks characteristic LSPR.

Recently, there is a growing interest to explore these metal NCs for a wide range of applications such as nanophotonics, catalysis, biolabeling, and sensing, because of their small size, and unique optoelectronic properties [19-27]. Due to the strong quantum confinement, the energy bands split into discrete energy levels and as a result metal NCs do not show any LSPR, instead, they exhibit multiple narrow molecular-like

electronic transitions with strong luminescence. Earlier, it has been demonstrated that Au NC with no LSPR signal can also act as an efficient acceptor of molecular excitation energy in many composite systems [14, 15, 28]. Similarly, Muhammed et al. (2008) have demonstrated the nonradiative FRET process between dansyl chromophore and ultrasmall glutathione-capped Au<sub>25</sub> NC (Au<sub>25</sub>SG<sub>18</sub>) through steady-state and femtosecond time-resolved fluorescence techniques [29]. Recently, Bain et al. (2015) have illustrated the role of surface capping ligands of Au<sub>25</sub> NCs on the FRET process in metal NC-semiconductor composites [30]. While most of these earlier studies on EET were performed with Au NCs, similar thorough investigations with Ag NCs are rare.

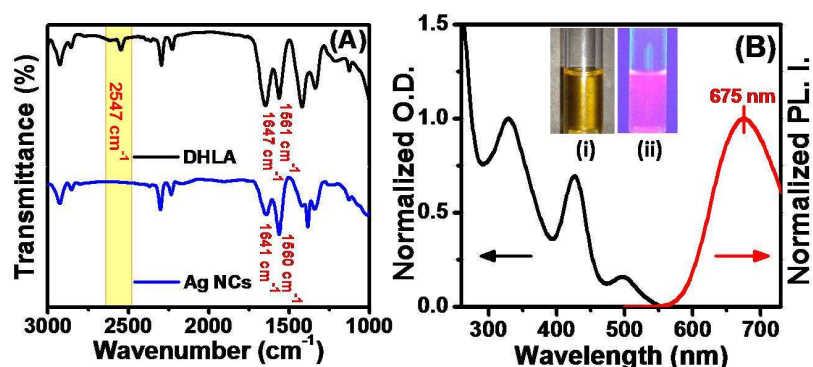
In the present work, the fundamental mechanism and dynamics behind the fluorescence quenching of DAPI by dihydrolipoic acid (DHLA)-capped Ag NCs and its subsequent suppression in the presence of cationic water-soluble polymer poly(diallyldimethylammoniumchloride) (PDADMAC) and CT-DNA have been demonstrated. The results reveal that the fluorescence quenching of DAPI near the ultrasmall Ag NCs occurs via efficient ultrafast nonradiative FRET process. Moreover, it has been illustrated that the selective compartmentalization of either donor (DAPI) or acceptor (Ag NC) leads to complete suppression of this FRET process.

## 5.2. Results and Discussions

### 5.2.1. Characterization of Ag NCs

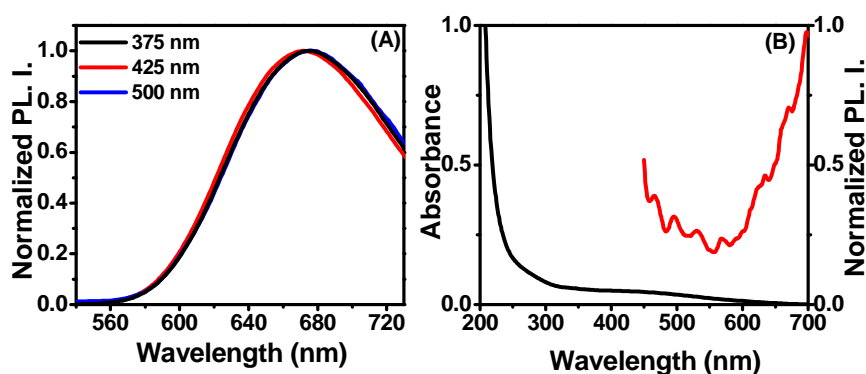
The as-synthesized DHLA-capped Ag NCs were characterized by FTIR, HRTEM, UV-Vis spectroscopy, PL spectroscopy, and mass spectrometry. Figure 5.1A shows the FTIR spectrum of DHLA-capped Ag

NCs with that of DHLA ligand only. The characteristic stretching frequency of S-H bond at  $2547\text{ cm}^{-1}$  observed for DHLA ligand disappears upon conjugation with Ag NCs, indicating the attachment of DHLA to the Ag NC surface through its free thiol end. Other noticeable peaks at  $1560\text{ cm}^{-1}$  and  $1420\text{ cm}^{-1}$  can be assigned to the stretching of the carboxylate groups. Hence, the absence of any thiol peak and the presence of carboxylate peaks in the FTIR spectrum of DHLA-capped Ag NCs confirm the formation of the DHLA-Ag NCs nanoconjugate. This kind of bonding interactions between DHLA and Ag NCs is expected as DHLA remains in thiol carboxylate form at pH 7.4. Therefore, at pH 7.4 the thiol carboxylate is the predominant species. Figure 5.1B shows the absorption and PL spectra of as-synthesized DHLA-capped Ag NCs in pH 7.4 phosphate buffer. The absorption spectrum of the Ag NCs consists of two narrow peaks at 329 and 426 nm with a weak shoulder at 497 nm, which matches well with the earlier reported absorption spectrum of DHLA-capped Ag NCs [31]. The PL spectrum of these Ag NCs consists of a distinct PL band centered at 675 nm ( $\lambda_{\text{ex}}=375\text{ nm}$ ), which is close to the other reported DHLA-capped Ag NCs [31, 32]. The inset of Figure 5.1B shows the photographs of Ag NCs dispersed in aqueous buffer under daylight (i) and UV light exposure (ii).



**Figure 5.1.** (A) FTIR spectra of dihydrolipoic acid and synthesized Ag NCs. (B) The normalized absorption (black line) and PL (red line) spectra of 5  $\mu\text{M}$  Ag NCs. Photographs of Ag NCs in pH 7.4 buffer under (i) daylight and (ii) UV light.

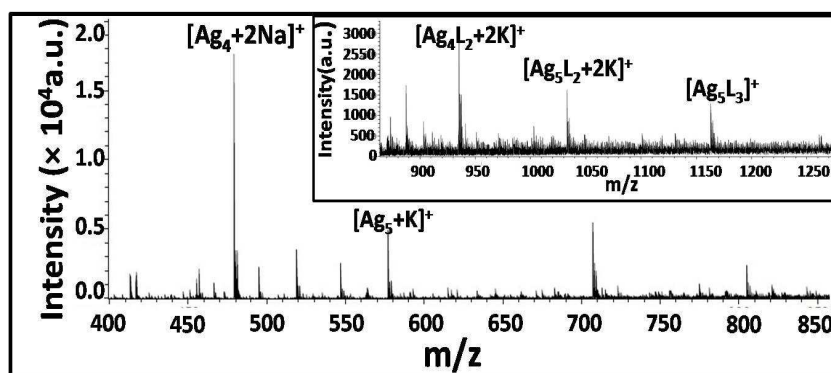
Notably, the PL peak position and spectral shape do not change with excitation wavelength indicating the narrow and homogeneous size distribution of these Ag NCs (Figure 5.2A). Here it should be noted that simple Ag(I)-DHLA complex prepared by mixing Ag(I) salt with DHLA ligand does not exhibit any characteristic absorption and luminescence bands, signifying that our synthesized DHLA-capped Ag NCs are chemically and structurally quite different from that of simple Ag(I)-S-Ag(I) kind of complex (Figure 5.2B).



**Figure 5.2.** (A) Normalized PL spectra of Ag NCs at different excitation

wavelengths. (B) Absorption and normalized PL spectrum ( $\lambda_{ex}= 375\text{ nm}$ ) of Ag(I)-DHHLA complex.

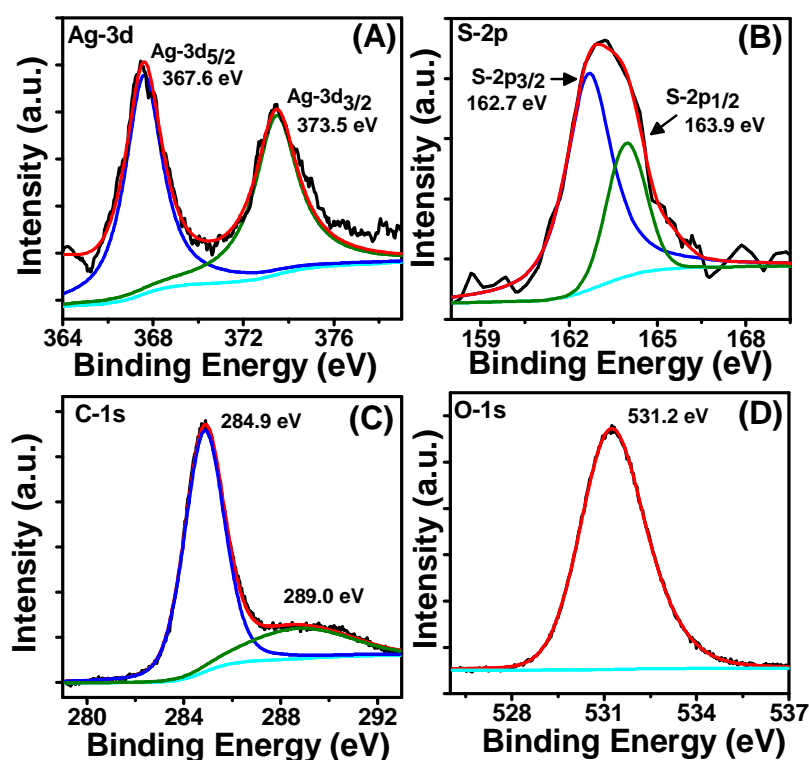
The exact molecular mass and composition of the as-synthesized Ag NC core have been confirmed by the mass spectrometric analysis. Figure 5.3 shows the mass spectrum of DHHLA-capped Ag NCs in 1:1 water-methanol mixture. The spectrum reveals a major peak at  $m/z$  477.80, which can be assigned to  $[\text{Ag}_4+2\text{Na}]^+$  cluster. A minor peak observed at  $m/z$  578.03 corresponds to  $[\text{Ag}_5+\text{K}]^+$  cluster. Other noticeable peaks at higher  $m/z$  values correspond to ligand associated  $\text{Ag}_4$  and  $\text{Ag}_5$  clusters (Figure 5.3, inset). These peaks are in good agreement with the earlier reported high-resolution mass spectroscopy spectrum of DHHLA-capped Ag NCs [31]. Hence, these results reveal that our as-synthesized Ag NCs contain the majority of  $\text{Ag}_4$  core with a minor amount of  $\text{Ag}_5$  core.



**Figure 5.3.** Electrospray ionization mass spectrum of as-synthesized DHHLA-capped Ag NCs in 1:1 water-methanol mixture ( $L$  represents DHHLA ligand). The inset shows the mass spectrum beyond 850  $m/z$ .

To know the chemical nature and composition of these DHHLA-capped Ag NCs, X-ray photoelectron spectroscopy (XPS) measurements

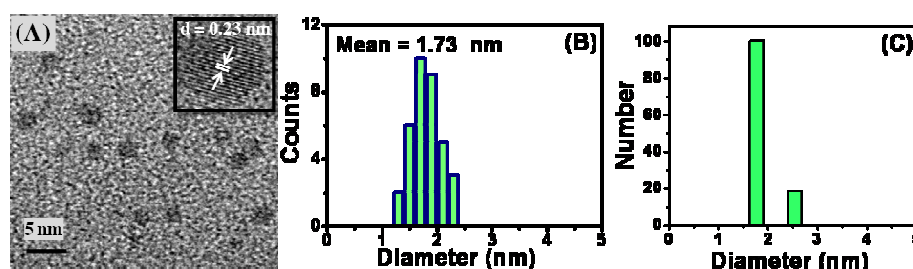
were performed. Figure 5.4 displays the expanded XPS spectra of Ag 3d, S 2p, C 1s, and O 1s. Two binding energy peaks at 367.7 and 373.5 eV have been observed for Ag 3d<sub>5/2</sub> and Ag 3d<sub>3/2</sub>, respectively. The Ag 3d<sub>5/2</sub> peak is located between the Ag(0) peak and Ag(I) peak and indicates the formation of Ag NCs with Ag(I)-thiolate bonding at the surface [33, 34]. The S 2p<sub>3/2</sub> and S 2p<sub>1/2</sub> peaks are observed at 162.7 and 163.9 eV, which indicate the presence of thiolate-Ag bonding in DHLA-capped Ag NC (Figure 5.4B). The C 1s spectrum shows two peaks at 284.9 and 289.0 eV due to the carbon atoms of aliphatic (C-C) and carboxylic acid (-COOH) groups, respectively (Figure 5.4C). Figure 5.4D shows the expected O 1s spectrum of DHLA-capped Ag NC.



**Figure 5.4.** Expanded XPS spectra of the elements (A) Ag 3d, (B) S 2p, (C) C 1s, and (D) O 1s of DHLA-capped Ag NC.

## Chapter 5

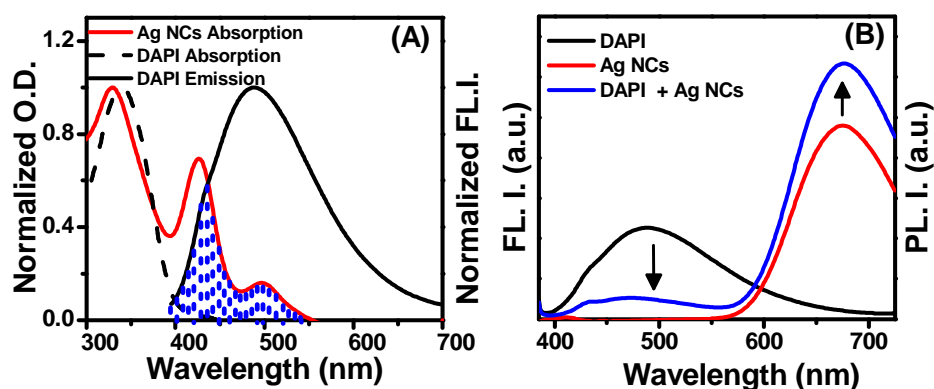
Next, HRTEM measurements were performed to explore the morphology and mean size of these Ag NCs (Figure 5.5). The image reveals spherical particles with an average diameter of  $1.73 \pm 0.28$  nm. The inset shows the presence of lattice planes with an interfringe distance of 0.23 nm, which corresponds to the (111) plane of the *fcc* Ag [31, 32]. However, Ag NCs with Ag<sub>2</sub>-Ag<sub>9</sub> core should exhibit size well below 1 nm [35, 36]. Here, it is important to mention that although TEM has been used earlier to measure the sizes of various Ag NCs, it has often been observed that the high energy electron beam irradiation leads to aggregation of these NCs [35, 36]. Hence, the large mean diameter ( $1.73 \pm 0.28$  nm) estimated from TEM measurements might be due to the aggregation of DHLA-capped Ag NCs upon high energy (200 kV) electron beam irradiation. In order to know the mean hydrodynamic diameter of these DHLA-capped Ag NCs DLS measurements were performed. DLS histogram reveals the presence of monodispersed Ag NCs with a mean hydrodynamic diameter of 1.8 nm (Figure 5.5C).



**Figure 5.5.** (A) HRTEM image of Ag NCs. The inset shows the presence of lattice planes with an interfringe distance of 0.23 nm. Size distribution histogram of Ag NCs estimated from (B) TEM and (C) DLS measurements.

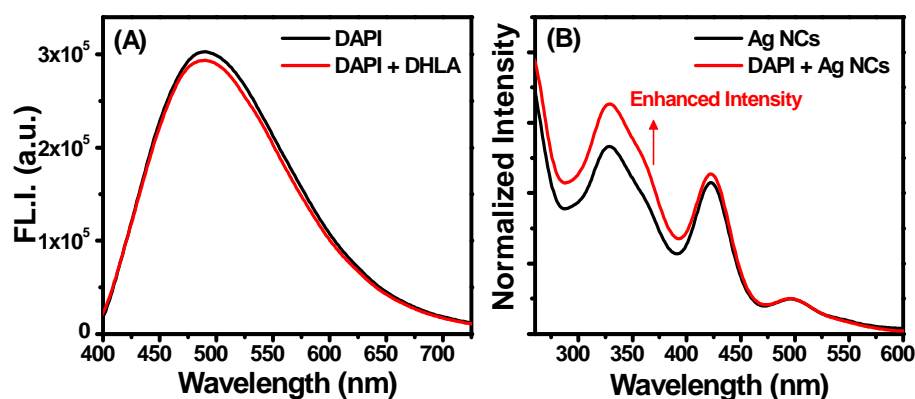
## 5.2.2. Excitation Energy Transfer from DAPI to Ag NCs

Figure 5.6A shows the normalized absorption and emission spectra of DAPI with the absorption spectrum of Ag NCs. DAPI in pH 7.4 phosphate buffer shows an absorption peak at 340 nm and emission maximum at 492 nm upon excitation at 375 nm (Figure 5.6A). It is evident from Figure 5.6A that the broad emission spectrum of DAPI overlaps significantly with the absorption spectrum of Ag NCs. Figure 5.6B shows the changes in the individual emission spectrum of DAPI and Ag NCs upon formation of DAPI-Ag NC composite. The emission spectrum of the composite system exhibits significant fluorescence quenching of DAPI at 492 nm with concomitant PL enhancement of Ag NCs at 675 nm compared to individual components.



**Figure 5.6.** (A) The normalized absorption spectrum (black dashed line) and fluorescence ( $\lambda_{ex} = 375$  nm) spectrum (black line) of 2.5  $\mu$ M DAPI and the normalized absorption spectrum of Ag NCs (red line). The blue dotted region shows the overlap between the absorption spectrum of Ag NCs and fluorescence of DAPI. (B) Changes in the fluorescence spectra ( $\lambda_{ex} = 375$  nm) of DAPI (black line) and Ag NCs (red line) upon formation of DAPI–Ag NCs composite (blue line).

A control experiment with only DHLA ligand shows no significant changes in the fluorescence quantum yield of DAPI, which indicates that the Ag NC itself quenches the fluorescence of nearby DAPI instead of the surface ligands (Figure 5.7A). The existence of significant spectral overlap between the fluorescence spectrum of DAPI and absorption spectrum of Ag NCs signifies that the observed fluorescence quenching of DAPI with a concomitant increase in PL intensity of Ag NCs might be due to FRET from photo-excited DAPI to Ag NCs. Similar kinds of fluorescence quenching of various fluorophores near the Au NC have been reported recently [29, 30]. Moreover, the normalized excitation spectra of Ag NCs in the absence and presence of DAPI recorded at 675 nm (with 399 nm filter) show enhanced intensity in the wavelength range 300-400 nm, which unequivocally prove the FRET process from DAPI to Ag NCs (Figure 5.7B).



**Figure 5.7.** (A) Changes in the fluorescence spectra of DAPI (black line) on the addition of DHLA (red line). (B) Normalized (at 500 nm) excitation spectra of Ag NCs ( $\lambda_{em} = 675$  nm) in the absence (black line) and presence (red line) of DAPI recorded with 399 nm filter.

Next, the fraction,  $f$ , of the DAPI emission that is quenched due to DAPI-Ag NC FRET process was calculated according to the following equation [37]:

$$f = \frac{\Delta I_{\text{FRET}}^{\text{A}}}{\Delta I_{\text{quench}}^{\text{D}}} \cdot \frac{\phi_{\text{F}}^{\text{D}}}{\phi_{\text{F}}^{\text{A}}} \quad (1)$$

where  $\Delta I_{\text{FRET}}^{\text{A}}$  is the enhanced acceptor fluorescence,  $\Delta I_{\text{quench}}^{\text{D}}$  is the difference in the donor emission intensities in the absence and presence of acceptor, and  $\phi_{\text{F}}^{\text{D}}$  and  $\phi_{\text{F}}^{\text{A}}$  are the emission quantum yields of the only donor (0.021) and acceptor (0.02), respectively. The  $f$  value i.e. the fraction of quenching of DAPI emission due to FRET from DAPI to Ag NCs is estimated around 92%. This indicates that the majority of the observed fluorescence quenching is due to FRET process between DAPI and Ag NCs.

In order to further explore the dynamics of this fluorescence quenching, femtosecond fluorescence upconversion measurements have been performed. Figure 5.8A shows the excited-state decay traces ( $\lambda_{\text{ex}}=375$  nm) of DAPI in the absence and presence of Ag NCs recorded at 490 nm emission wavelength. DAPI in pH 7.4 phosphate buffer shows an average fluorescence lifetime of 81.50 ps with lifetime components of  $2.35 \pm 0.18$  ps (31%) and  $117.90 \pm 1.96$  ps (69%) (Table 5.1). Similar bi-exponential excited-state decay with a very short average lifetime of DAPI in aqueous solution is reported earlier [38, 39]. It has been proposed that DAPI in aqueous solution remains in two conformational structures (planar and twisted conformations) and exhibits fast non-radiative relaxation via excited-state proton transfer reaction [38, 39]. Significant shortening of fluorescence lifetime of DAPI has been observed in the presence of Ag NCs (Figure 5.8A). The average fluorescence lifetime of DAPI decreases from 81.50 to 3.71 ps in the presence of Ag NCs (Table

5.1). DAPI in the presence of Ag NCs exhibits a biexponential decay with lifetime components of  $0.67 \pm 0.02$  ps (87%) and  $24.80 \pm 2.15$  ps (13%). Here it is important to mention that the reported luminescence lifetime of DHLA-capped Ag NCs is in microsecond ( $\mu$ s) range and do not interfere with the decay traces of DAPI in the femtosecond time scale [31]. This shortened excited-state lifetime of DAPI in the presence of Ag NCs strongly signifies the involvement of nonradiative FRET from DAPI to Ag NCs.

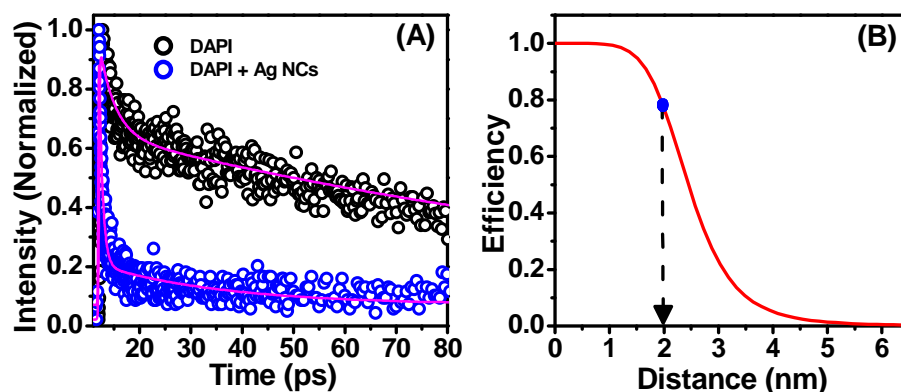


**Figure 5.8.** (A) Femtosecond fluorescence transients ( $\lambda_{ex} = 375$  nm) of DAPI in the absence (black) and presence of Ag NCs (blue) recorded at 490 nm emission wavelength. (B) Theoretical curves of energy transfer efficiency against the distance between DAPI and Ag NCs generated from FRET theory. Experimentally obtained energy transfer efficiency from steady-state data is highlighted with a blue color circle.

The efficiency ( $\phi_{\text{Eff}}$ ) of this nonradiative FRET process was calculated using the following equation:

$$\phi_{\text{Eff}} = 1 - \frac{\phi_{\text{D-A}}}{\phi_{\text{D}}} \quad (2)$$

where  $\phi_{D-A}$  and  $\phi_D$  are the quantum yield of DAPI in the presence and absence of Ag NCs, respectively. The estimated EET efficiency of the present system is 77.7%. The calculated rate for this nonradiative EET is  $0.26 \times 10^{12} \text{ s}^{-1}$  (Table 5.2).

Next, various energy transfer parameters for the present DAPI-Ag NC system were estimated. The Förster distance  $R_0$  for the present DAPI-Ag NC system can be estimated by using the following equation:

$$R_0 = [(8.8 \times 10^{-25})(\kappa^2 \eta^{-4} \phi_D J(\lambda))]^{1/6} \quad (3)$$

where  $\kappa^2$  is the orientation factor of the transition dipoles of the donor and the acceptor,  $\phi_D$  is the quantum yield of the donor,  $\eta$  is the refractive index of the medium, and  $J(\lambda)$  is the spectral overlap integral between the donor emission and the acceptor absorption spectrum. For the present DAPI-Ag NCs system, the calculated overlap integral is  $5.51 \times 10^{-14} \text{ M}^{-1} \text{ cm}^3$  and the estimated  $R_0$  is 2.45 nm (Table 5.2). Notably, for an ideal FRET pair, the typical Förster distance lies in the range of 2.0-6.0 nm [40]. Moreover, the estimated small  $R_0$  value for the present D-A system signifies that the present FRET pair can be used to probe the short-range distance fluctuations in various FRET- based applications.

On the basis of the estimated value of  $R_0$ , the theoretical quenching efficiency as a function of distance between DAPI and Ag NC was plotted according to the following equation:

$$\phi_{ET} = \frac{1}{1 + \left(\frac{R}{R_0}\right)^6} \quad (4)$$

where  $\phi_{ET}$  is the energy transfer efficiency and  $R$  is the separation distance between DAPI and Ag NC. Figure 5.8B shows the theoretical plots of the quenching efficiency against the separation distance based on the FRET theory for the present system. Experimentally obtained quenching efficiency for the present system is shown with the blue circle on the

## Chapter 5

curves. The estimated average separation distances between DAPI and Ag NC is 2.0 nm. Moreover, favorable electrostatic interactions between positively charged DAPI and negatively charged DHLA ligands on the surface of Ag NCs accounts for the very short distance (2.0 nm) between DAPI and Ag NCs (Scheme 5.1).

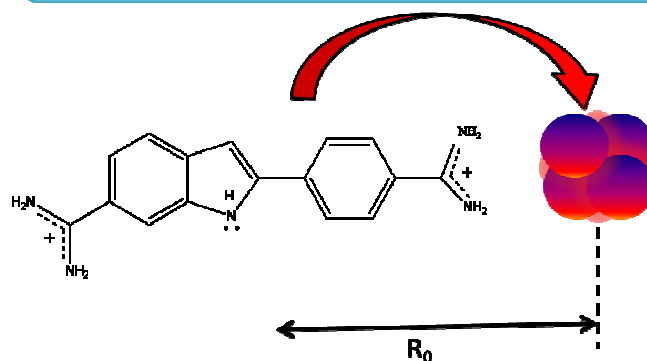
**Table 5.1.** Fluorescence decay parameters of DAPI in the absence and presence of Ag NCs.

System	$\tau_1$ (ps)	$a_1$	$\tau_2$ (ps)	$a_2$	$\langle\tau\rangle$ (ps)
DAPI	$2.35 \pm 0.18$	0.31	$117.90 \pm 1.96$	0.69	81.50
+ Ag NCs	$0.67 \pm 0.02$	0.87	$24.80 \pm 2.15$	0.13	3.71

**Table 5.2.** Estimated quantum yields, overlap integral ( $J$ ), rate of energy transfer ( $k_{ET}$ ), and  $R_0$  for DAPI-Ag NCs system.

System	$\phi_D$	$J(\lambda)$ ( $M^{-1} cm^3$ )	$k_{ET}$ ( $\times 10^{12} s^{-1}$ )	$R_0$ (nm)
DAPI	0.021	–	–	–
+ Ag NCs	0.0046	$5.51 \times 10^{-14}$	0.26	2.45

## Förster resonance energy transfer

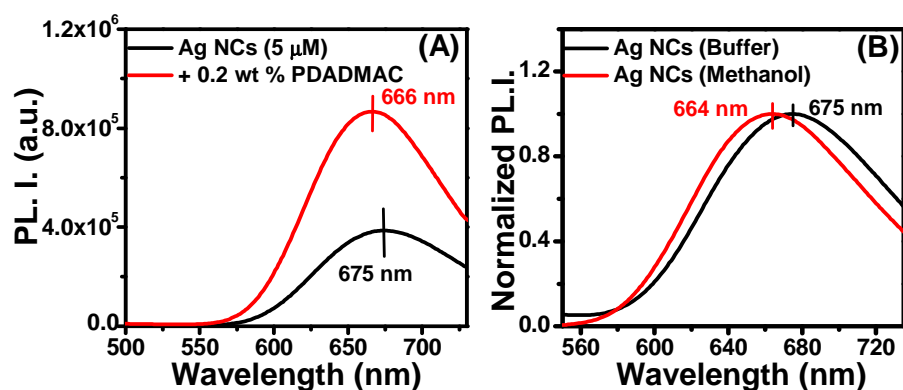


**Scheme 5.1.** Chemical structures of DAPI and DHLA-capped Ag NC. The parameter  $R_0$  indicates the distance from center of DAPI molecule to the center of Ag NC.

### 5.2.3. Effect of Ag NCs-Polymer Composite Formation on the FRET Process

Figure 5.9A displays the changes in the PL spectra of Ag NCs in the presence of 0.2 wt % PDADMAC. Ag NCs in pH 7.4 phosphate buffer show an intense PL band ( $\lambda_{ex}=375$  nm) centered at 675 nm. The luminescence properties of these Ag NCs alter significantly upon addition of 0.2 wt% PDADMAC. The luminescence quantum yield of Ag NCs increases by a factor of 2.23 and the emission maximum shifts from 675 to 666 nm with a 9 nm blue shift. These spectral changes strongly indicate specific interaction of negatively charged DHLA-capped Ag NCs with the positively charged polymer matrix. It is well known that the luminescence properties of noble metal NCs are very sensitive to the surface capping ligands [28, 41]. Efficient surface capping of these NCs results in high luminescence quantum yield. Hence, the observed enhancement in the luminescence intensity of DHLA-capped Ag NCs in the presence of PDADMAC could be due to encapsulation of Ag NCs inside the polymer

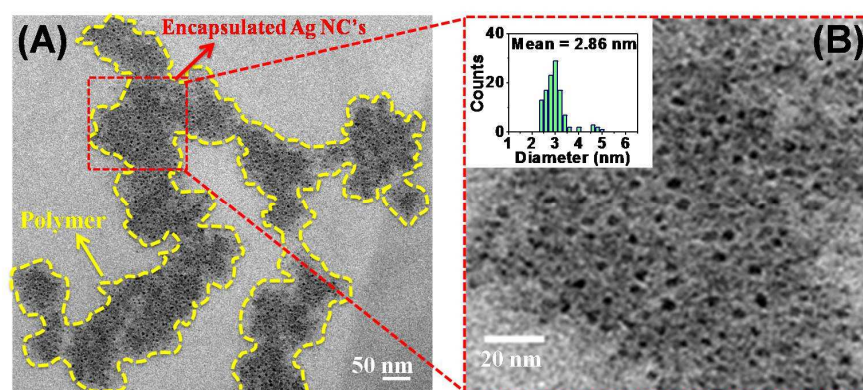
matrix. This argument gains support from the observed 9 nm blue shift in the emission maximum of Ag NCs in the presence of PDADMAC. A control experiment with less polar methanol solvent shows similar 11 nm blue shifts in the emission maximum of Ag NCs compared to that in aqueous buffer (Figure 5.9B). Hence, the blue shift in the emission maximum of Ag NCs observed in the presence of PDADMAC could be due to the less polar environment of PDADMAC matrix compared to the bulk aqueous medium. These observations can be explained by considering effective encapsulation of Ag NCs by the positively charged PDADMAC.



**Figure 5.9.** (A) Changes in the PL spectra ( $\lambda_{ex} = 375$  nm) of Ag NCs upon addition of 0.2 wt% PDADMAC. (B) Normalized PL spectra of Ag NCs in buffer (black line) and methanol (red line).

To support this argument, the morphology of Ag NCs-PDADMAC composite system through HRTEM measurements has been visualized. Figure 5.10A displays the HRTEM image of Ag NCs-PDADMAC composite system. It is evident that all the Ag NCs are encapsulated in the polymer matrix. Notably, any Ag NCs have not been seen outside the polymer matrix. Figure 5.10B shows the magnified portion of a selected area of Figure 5.10A, where individual polymer encapsulated NC is

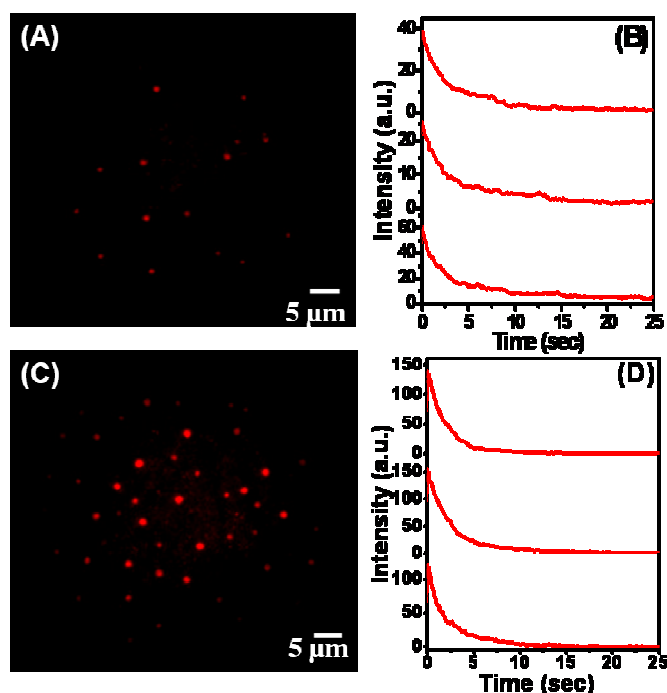
clearly visible. The inset of Figure 5.10B shows the size distribution histogram of the polymer encapsulated Ag NCs. The size varies from 2.25 to 4.95 nm with an average size of  $2.86 \pm 0.56$  nm. These HRTEM results reveal that the positively charged PDADMAC polymer efficiently encapsulates these negatively charged DHLA-capped Ag NCs through favorable electrostatic interactions. Further evidence of polymer encapsulation comes from PL imaging of individual Ag NC in the absence and presence of PDADMAC.



**Figure 5.10.** (A) HRTEM image of Ag NCs-PDADMAC composite system. (B) A zoomed portion of image (A) showing encapsulated Ag NCs inside the PDADMAC matrix. The inset shows the size distribution histogram of encapsulated Ag NCs estimated from the HRTEM measurements.

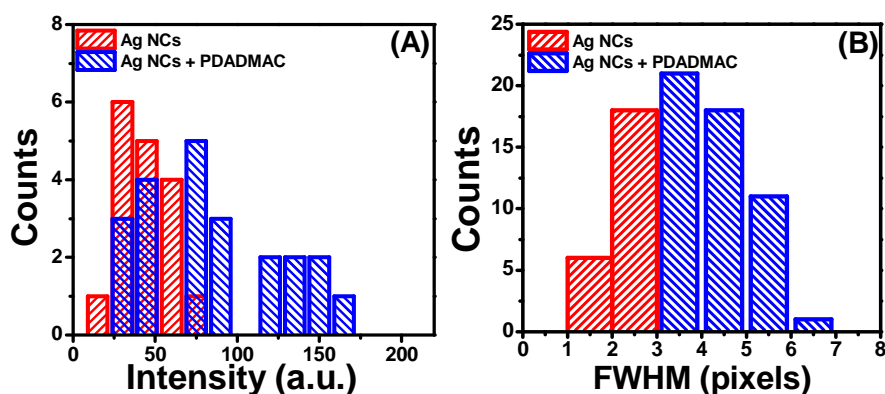
To explore the PL behavior of individual Ag NC in the absence and presence of PDADMAC, PL microscopy with an excitation wavelength of 457 nm from an argon ion laser (CW) has been performed. Figure 5.11A shows the PL image of Ag NCs on a clean glass coverslip. Localised diffraction limited (FWHM~1-3 pixels) luminescent spots have been observed from individual Ag NC. Intensity traces of these luminescent spots reveal no characteristic blinking (luminescence on/off)

phenomenon (Figure 5.11B). Most of these luminescent spots photobleach within few seconds ( $\sim 10$  sec). Earlier, Dickson and co-workers observed similar non-blinking single-molecule intensity traces of individual DNA-encapsulated Ag NCs [42]. However, in contrary to their DNA-encapsulated Ag NCs, our DHLA-capped Ag NCs photobleach very fast. Figure 5.11C shows the PL behavior of Ag NC in the presence of 0.2 wt% PDADMAC. It is evident that each of the luminescent spots in the presence of 0.2 wt% PDADMAC becomes brighter compared to Ag NC alone. Figure 5.11D displays the PL intensity traces of three selected luminescent spots. Similar fast photobleaching with no characteristic blinking has been observed for Ag NCs embedded in 0.2 wt% PDADMAC.



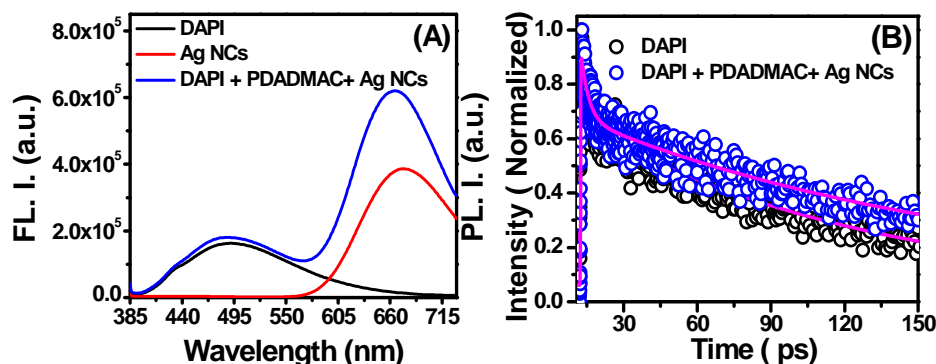
**Figure 5.11.** (A) PL image and (B) intensity traces of individual Ag NCs. (C) PL image and (D) intensity traces of PDADMAC encapsulated Ag NCs.

Moreover, careful analysis of these luminescent spots in the absence and presence of PDADMAC reveals broader distribution of FWHM and higher luminescence intensity in the presence of PDADMAC (Figure 5.12). These observations correlate well with the earlier obtained results from HRTEM and steady-state PL measurements. The broader FWHM distribution (2-6 pixels) of luminescent spots in Ag NCs-polymer composite system might originate from co-localization of more than one Ag NC at the same luminescent spot during surface deposition. This possibility gain support from earlier observation of increased mean size of these NCs in Ag NCs-polymer composite system from HRTEM measurements. Similarly, the average intensity of each of these luminescent spots in Ag NCs-polymer composite system increases significantly, as compared to Ag NCs alone, which is similar to the enhanced PL quantum yield in steady-state PL measurements. Hence, these luminescence characteristics of Ag NC in the absence and presence of PDADMAC strongly support the formation of Ag NC-polymer composite system.



**Figure 5.12.** Distribution histogram of (A) intensity and (B) FWHM of Ag NCs in the absence and presence of 0.2 wt% PDADMAC.

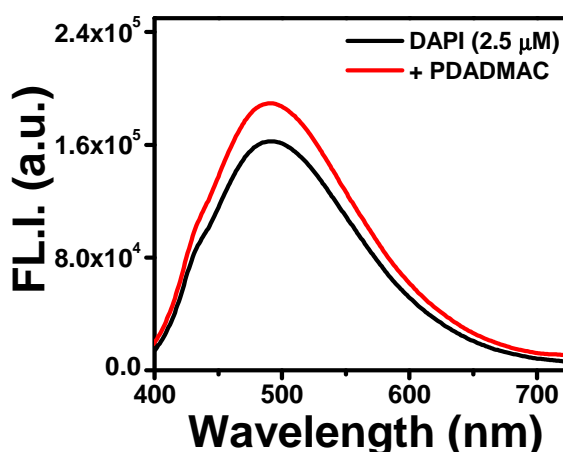
Next, the influence of Ag NCs-polymer composite formation on the extent of nonradiative FRET process between DAPI and Ag NC was monitored. Figure 5.13A shows the changes in the fluorescence spectra of DAPI in the absence and presence of Ag NCs-polymer composite. For comparison, the PL spectrum ( $\lambda_{ex} = 375$  nm) of Ag NCs alone is also shown in Figure 5.13A. Interestingly, the fluorescence quantum yield of DAPI remains almost unchanged in the presence of PDADMAC encapsulated Ag NCs (Figure 5.13A). On the other hand, a noticeable increase in the PL quantum yield of Ag NCs has been observed at 675 nm for the Ag NCs-polymer-DAPI system, compared to Ag NCs alone, which is similar to that has been observed earlier due to polymer encapsulation of Ag NCs.



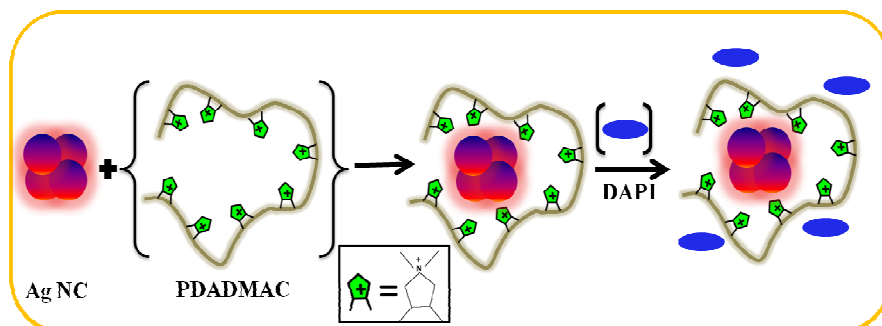
**Figure 5.13.** (A) Changes in the fluorescence spectra ( $\lambda_{ex} = 375$  nm) of DAPI (black line) and Ag NCs (red line) upon formation of DAPI-PDADMAC-Ag NCs composite (blue line). (B) Femtosecond fluorescence transients ( $\lambda_{ex} = 375$  nm) of DAPI in the absence (black) and presence (blue) of PDADMAC-Ag NCs composite recorded at 490 nm emission wavelength.

Figure 5.13B displays the fluorescence lifetime decay traces of DAPI in the absence and presence of Ag NCs-PDADMAC composite. As

mentioned earlier, DAPI in aqueous buffer shows very short fluorescence lifetime of 81.50 ps with lifetime components of  $2.35 \pm 0.18$  ps (31%) and  $117.90 \pm 1.96$  ps (69%) (Table 5.1). Notably, the fluorescence lifetime of DAPI does not quench in the presence of Ag NCs-PDADMAC composite. The average fluorescence lifetime of DAPI in the presence of Ag NCs-PDADMAC composite shows a value of 115.90 ps with lifetime components of  $3.21 \pm 0.23$  ps (29%) and  $161.94 \pm 2.98$  ps (71%). This nominal increase in DAPI lifetime in the presence of Ag NCs-PDADMAC composite could be due to the increased hydrophobicity from the hydrocarbon side chains of polymer. Similar minor but noticeable increase in fluorescence quantum yield of DAPI has been observed upon addition of PDADMAC in steady-state measurement (Figure 5.14). These observations reveal that the nonradiative FRET process between DAPI and Ag NCs completely suppresses due to the compartmentalization of Ag NCs inside the polymer matrix (Scheme 5.2). Next, the effect of selective compartmentalization of donor (DAPI) on the FRET process was investigated.



**Figure 5.14.** Changes in the fluorescence spectra of DAPI ( $\lambda_{ex} = 375$  nm) upon addition of 0.2 wt % PDADMAC.



**Scheme 5.2.** Schematic representation of the proposed polymer encapsulation of Ag NCs and subsequent modulation of nonradiative FRET process between DAPI and Ag NCs.

#### 5.2.4. Effect of DNA Binding of DAPI on the FRET Process

DAPI is an efficient DNA binding fluorescence marker and shows strong binding affinity with the minor-groove of DNA. In the present study, this phenomenon has been utilized for selective compartmentalization of DAPI (donor) from Ag NCs (acceptor). The aim is to know whether this selective compartmentalization of donor has any influence on the observed FRET process or not. Figure 5.15A shows the changes in the absorption spectra of DAPI in the absence and presence of 10  $\mu\text{M}$  CT-DNA. DAPI shows an absorption maximum at 340 nm in pH 7.4 phosphate buffer. However, in the presence of CT-DNA, the absorption peak shifts to 350 nm with a 10 nm red shift, signifying binding of DAPI with DNA (Figure 5.15A). On the other hand, the fluorescence spectrum ( $\lambda_{\text{ex}} = 375$  nm) of DAPI exhibits a peak at 492 nm (Figure 5.15B). Upon addition of CT-DNA, this peak shifts to 466 nm with a 26 nm blue shifts. Moreover, a significant increase ( $\sim 7$  times) in fluorescence quantum yield has been observed in the presence of CT-DNA. This blue

shift with enhanced fluorescence from DAPI in the presence of CT-DNA clearly indicates that DAPI experiences more hydrophobic environment compared to bulk aqueous medium.

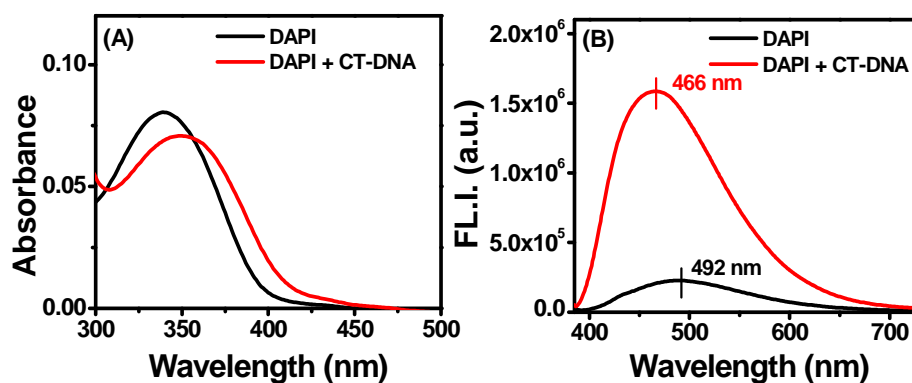


**Figure 5.15.** (A) Absorption spectra and (B) fluorescence spectra of DAPI ( $2.5 \mu\text{M}$ ,  $\lambda_{ex} = 375 \text{ nm}$ ) in the absence (black line) and presence (red line) of  $10 \mu\text{M}$  CT-DNA.

In addition, the fluorescence lifetime of DAPI increases appreciably from 81.50 ps to 1.62 ns in the presence of CT-DNA (Table 5.1 & 5.3). Similar kinds of spectral changes have been observed earlier for DAPI bound to various hydrophobic host molecules [38, 39]. Earlier, it has been shown that DAPI binds to the AT base pairs of the minor groove of CT-DNA [43, 44]. Hence, on the basis of the previous literature and the present results, it can be stated that DAPI strongly binds to the minor groove of CT-DNA. Here it is important to mention that CT-DNA does not alter the PL characteristics of Ag NCs (Figure 5.16), indicating negligible interactions between the two. Next, the influence of this selective DNA binding of DAPI on the extent of FRET between DAPI and Ag NCs was investigated.

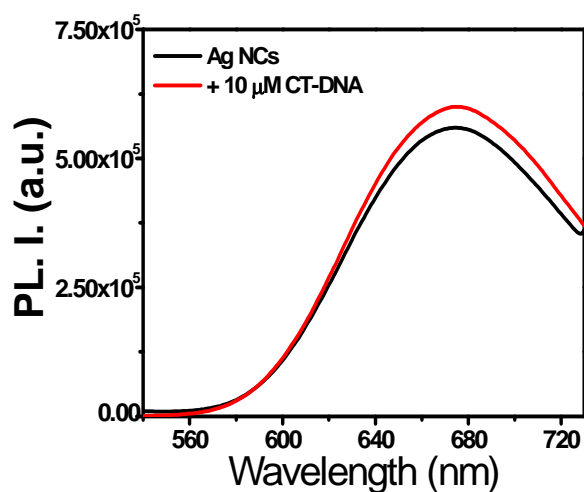


**Figure 5.16.** Changes in the PL spectra of Ag NCs upon addition of CT-DNA.

Figure 5.17A shows the fluorescence spectra ( $\lambda_{\text{ex}} = 375$  nm) of DNA bound DAPI in the absence and presence of Ag NCs. For comparison, Figure 5.17A also displays the emission spectra of DAPI and Ag NCs at 375 nm excitation. DNA bound DAPI shows a fluorescence peak ( $\lambda_{\text{ex}} = 375$  nm) at 466 nm. The peak position and intensity of this fluorescence band of DNA bound DAPI remain unaltered in the presence of Ag NCs. Moreover, a red-shifted emission band centered at 670 nm has been observed for DAPI-DNA-Ag NC composite system, which can be assigned to luminescence from Ag NCs. These unchanged emission characteristics of DNA bound DAPI and Ag NCs in the mixture indicate complete suppression of nonradiative FRET process. To further substantiate this possibility, the changes in fluorescence lifetime of DNA bound DAPI in the absence and presence of Ag NCs have been measured. Figure 5.17B shows the lifetime decay traces of DNA bound DAPI in the absence and presence of Ag NCs recorded at 440 nm emission wavelength. All the decays were fitted with a bi-exponential decay function. DNA bound DAPI shows an average lifetime of  $1.62 \pm 0.02$  ns

with lifetime components of 0.63 ns (51%) and 2.64 ns (49%) (Table 5.3). The lifetime of DNA bound DAPI remains unaltered in the presence of Ag NCs. The average lifetime of DNA bound DAPI shows a value of  $1.68 \pm 0.03$  ns with lifetime components of 0.50 ns (35%) and 2.32 ns (65%) in the presence of Ag NCs (Table 5.3).

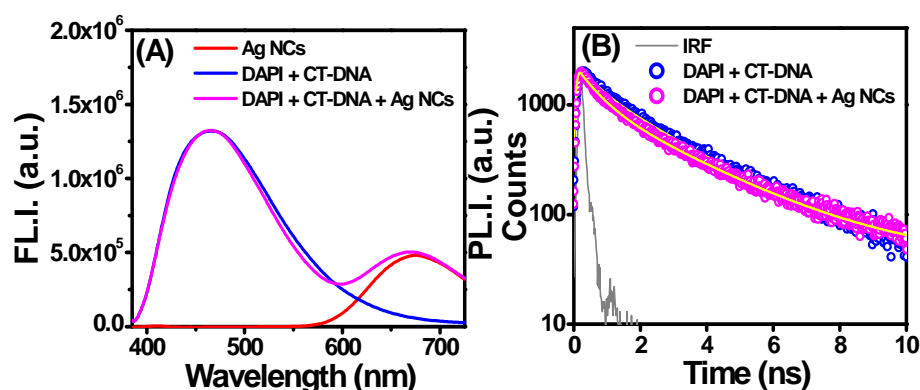
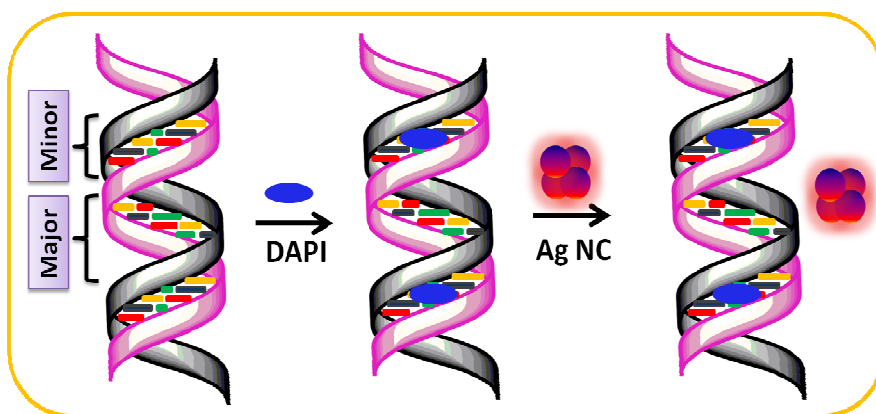


**Figure 5.17.** (A) Changes in the fluorescence spectra ( $\lambda_{ex} = 375$  nm) of DAPI-DNA complex (blue line) and Ag NCs (red line) upon formation of DAPI-DNA-Ag NCs composite (pink line). (B) Changes in the PL lifetime traces ( $\lambda_{ex} = 375$  nm) of DAPI-DNA complex (blue) in the presence of  $5 \mu\text{M}$  Ag NCs recorded at 440 nm emission wavelength.

**Table 5.3.** Fluorescence decay parameters of DAPI in the presence of CT-DNA and CT-DNA-Ag NCs system.

System	$\tau_1$ (ns)	$a_1$	$\tau_2$ (ns)	$a_2$	$\langle\tau\rangle$ (ns)	$\chi^2$
DAPI + CT-DNA	0.63	0.51	2.64	0.49	$1.62 \pm 0.02$	1.06
+ Ag NCs	0.50	0.35	2.32	0.65	$1.68 \pm 0.03$	1.08

Hence, these results reveal selective and complete compartmentalization of DAPI within CT-DNA and subsequent suppression of nonradiative FRET process between DAPI and Ag NCs (Scheme 5.3).



**Scheme 5.3.** Illustration of the effect of DNA binding of DAPI on the nonradiative FRET process between DAPI and Ag NCs.

### 5.3. Conclusions

In the present work, the fundamental mechanism behind the fluorescence quenching of DAPI in the presence of ultras-small Ag NCs and its subsequent modulation in the presence of PDADMAC polymer and CT-DNA has been addressed. The fluorescence of DAPI significantly quenches in the presence of Ag NCs. Importantly, the concomitant increase in the luminescence intensity of Ag NCs clearly signifies the involvement of FRET from DAPI to Ag NCs. This fluorescence quenching is predominantly nonradiative in nature with significant shortening of excited-state lifetime of DAPI. This nonradiative FRET process completely suppresses in the presence of a cationic polymer

PDADMAC. Steady-state PL, HRTEM, PL imaging measurements revealed efficient and complete encapsulation of acceptor (Ag NCs) within the polymer matrix. The effect of selective compartmentalization of donor (DAPI) on the FRET process is also demonstrated in the presence of CT-DNA. It has been observed that the nonradiative FRET process completely suppresses in the presence of CT-DNA due to the selective binding of DAPI with CT-DNA.

### 5.4. References

1. Wang S., Vafabakhsh R., Borschel W. F., Ha T., Nichols C. G. (2016), Structural dynamics of potassium channel gating revealed by single molecule FRET, *Nat. Struct. Mol. Biol.*, 23, 31-36. (DOI: 10.1038/nsmb.3138)
2. Arslan S., Khafizov R., Thomas C. D., Chemla Y. R., Ha T. (2015), Protein structure. Engineering of a superhelicase through conformational control, *Science*, 348, 344-347. (DOI: 10.1126/science.aaa0445)
3. Clapp A. R., Medintz I. L., Mauro J. M., Fisher B. R., Bawendi M. G., Mattoussi H. (2004), Fluorescence resonance energy transfer between quantum dot donors and dye-labeled protein acceptors, *J. Am. Chem. Soc.*, 126, 301-310. (DOI: 10.1021/ja037088b)
4. Medintz I. L., Clapp A. R., Mattoussi H., Goldman E. R., Fisher B., Mauro J. M. (2003), Self-assembled nanoscale biosensors based on quantum dot FRET donors, *Nat. Mater.*, 2, 630-638. (DOI: 10.1038/nmat961)
5. Naiki H., Masuhara A., Masuo S., Onodera T., Kasai H., Oikawa H. (2013), Highly controlled plasmonic emission enhancement from metal-semiconductor quantum dot complex nanostructures, *J. Phys. Chem. C*, 117, 2455-2459. (DOI: 10.1021/jp305408p)
6. Li M., Cushing S. K., Wang Q., Shi X., Hornak L. A., Hong Z., Wu N. (2011), Size-dependent energy transfer between CdSe/ZnS quantum dots and gold nanoparticles, *J. Phys. Chem. Lett.*, 2, 2125-2129. (DOI: 10.1021/jz201002g)

7. Sen T., Patra A. (2012), Recent advances in energy transfer processes in gold-nanoparticle-based assemblies, *J. Phys. Chem. C*, 116, 17307-17317. (DOI: 10.1021/jp302615d)
8. Quach A. D., Crivat G., Tarr M. A., Rosenzweig Z. (2011), Gold nanoparticle-quantum dot-polystyrene microspheres as fluorescence resonance energy transfer probes for bioassays, *J. Am. Chem. Soc.*, 133, 2028-2030. (DOI: 10.1021/ja109348d)
9. Kuhnke K., Becker R., Epple M., Kern K. (1997),  $C_{60}$  exciton quenching near metal surfaces, *Phys. Rev. Lett.*, 79, 3246-3249. (DOI: 10.1103/PhysRevLett)
10. Dulkeith E., Morteani A. C., Niedereichholz T., Klar T. A., Feldmann J., Levi S. A., van Veggel F. C. J. M., Reinhoudt D. N., Moller M., Gittins D. I. (2002), Fluorescence quenching of dye molecules near gold nanoparticles: Radiative and nonradiative effects, *Phys. Rev. Lett.*, 89, 203002. (DOI: 10.1103/PhysRevLett.89.203002)
11. Dulkeith E., Ringler M., Klar T. A., Feldmann J., Muñoz Javier A., Parak W. J. (2005), Gold nanoparticles quench fluorescence by phase induced radiative rate suppression, *Nano Lett.*, 5, 585-589. (DOI: 10.1021/nl0480969)
12. Cannone F., Chirico G., Bizzarri A. R., Cannistraro S. (2006), Quenching and blinking of fluorescence of a single dye molecule bound to gold nanoparticles, *J. Phys. Chem. B*, 110, 16491-16498. (DOI: 10.1021/jp0625816)
13. Pons T., Medintz I. L., Sapsford K. E., Higashiya S., Grimes A. F., English D. S., Mattoussi H. (2007), On the quenching of

semiconductor quantum dot photoluminescence by proximal gold nanoparticles, *Nano Lett.*, 7, 3157-3164. (DOI: 10.1021/nl071729+)

14. Jennings T. L., Singh M. P., Strouse G. F. (2006), Fluorescent lifetime quenching near  $d=1.5$  nm gold nanoparticles: Probing NSET validity, *J. Am. Chem. Soc.*, 128, 5462-5467. (DOI: 10.1021/ja0583665)

15. Yun C. S., Javier A., Jennings T., Fisher M., Hira S., Peterson S., Hopkins B., Reich N. O., Strouse, G. F. (2005), Nanometal surface energy transfer in optical rulers, breaking the FRET barrier, *J. Am. Chem. Soc.*, 127, 3115-3119. (DOI: 10.1021/ja043940i)

16. Sen T., Sadhu S., Patra A., Surface energy transfer from rhodamine 6G to gold nanoparticles: A spectroscopic ruler, *App. Phys. Lett.*, 91, 043104. (DOI: 10.1063/1.2762283)

17. Prajapati R., Chatterjee S., Bhattacharya A., Mukherjee T. K. (2015), Surfactant-induced modulation of nanometal surface energy transfer from silicon quantum dots to silver nanoparticles, *J. Phys. Chem. C*, 119, 13325-13334. (DOI: 10.1021/acs.jpcc.5b02903)

18. Breshike C. J., Riskowski R. A., Strouse G. F. (2013), Leaving Förster resonance energy transfer behind: Nanometal surface energy transfer predicts the size-enhanced energy coupling between a metal nanoparticle and an emitting dipole, *J. Phys. Chem. C*, 117, 23942-23949. (DOI: 10.1021/jp407259r)

19. Gwinn E., Schultz D., Copp S. M., Swasey S. (2015), DNA-protected silver clusters for nanophotonics, *Nanomaterials*, 5, 180-207. (DOI: 10.3390/nano5010180)

20. Berry R. S., Smirnov B. M. (2009), Phase transitions in metal clusters and cluster catalysts, *J. Phys. Chem. A*, 113, 14220-14226. (DOI: 10.1021/jp9017053)
21. Murakami Y., Konishi K. (2007), Remarkable co-catalyst effect of gold nanoclusters on olefin oxidation catalyzed by a manganese-porphyrin complex, *J. Am. Chem. Soc.*, 2007, 129, 14401-14407. (DOI: 10.1021/ja075051b)
22. Li G., Abroshan H., Chen Y., Jin R., Kim H. J. (2015), Experimental and mechanistic understanding of aldehyde hydrogenation using Au<sub>25</sub> nanoclusters with lewis acids: Unique sites for catalytic reactions, *J. Am. Chem. Soc.*, 137, 14295-14304. (DOI: 10.1021/jacs.5b07716)
23. Smerieri M., Pal J., Savio L., Vattuone L., Ferrando R., Tosoni S., Giordano L., Pacchioni G., Rocca M., (2015), Spontaneous oxidation of Ni nanoclusters on MgO monolayers induced by segregation of interfacial oxygen, *J. Phys. Chem. Lett.*, 6, 3104-3109. (DOI: 10.1021/acs.jpcllett.5b01362)
24. Lin C. A., Yang T. Y., Lee C. H., Huang S. H., Sperling R. A., Zanella M., Li J. K., Shen J. L., Wang H. H., Yeh H. I., Parak W. J., Chang W. H. (2009), Synthesis, characterization, and bioconjugation of fluorescent gold nanoclusters toward biological labeling applications, *ACS Nano*, 3, 395-401. (DOI: 10.1021/nm800632j)
25. Jiang H., Xu G., Sun Y., Zheng W., Zhu X., Wang B., Zhang X., Wang G. (2015), A “turn-on” silver nanocluster based fluorescent sensor for folate receptor detection and cancer cell imaging under visual analysis, *Chem. Comm.*, 51, 11810-11813. (DOI: 10.1039/C5CC02061A)

26. Das N. K., Ghosh S., Priya A., Datta S., Mukherjee S. (2015), Luminescent copper nanoclusters as a specific cell-imaging probe and a selective metal ion sensor, *J. Phys. Chem. C*, 119, 24657-24664. (DOI: 10.1021/acs.jpcc.5b08123)
27. Xia N., Yang J., Wu Z. (2015), Fast, high-yield synthesis of amphiphilic Ag nanoclusters and the sensing of Hg<sup>2+</sup> in environmental samples, *Nanoscale*, 7, 10013-10020. (DOI: 10.1039/c5nr00705d)
28. Li M., Cushing S. K., Wang Q., Shi X., Hornak L. A., Hong Z., Wu N. (2011), Size-dependent energy transfer between CdSe/ZnS quantum dots and gold nanoparticles, *J. Phys. Chem. Lett.*, 2, 2125-2129. (DOI: 10.1021/jz201002g)
29. Muhammed M. A., Shaw A. K., Pal S. K., Pradeep T. (2008), quantum clusters of gold exhibiting FRET, *J. Phys. Chem. C*, 112, 14324-14330. (DOI: 10.1021/jp804597r)
30. Bain D., Paramanik B., Sadhu S., Patra A. (2015), A study into the role of surface capping on energy transfer in metal cluster-semiconductor nanocomposites, *Nanoscale*, 7, 20697-20708. (DOI: 10.1039/c5nr06793f)
31. Adhikari B., Banerjee A. (2010), Facile synthesis of water-soluble fluorescent silver nanoclusters and Hg(II) sensing, *Chem. Mater.*, 22, 4364-4371. (DOI: 10.1021/cm1001253)
32. Chen W. T., Hsu Y. J., P. V. Kamat (2012), Realizing visible photoactivity of metal nanoparticles: Excited-state behavior and electron-transfer properties of silver (Ag<sub>8</sub>) clusters, *J. Phys. Chem. Lett.*, 3, 2493-2499. (DOI: 10.1021/jz300940c)
33. Yuan X., Luo Z., Zhang Q., Zhang X., Zheng Y., Lee J. Y., Xie, J. (2011), Synthesis of highly fluorescent metal (Ag, Au, Pt, and Cu)

- nanoclusters by electrostatically induced reversible phase transfer, *ACS Nano*, 5, 8800-8808. (DOI: 10.1021/nn202860s)
34. Negishi Y., Arai R., Niihori Y., Tsukuda T. (2011), Isolation and structural characterization of magic silver clusters protected by 4-(tert-butyl)benzyl mercaptan, *Chem. Commun.*, 47, 5693-5695. (DOI: 10.1039/C0CC05587E)
35. Rao T. U. B., Pradeep T. (2010), Luminescent Ag<sub>7</sub> and Ag<sub>8</sub> clusters by interfacial synthesis, *Angew. Chem., Int. Ed.*, 49, 3925-3929. (DOI: 10.1002/anie.200907120)
36. Rao T. U. B., Nataraju B., Pradeep T. (2010), Ag<sub>9</sub> quantum cluster through a solid-state route, *J. Am. Chem. Soc.*, 132, 16304-16307. (DOI: 10.1021/ja105495n)
37. Willard D. M., Carillo L. L., Jung J., Orden A. V. (2001), CdSe-ZnS quantum dots as resonance energy transfer donors in a model protein-protein binding assay, *Nano Lett.*, 1, 469-474. (DOI: 10.1021/nl015565n)
38. Banerjee D., Pal S. K. (2008), Excited-state solvation and proton transfer dynamics of DAPI in biomimetics and genomic DNA, *J. Phys. Chem. A*, 112, 7314-7320. (DOI: 10.1021/jp801778e)
39. Shinde M. N., Bhasikuttan A. C., Mohanty J. (2015), The contrasting recognition behavior of  $\beta$ -cyclodextrin and its sulfobutylether derivative towards 4', 6-diamidino-2-phenylindole, *ChemPhysChem*, 16, 3425-3432. (DOI: 10.1002/cphc.201500638)
40. Lakowicz J. R., (1999), *Principles of fluorescence spectroscopy*, 2nd ed., Academic Press, New York. (ISBN: 0-306-46093-9)
41. Chen Y. S., Kamat P. V. (2014), Glutathione-capped gold nanoclusters as photosensitizers, visible light-induced hydrogen

- generation in neutral water, *J. Am. Chem. Soc.*, 136, 6075-6082. (DOI: 10.1021/ja5017365)
42. Vosch T., Antoku Y., Hsiang J. C., Richards C. I., Gonzalez J. I., Dickson R. M. (2007), Strongly emissive individual DNA-encapsulated Ag nanoclusters as single-molecule fluorophores, *Proc. Natl. Acad. Sci. U. S. A.*, 104, 12616-12621. (DOI: 10.1073/pnas.0610677104)
43. Manzini G., Barcellona M. L., Avitabile M., Quadrifoglio F. (1983), Interaction of diamidino-2-phenylindole (DAPI) with natural and synthetic nucleic acids, *Nucleic Acids Res.*, 11, 8861-8875. (DOI: 10.1093/nar/11.24.8861)
44. Barcellona M. L., Gratton E. (1996), Torsional dynamics and orientation of DNA-DAPI complexes, *Biochemistry*, 35, 321-333. (DOI: 10.1021/bi951027b)

**Chapter 6**

*Effect of Surfactant Assemblies on the  
Resonance Energy Transfer from 4',6-  
diamidino-2-phenylindole to Silver  
Nanoclusters*

### 6.1. Introduction

Förster resonance energy transfer (FRET) has become one of the most widely used experimental tools in a variety of fields including single molecule investigation of DNA and proteins, light harvesting by model photosynthetic systems and supramolecular aggregates and nanoparticle-based sensors [1-9]. FRET is a nonradiative process whereby an excited donor transfers its energy to a proximal ground state acceptor through dipole-dipole interactions [10]. The rate of energy transfer depends upon various factors such as the extent of spectral overlap, the relative orientation of the transition dipoles and most importantly, the distance between the donor and acceptor molecules which should be in the range of 2-10 nm [10].

Over the past few years, numerous investigations have been executed on the structural and photophysical aspects of molecules entrapped in protein environments, DNA, micelles, reverse micelles, vesicles or various nanocavities due to the promising effects of confined assemblies on photophysical and biological phenomena [11-19]. Recently, due to the explicit distance dependence of FRET, it has been extensively used to characterize biologically relevant model membrane systems such as micelles and reverse micelles [20-24]. For example, Liu et al. (2013) investigated the concentration effect of the sulfonated Gemini surfactant on the FRET from acridine orange to rhodamine B [25]. Initially, with increase in surfactant concentration, the FRET efficiency increased almost linearly. Thereafter upon further addition of the surfactant, the FRET efficiency declined sharply due to the formation of large surfactant aggregates, which ultimately increased the distance between the donor and acceptor. In another study, Roy et al. (2016) performed a comparative

FRET study in pluronic triblock copolymer micelle and noisome composed of biological component cholesterol and investigated the effect of cholesterol and sucrose on the FRET parameters [26].

Recently, we have reported that DAPI and Ag NC form an excellent FRET pair with ~78% FRET efficiency and demonstrated the effect of compartmentalization of donor and acceptor on FRET efficiency [27]. DAPI exhibits excited state intramolecular proton transfer (ESIPT) from its amidino to indole moiety [28-30]. Due to this ESIPT, DAPI undergoes fast non-radiative relaxation which significantly retards upon binding with micelles, liposomes, DNA, etc. due to perturbed ESIPT [31-35]. In the present work, we have studied the influence of surfactant assemblies of SDS on the FRET between DAPI and Ag NC. While DAPI interacts specifically with SDS surfactants in a concentration-dependent manner, Ag NC shows no specific interaction with surfactant assemblies. Our results reveal that DAPI forms aggregates with the SDS at the interface and with the increase in concentrations, it interacts with the SDS pre-micelles followed by its complete incorporation into the Stern layer of SDS micelles. These specific concentration-dependent interactions between DAPI and SDS hinder the non-radiative FRET between DAPI and Ag NC.

## 6.2. Results and Discussion

### 6.2.1. Interaction of DAPI with SDS: Steady-State FL Measurements

The absorption spectrum of DAPI shows a peak at 341 nm in pH 7.4 phosphate buffer (Figure 6.1). Significant spectral changes have been observed upon addition of SDS. At low concentrations of SDS (upto 0.6 mM), the absorbance of DAPI decreases. The absorption spectrum

broadens without any noticeable change in the peak maxima. However, on further increase in concentrations of SDS (1 to 16 mM), the absorbance of DAPI increases with gradual peak shift to a longer wavelength. At 1 mM SDS, a broad spectrum centered at 349 nm has been observed and this absorption maximum further shifts to 356 nm in the presence of 16 mM SDS.

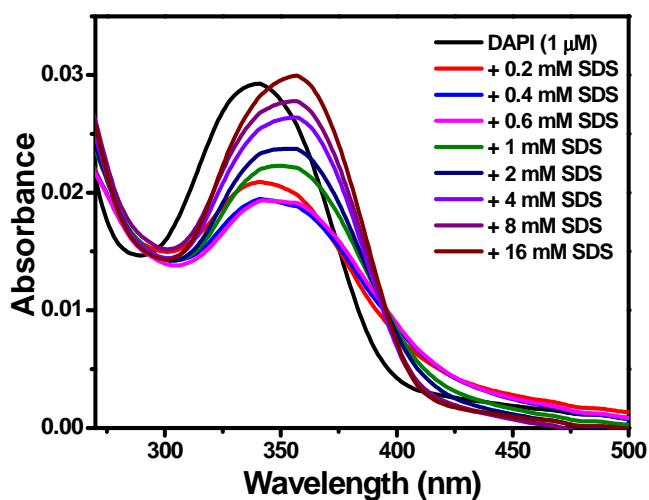


**Figure 6.1.** Changes in the absorption spectra of DAPI upon gradual addition of SDS.

Figure 6.2 shows the changes in FL spectra ( $\lambda_{\text{ex}} = 375 \text{ nm}$ ) of DAPI in the presence of different concentrations of SDS. DAPI exhibits FL maximum at 492 nm upon excitation at 375 nm (Figure 6.2A) [27]. The emission maximum of DAPI shifts to 556 nm with a red shift of 64 nm in the presence of 0.2 and 0.4 mM SDS. At 0.6 mM SDS, along with the 556 nm peak, a blue shifted peak at 472 nm has been observed. The FL maximum shifts to 470 nm with 4 and 13 fold FL enhancements in the presence of 1 and 2 mM SDS, respectively (Figure 6.2B). For

concentrations at and above 4 mM SDS, the emission maxima shift to 466 nm showing FL enhancements of 45 and 48 fold upon addition of 4 and 16 mM SDS, respectively (Figure 6.2B).

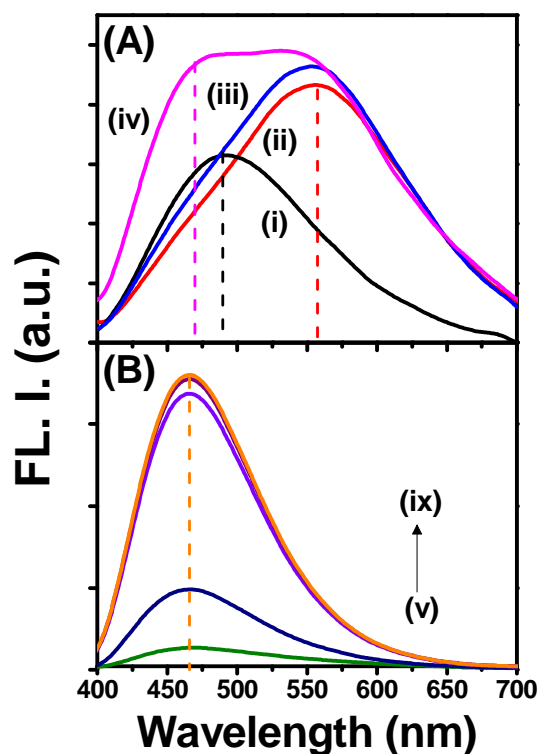


**Figure 6.2.** Changes in the FL spectra of DAPI ( $\lambda_{ex} = 375$  nm) upon addition of (A) (i) 0 mM, (ii) 0.2 mM, (iii) 0.4 mM, (iv) 0.6 mM SDS, and (B) (v) 1 mM, (vi) 2 mM, (vii) 4 mM, (viii) 8 mM, and (ix) 16 mM SDS.

Figure 6.3A shows the plot of FL intensity ratio ( $I/I_0$ ) of DAPI against concentrations of SDS.  $I$  and  $I_0$  represent fluorescence intensity of DAPI at 492 nm in the presence and absence of SDS, respectively. The sigmoidal plot illustrates that with the increase in the concentration of SDS from, the FL intensity of DAPI increases and beyond 4 mM SDS, the FL intensity saturates. To know the nature of interactions between DAPI

and SDS, we have studied the effect of non-ionic TX-100 and cationic CTAB surfactants on the FL of DAPI. Figure 6.3B displays the plot of  $I/I_0$  ( $\lambda_{em} = 492$  nm) against concentrations of TX-100 and CTAB. Figure 6.3B shows that in the presence of TX-100 (0.1-1 mM), the FL intensity of DAPI shows negligible FL enhancement of 1.6 fold, whereas FL spectrum of DAPI remains unaltered upon addition of CTAB (0.2-2 mM). Since TX-100 is a non-ionic surfactant, the negligible FL enhancement may be due to the hydrophobic environment of non-ionic TX-100 micelles. The unaltered emission of DAPI in the presence of positively charged CTAB can be explained by considering the minimal interaction between DAPI and CTAB. This is due to the electrostatic repulsion between similarly charged molecules. These results clearly indicate that 48 fold FL enhancement of DAPI in the presence of SDS is due to the specific electrostatic interactions between the positively charged DAPI and negatively charged SDS.

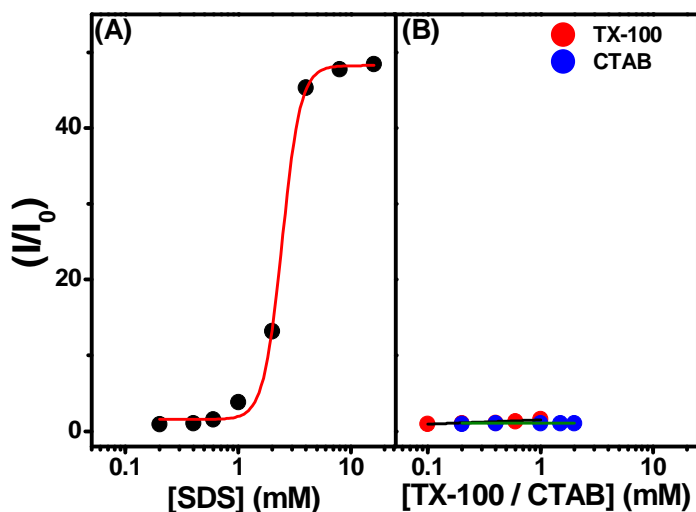


**Figure 6.3.**  $I/I_0$  ( $\lambda_{em} = 492$  nm) against concentrations of surfactant for DAPI in the presence of (A) SDS and (B) TX-100 and CTAB.

Previously, similar kind of spectral changes for various dye-surfactant systems have been reported [36-39]. At lower concentrations of SDS (0.2-0.4 mM), the changes in the absorption spectra and the red-shifted 556 nm peak in the FL spectra of DAPI can be explained by considering the formation of DAPI-SDS aggregates at the interface. The favorable electrostatic interaction between negatively charged SDS and positively charged DAPI results in aggregation. Previously, based on the spectral changes observed, the dye - surfactant aggregates are classified either as J/H-aggregates or non-specific aggregates [40-42]. In the presence of 0.2-0.4 mM SDS, the absence of peak shift in the absorption maxima along with the insignificant changes in the FL intensity of DAPI suggests that these DAPI-SDS aggregates cannot be assigned to J or H type of aggregates. Hence, these aggregates are referred to as non-specific DAPI-SDS aggregates [41]. With the gradual increase in concentrations, the surfactant monomers self-assemble to form pre-micelles followed by the formation of micelles at CMC. The enhancement in absorbance of DAPI along with 8 to 15 nm bathochromic shifts upon addition of 0.6 to 16 mM SDS, respectively reflects the association of positively charged DAPI with the negatively charged surfactant assemblies. In the presence of 0.6 mM SDS, the appearance of two FL peaks clearly indicates the interaction of DAPI with two different surfactant assemblies. The emission at 556 nm is quite similar to the emission observed due to the formation of DAPI-SDS aggregates in the presence of 0.2-0.4 mM SDS. The blue-shifted emission at 472 nm signifies the association of positively charged DAPI with the negatively charged SDS pre-micelles. The FL enhancement at 1 and 2 mM SDS with a further blue-shifted emission maximum centered at 470 nm strongly indicates the association of DAPI with the negatively charged pre-micelles

of SDS, where DAPI experiences the less polar environment as compared to aqueous medium. The CMC of SDS in water is 8 mM which reduces to 3-4 mM in phosphate buffers [43, 44]. Therefore, the sudden jump in the FL intensity of DAPI in the presence of 4 mM SDS can be rationalized by considering the incorporation of DAPI into the Stern layer of SDS micelles. The observed saturation of the FL intensity of DAPI upon further addition of SDS reveals that all the DAPI molecules get incorporated into the Stern layer of SDS micelles. Similar kind of FL enhancements with the significant blue shift in the emission maximum of DAPI have been observed in the presence of liposomes, proteins, DNA, cyclodextrin, etc. due to its specific association with these hydrophobic systems [31-35].

### 6.2.2. Time-Resolved FL Measurements: DAPI-SDS System

To get further insights of the mechanism of interaction between DAPI and SDS, we have performed time-resolved fluorescence measurements. The FL decay traces of DAPI ( $\lambda_{\text{ex}} = 375$  nm) upon gradual addition of SDS have been recorded at an emission wavelength of 492 nm (Figure 6.4A and 6.4B). All the estimated lifetime components are listed in Table 6.1.

DAPI shows single exponential FL decay with the lifetime of 0.14 ns which matches well with the earlier reports (Figure 6.4A) [32, 34]. The short lifetime of DAPI in the aqueous medium is due to the non-radiative ESIPT in the presence of water molecules. In various restricted environments, this ESIPT is hindered due to unavailability of water molecules in its vicinity, resulting in slower excited state dynamics [31-35]. Figure 6.4A displays the changes in the FL decay traces of DAPI in the presence of 0.2 to 0.6 mM SDS. For 0.2 mM SDS, DAPI exhibits bi-

exponential decay with an average FL lifetime of 0.24 ns having lifetime components of 0.14 (88%) and 0.96 (12%) ns. At 0.4 mM SDS, the average FL lifetime increases to 0.30 ns with lifetime components of 0.15 (83%) and 1.05 (17%) ns. In the presence of 0.2 mM SDS, the 0.14 ns component matches with the FL lifetime of free DAPI in the aqueous medium, whereas 0.96 ns component can be assigned to the DAPI-SDS non-specific aggregates formed at the interface. For 0.4 mM SDS, the free DAPI component further decreases with an increase in the contribution from DAPI-SDS aggregates.

Upon addition of 0.6 mM SDS, DAPI shows tri-exponential decay kinetics having average lifetime of 0.67 ns with lifetime components of 0.19 (53%), 0.95 (37%) and 2.18 (10%) ns. The free DAPI component further decreases with an increase in contribution from DAPI-SDS aggregates. The additional 2.18 ns lifetime component can be assigned to the pre-micelles associated DAPI. These lifetime components of DAPI in the presence of 0.6 mM SDS clearly reveal the existence of free DAPI, DAPI-SDS aggregates at the interface and pre-micelles associated DAPI. The lifetime of pre-micelles associated DAPI increases due to the perturbed ESIPT. Figure 6.4B shows the changes in the FL decay traces of DAPI upon further addition of 1 to 16 mM SDS. At 1 mM SDS, DAPI has an average lifetime of 1.13 ns with lifetime components of 0.17 (31%), 0.86 (31%) and 2.15 (38%) ns. For 2 mM SDS, the average lifetime becomes 1.42 ns with lifetime components of 0.16 (26%), 1.18 (32%) and 2.40 (42%) ns. These FL lifetime results show the enhanced contribution of the component assigned to pre-micelles associated DAPI in the presence of 1 and 2 mM SDS.

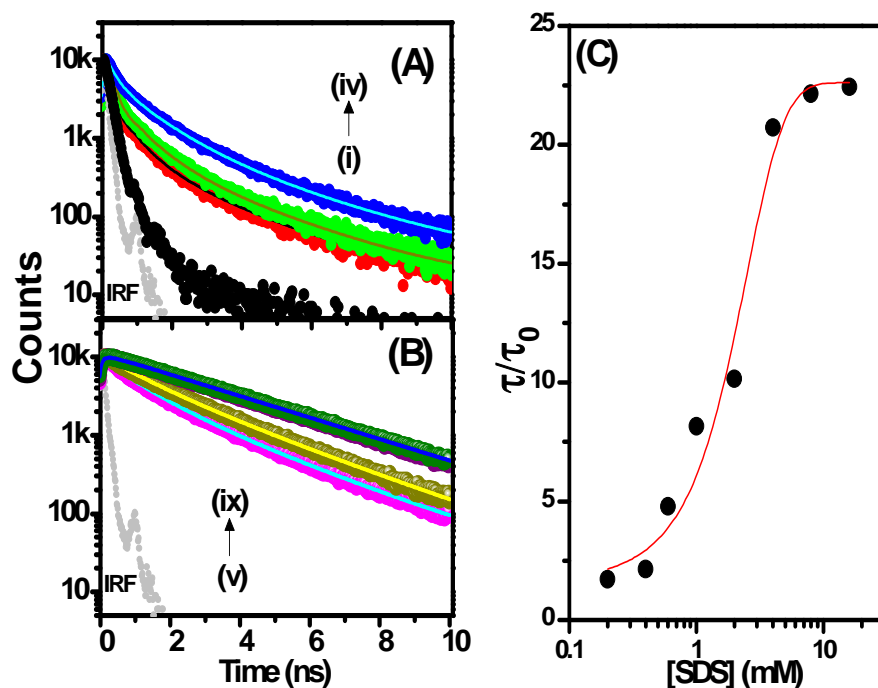


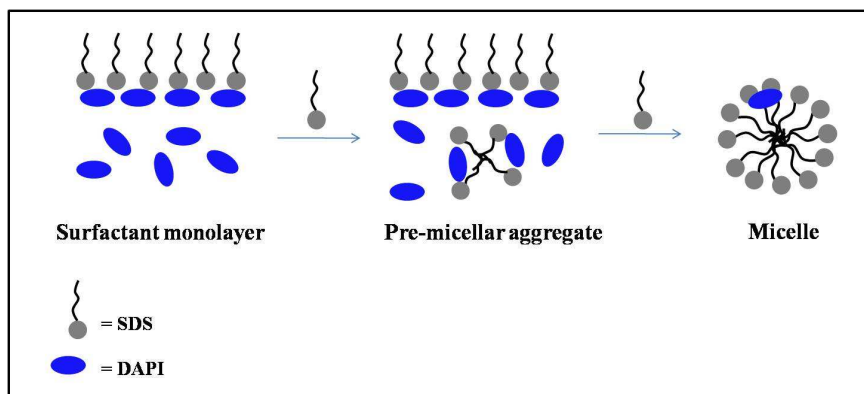
**Figure 6.4.** (A) Changes in the FL lifetime decay traces of DAPI ( $\lambda_{ex} = 375$  nm) in the presence of (A) (i) 0 mM, (ii) 0.2 mM, (iii) 0.4 mM, (iv) 0.6 mM SDS, and (B) (v) 1 mM, (vi) 2 mM, (vii) 4 mM, (viii) 8 mM, and (ix) 16 mM SDS recorded at 492 nm emission wavelength. (C)  $\tau/\tau_0$  ( $\lambda_{em} = 492$  nm) against concentrations of SDS for DAPI-SDS system.

DAPI shows single exponential decay kinetics at and above 4 mM SDS concentration (Figure 6.4B). In the presence of 4 mM SDS, the FL lifetime of DAPI increases to 2.90 ns, which further enhances to 3.10 and 3.14 ns upon addition of 8 and 16 mM SDS, respectively. It is important to mention here that upon micellization, i.e. at  $\text{SDS} \geq 4$  mM, the single exponential decays of DAPI clearly indicate the association of DAPI to only one type of surfactant assembly. In phosphate buffer, since the CMC of SDS is  $\sim 3$ -4 mM, these lifetime data reveal complete incorporation of DAPI into the Stern layer of SDS micelles, where it experiences the less

polar environment in comparison with the aqueous medium. As a result of this incorporation, the ESIPT is hindered resulting in an enhanced FL lifetime of DAPI. Figure 6.4C shows the plot of the ratio of average FL lifetime ( $\tau/\tau_0$ ) versus concentrations of SDS for DAPI-SDS system. The parameters  $\tau$  and  $\tau_0$  are the average FL lifetimes of DAPI in the presence and absence of SDS. Based on the steady-state and time-resolved results, the specific interaction between DAPI and different surfactant assemblies of SDS is illustrated in Scheme 6.1.

**Table 6.1.** *Fluorescence decay parameters of DAPI in the presence of different concentrations of SDS.*

<b>Sample</b>	$\tau_1$ (ns)	$a_1$	$\tau_2$ (ns)	$a_2$	$\tau_3$ (ns)	$a_3$	$\tau_{\text{avg}}$ (ns)	$\chi^2$
<b>DAPI</b>	0.14	1.0	-	-	-	-	0.14	1.09
<b>+ 0.2 mM SDS</b>	0.14	0.88	0.96	0.12	-	-	0.24	1.16
<b>+ 0.4 mM SDS</b>	0.15	0.83	1.05	0.17	-	-	0.30	1.15
<b>+ 0.6 mM SDS</b>	0.19	0.53	0.95	0.37	2.18	0.10	0.67	1.16
<b>+ 1 mM SDS</b>	0.17	0.31	0.86	0.31	2.15	0.38	1.13	1.08
<b>+ 2 mM SDS</b>	0.16	0.26	1.18	0.32	2.40	0.42	1.42	1.01
<b>+ 4 mM SDS</b>	-	-	-	-	2.90	1	2.90	1.07
<b>+ 8 mM SDS</b>	-	-	-	-	3.10	1	3.10	1.00
<b>+ 16 mM SDS</b>	-	-	-	-	3.14	1	3.14	1.01



**Scheme 6.1.** Interaction of DAPI with different surfactant assemblies of SDS.

### 6.2.3. Effect of Surfactant Assemblies on FRET between DAPI and Ag NC

Figure 6.5A shows the absorption and PL spectra of as-synthesized DHLA-capped Ag NC. The absorption spectrum of Ag NC shows two peaks at 329 and 426 nm with a weak shoulder at 497 nm. The PL spectrum consists of a distinct band centered at 675 nm ( $\lambda_{\text{ex}} = 375$  nm). The absorption and PL maxima match well with the earlier reports [27, 45]. The morphology and size of the Ag NC have been estimated by HRTEM measurements (Figure 6.5B). The image reveals spherical particles with average diameter of  $1.84 \pm 0.12$  nm (inset, Figure 6.5B) [27, 45].

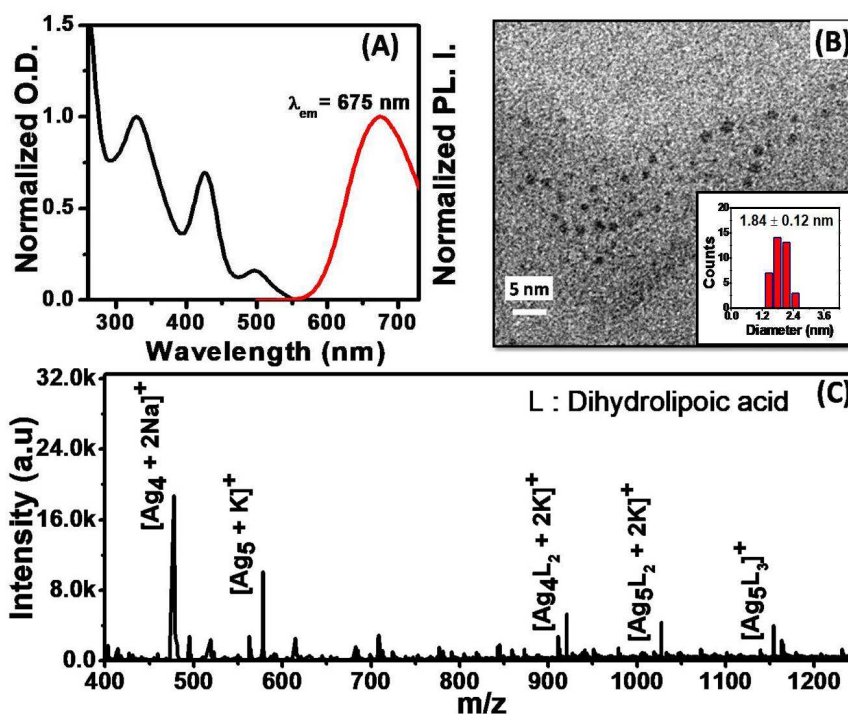


**Figure 6.5.** (A) Normalized absorption (black line) and PL (red line) spectra of synthesized Ag NCs at an excitation wavelength of 375 nm. (B) HRTEM image of Ag NCs. The inset shows the size distribution histogram for Ag NCs generated from HRTEM measurements. (C) ESI mass spectrum of synthesized DHLA capped Ag NCs in 1:1 water-methanol mixture.

Figure 6.5C shows the mass spectrometric analysis of Ag NC. The spectrum reveals a major peak at  $m/z$  477.30 and a minor peak at  $m/z$  578 which can be assigned to  $[Ag_4 + 2Na]^+$  and  $[Ag_5 + K]^+$  clusters, respectively. The other significant peaks at higher  $m/z$  values correspond to ligand associated  $Ag_4$  and  $Ag_5$  clusters. The spectrum correlates well with our earlier reports of Ag NCs revealing majority of the  $Ag_4$  core with a minor amount of  $Ag_5$  core [27].

DAPI-Ag NC forms an excellent FRET pair in aqueous solution due to significant spectral overlap as demonstrated in our earlier report [27]. In the presence of Ag NC, the FL of DAPI quenches with concomitant PL enhancement of Ag NC (Figure 6.6). Previously, using femtosecond upconversion technique we have shown that the average FL lifetime of DAPI decreases from 81.50 to 3.71 ps in the presence of Ag NC [27]. Furthermore, the normalized excitation spectra of Ag NC in the absence and presence of DAPI recorded at 675 nm emission wavelength (with 399 nm filter) show enhanced intensity in the wavelength range 300-400 nm which supports the FRET process from photoexcited DAPI to Ag NC [27].

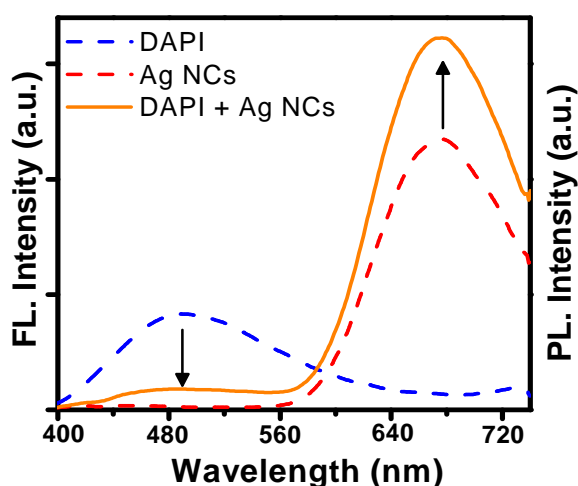


**Figure 6.6.** Changes in the emission spectra ( $\lambda_{ex} = 375$  nm) of DAPI (dash blue) and Ag NC (dash red) upon mixing (solid orange) in PBS.

The FRET efficiency ( $\phi_{\text{Eff}}$ ) from DAPI to Ag NCs was estimated using the following equation:

$$\phi_{\text{Eff}} = 1 - \frac{\phi_{\text{D-A}}}{\phi_{\text{D}}} = 1 - \frac{\tau_{\text{D-A}}}{\tau_{\text{D}}} \quad (1)$$

where  $\phi_{D-A}$  and  $\phi_D$  are the quantum yields of the donor in the presence and absence of the acceptor, respectively. The parameters  $\tau_{D-A}$  and  $\tau_D$  are the average FL lifetime of the donor in the presence and absence of the acceptor, respectively.

The Förster distance  $R_0$  between the donor and acceptor at which 50% energy transfer is observed, was calculated using

$$R_0 = [(8.8 \times 10^{-25})(\kappa^2 \eta^{-4} \phi_D J(\lambda))]^{1/6} \quad (2)$$

where  $\kappa^2$  is the orientation factor of the transition dipoles of the donor and the acceptor,  $\phi_D$  is the quantum yield of the donor,  $\eta$  is the refractive index of the medium and  $J(\lambda)$  is the spectral overlap integral between the donor emission and the acceptor absorption spectra.

With the help of calculated values of  $\phi_{\text{Eff}}$  and  $R_0$ , the distance between donor and acceptor was estimated using the following equation:

$$\phi_{\text{Eff}} = \frac{1}{1 + \left(\frac{R}{R_0}\right)^6} \quad (3)$$

where  $\phi_{\text{Eff}}$  is the energy transfer efficiency and  $R$  is the distance between donor and acceptor. For DAPI-Ag NC pair, the estimated  $\phi_{\text{Eff}}$  from the steady-state data is 78%. The calculated overlap integral is  $5.12 \times 10^{-14} \text{ M}^{-1} \text{ cm}^3$  and the estimated  $R_0$  is 2.42 nm. Based on the estimated  $\phi_{\text{eff}}$  and  $R_0$  values, the separation distance ( $R$ ) of 1.98 nm has been calculated for DAPI-Ag NC FRET pair. The estimated FRET parameters for DAPI-Ag NC pair match well with our previous report [27].

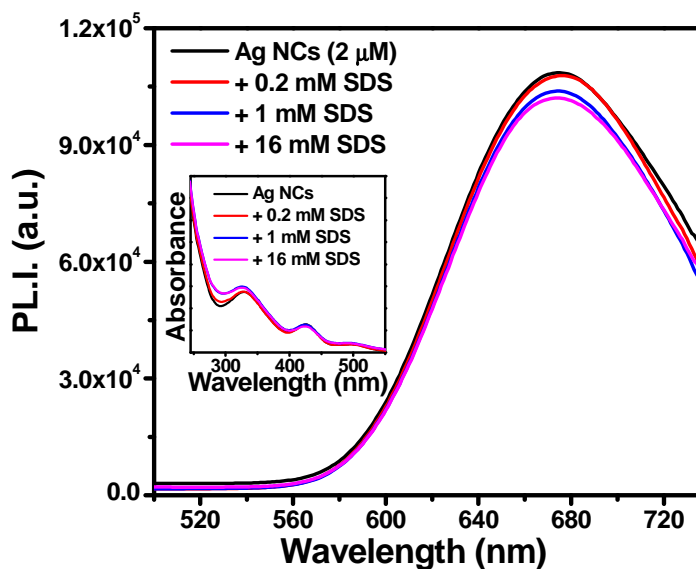


**Figure 6.7.** Changes in the PL spectrum ( $\lambda_{ex} = 375$  nm) of Ag NCs upon gradual addition of SDS. The inset shows the changes in the absorption spectrum of Ag NCs in the presence of SDS.

While DAPI interacts specifically with SDS in a concentration-dependent manner, Ag NC shows no specific interactions with surfactant assemblies (Figure 6.7). The primary goal of the present study is to explore the effect of specific interaction between DAPI and SDS on the efficiency of FRET from DAPI to Ag NC. Here, we have monitored the FL spectra of DAPI in the presence of two different surfactant concentrations namely 1 and 16 mM SDS, upon addition of Ag NC. Figure 6.8A reveals that the extent of fluorescence quenching is significantly less in the presence of 1 mM SDS as compared to that in its absence, indicating less efficient energy transfer. Interestingly, in the presence of 16 mM SDS the peak position as well as the FL intensity of DAPI remains unaltered upon addition of Ag NC indicating complete

suppression of nonradiative FRET between DAPI and Ag NC (Figure 6.8B).

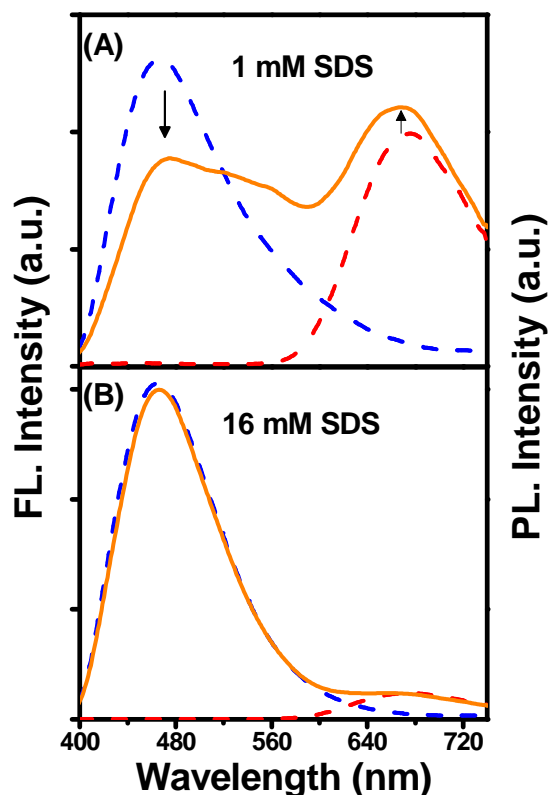


**Figure 6.8.** Changes in the emission spectra ( $\lambda_{ex} = 375$  nm) of DAPI (dash blue) and Ag NC (dash red) upon mixing (solid orange) in (A) 1 mM SDS and (B) 16 mM SDS.

To further substantiate these steady-state results, we have measured the changes in the FL lifetime of DAPI in the presence of two different SDS assemblies upon addition of Ag NC. The lifetime decay traces ( $\lambda_{ex} = 375$  nm) were recorded at 492 nm emission wavelength. For 1 and 16 mM SDS the decays were fitted with bi-exponential and single-exponential decay functions, respectively. All the estimated lifetime components are listed in Table 6.2.

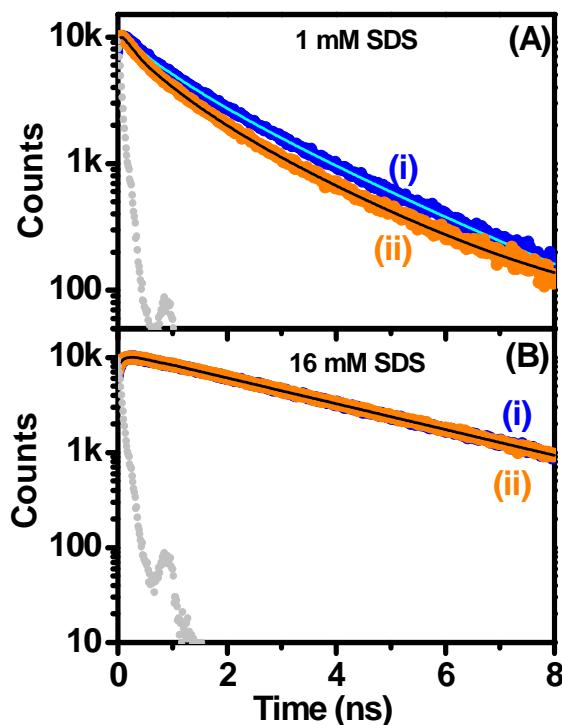


**Figure 6.9.** FL lifetime decay traces ( $\lambda_{ex} = 375$  nm) of DAPI, upon addition of (A) 1 mM and (B) 16 mM SDS in the absence (i) and presence (ii) of Ag NC ( $\lambda_{em} = 492$  nm).

Figure 6.9A shows the changes in lifetime decay traces of DAPI in the presence of 1 mM SDS upon addition of Ag NC. As mentioned earlier, DAPI in the presence of 1 mM SDS has an average FL lifetime of 1.13 ns with lifetime components of 0.17 (31%), 0.86 (31%) and 2.15 (38%) ns. Upon addition of Ag NC, this average lifetime reduces to 0.83 ns with lifetime components of 0.12 (41%), 0.73 (34%) and 2.14 (25%) ns. Notably, the lifetime due to the pre-micelles associated DAPI remains unchanged whereas the lifetimes corresponding to free DAPI and DAPI-SDS aggregate decreases. This clearly indicates that the observed FL quenching of DAPI by Ag NC in the presence of 1 mM SDS is due to the

interaction of Ag NC with free DAPI and DAPI-SDS aggregates whereas the FL from pre-micelles associated DAPI remains unquenched. As a consequence, the overall quenching efficiency due to the non-radiative FRET decreases in 1 mM SDS. Figure 6.9B shows that the lifetime decay of DAPI in the presence of 16 mM SDS remains unaffected upon addition of Ag NC. The FL lifetime of DAPI for 16 mM SDS addition is 3.14 ns which remains unchanged in the presence of Ag NC (Table 6.2). The unchanged average FL lifetime of DAPI in the presence of 16 mM SDS upon addition of Ag NC indicates complete suppression of nonradiative FRET from DAPI to Ag NC.

**Table 6.2.** Fluorescence decay parameters of DAPI-SDS system in the absence and presence of Ag NCs.

Sample (DAPI)	$\tau_1$ (ns)	$a_1$	$\tau_2$ (ns)	$a_2$	$\tau_3$ (ns)	$a_3$	$\langle\tau\rangle$ (ns)	$\chi^2$
+ 1 mM SDS	0.17	0.31	0.86	0.31	2.15	0.38	1.13	1.08
+1 mM SDS + Ag NCs	0.12	0.41	0.73	0.34	2.14	0.25	0.83	1.05
+ 16 mM SDS	-	-	-	-	3.14	1	3.14	1.10
+ 16 mM SDS + Ag NCs	-	-	-	-	3.12	1	3.12	1.06

The radiative and nonradiative decay rates of DAPI in the presence of 1 and 16 mM SDS upon addition of Ag NC are estimated according to the following equations:

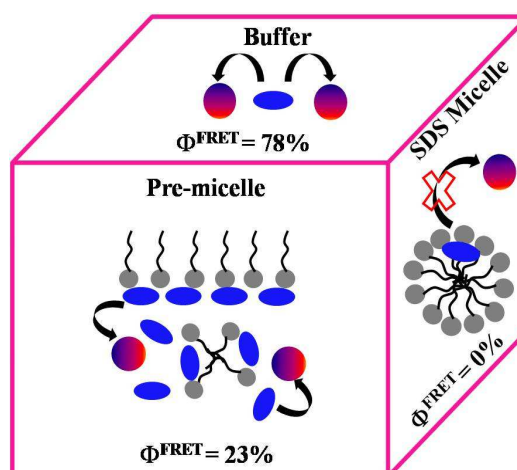
$$k_r = \frac{\phi_D}{\tau_D} \quad (4)$$

$$k_{\text{nr}} = \left( \frac{1 - \phi_{\text{D}}}{\tau_{\text{D}}} \right) \quad (5)$$

where  $k_{\text{r}}$  and  $k_{\text{nr}}$  are the radiative and nonradiative decay rates, respectively.  $\phi_{\text{D}}$  is the quantum yield and  $\tau_{\text{D}}$  is the average lifetime of the donor. It is evident from Table 6.3 that in the presence of 1 mM SDS the radiative rate almost remains same, whereas the nonradiative rate increases from  $0.81 \times 10^9 \text{ s}^{-1}$  to  $1.13 \times 10^9 \text{ s}^{-1}$  indicating nonradiative energy transfer from DAPI to Ag NC. The estimated  $\phi_{\text{Eff}}$  from DAPI (in the presence of 1 mM SDS) to Ag NC from steady-state and time-resolved data is 23% and 27%, respectively (Table 6.3). In the presence of 1 mM SDS, the calculated Förster distance ( $R_0$ ) for DAPI-Ag NC pair increases to 3.17 nm and the separation distance ( $R$ ) between DAPI and Ag NC increases to 3.88 nm (Table 6.3). Due to the specific interactions between DAPI and SDS, the distance between DAPI and Ag NC increases as a result of which, the FRET efficiency for DAPI-Ag NC pair decreases. For 16 mM SDS, DAPI is completely incorporated in the negatively charged SDS micellar Stern layer due to which a complete suppression of FRET from DAPI to Ag NC has been observed. Hence, our results reveal that the concentration-dependent specific interactions between DAPI and SDS significantly affect the FRET efficiency of DAPI-Ag NC pair (Scheme 6.2).

**Table 6.3.** Estimated quantum yields, radiative rates, nonradiative rates, efficiency of energy transfer, and FRET distance for DAPI-Ag NC pair in the presence of 1 mM SDS.

Sample (DAPI)	$\phi_D$	$k_r$ ( $\times 10^9 \text{ s}^{-1}$ )	$k_{nr}$ ( $\times 10^9 \text{ s}^{-1}$ )	$\phi_{\text{Eff}}$ (F)	$\phi_{\text{Eff}}$ ( $\tau$ )	$R_0$ (nm)	$R$ (nm)
+ 1 mM SDS	0.080	0.071	0.81	-	-	-	-
+ 1 mM SDS + Ag NCs	0.062	0.074	1.13	0.23	0.27	3.17	3.88



**Scheme 6.2.** Schematic representation of the modulation of FRET between DAPI and Ag NC due to the addition of 1 mM and 16 mM SDS.

### 6.3. Conclusions

In the present work, we have demonstrated the effect of SDS surfactant assemblies on the FRET between DAPI and Ag NC. DAPI shows specific concentration-dependent interaction with SDS, whereas Ag NC remains unaffected upon addition of SDS. In the presence of 0.2 mM

and 0.4 mM SDS, DAPI-SDS non-specific aggregates are formed at the interface. At 0.6 mM SDS, the existence of DAPI-SDS aggregates at the interface along with the pre-micelle associated DAPI is observed. Upon addition of 1 and 2 mM SDS, the extent of association of DAPI with the pre-micelles of SDS increases, followed by its complete incorporation in the micellar Stern layer at and above 4mM SDS. These specific interactions of DAPI with SDS significantly affect FRET between DAPI and Ag NC. In the presence of 1 mM SDS, the  $\phi_{\text{Eff}}$  for DAPI-Ag NC pair reduces to 23%. Furthermore, this FRET between DAPI and Ag NC completely suppresses at 16 mM SDS due to the incorporation of DAPI into the micellar Stern layer of SDS.

### 6.4. References

1. Jordanides X. J., Scholes G. D., Fleming G. R. (2001), The mechanism of energy transfer in the bacterial photosynthetic reaction center, *J. Phys. Chem. B*, 105, 1652-1669. (DOI: 10.1021/jp003572e)
2. Jordanides X. J., Scholes G. D., Shapley W. A., Reimers J. R., Fleming G. R. (2004), Electronic couplings and energy transfer dynamics in the oxidized primary electron donor of the bacterial reaction center, *J. Phys. Chem. B*, 108, 1753-1765. (DOI: 10.1021/jp036516x)
3. Bates M., Blosser T. R., Zhuang X. (2005), Short-range spectroscopic ruler based on a single-molecule optical switch, *Phys. Rev. Lett.*, 94, 108101-108104. (DOI: 10.1103/PhysRevLett.94.108101)
4. Tucker M. J., Oyola R., Gai F. (2005), Conformational distribution of a 14-residue peptide in solution: A fluorescence resonance energy transfer study, *J. Phys. Chem. B*, 109, 4788-4795. (DOI: 10.1021/jp044347q)
5. Wang D., Geva E. (2005), Protein structure and dynamics from single-molecule fluorescence resonance energy transfer, *J. Phys. Chem. B*, 109, 1626-1634. (DOI: 10.1021/jp0478864)
6. Kuzmenkina E. V., Heyes C. D., Nienhaus G. U. (2005), Single-molecule Förster resonance energy transfer study of protein dynamics under denaturing conditions, *Proc. Natl. Acad. Sci. U.S.A.*, 102, 15471-15476. (DOI: 10.1073/pnas.0507728102)

7. Schuler B., Lipman E. A., Steinbach P. J., Kumke M., Eaton W. A. (2005), Polyproline and the “spectroscopic ruler” revisited with single-molecule fluorescence, *Proc. Natl. Acad. Sci. U.S.A.*, 102, 2754-2759. (DOI: 10.1073/pnas.0408164102)
8. Goldman E. R., Medintz I. L., Whitley J. L., Hayhurst A., Clapp A. R., Uyeda H. T., Deschamps J. R., Lassman M. E., Mattoussi H. (2005), A hybrid quantum dot-antibody fragment fluorescence resonance energy transfer-based TNT sensor, *J. Am. Chem. Soc.*, 127, 6744-6751. (DOI: 10.1021/ja0436771)
9. Bain D., Paramanik B., Sadhu S., Patra A. (2015), A study into the role of surface capping on energy transfer in metal cluster-semiconductor nanocomposites, *Nanoscale*, 7, 20697-20708. (DOI: 10.1039/c5nr06793f)
10. Lakowicz J. R., (1999), *Principles of fluorescence spectroscopy*, 2nd ed., Academic Press, New York. (ISBN: 0-306-46093-9)
11. Maiti N. C., Krishna M. M. G., Britto P. J., Periasamy N. (1997), Fluorescence dynamics of dye probes in micelles, *J. Phys. Chem. B*, 101, 11051-11060. DOI: 10.1021/jp9723123
12. Bhattacharyya K. (2003), Solvation dynamics and proton transfer in supramolecular assemblies, *Acc. Chem. Res.*, 36, 95-101. (DOI: 10.1021/ar020067m)
13. Ghatak C., Rao V. G., Pramanik R., Sarkar S., Sarkar N. (2011), The effect of membrane fluidity on FRET parameters: An energy transfer study inside small unilamellar vesicle, *Phys. Chem. Chem. Phys.*, 13, 3711-3720. (DOI: 10.1039/C0CP01925A)

14. Paul B. K., Guchhait N. (2011), Exploring the strength, mode, dynamics, and kinetics of binding interaction of a cationic biological photosensitizer with DNA: implication on dissociation of the drug-DNA complex via detergent sequestration, *J. Phys. Chem. B*, 115, 11938-11949. (DOI: 10.1021/jp206589e)
15. Ray D., Paul B. K., Guchhait N. (2012), A spectroscopic investigation on the interaction of a magnetic ferrofluid with a model plasma protein: effect on the conformation and activity of the protein, *Phys. Chem. Chem. Phys.*, 14, 12182-12192. (DOI: 10.1039/C2CP41292F)
16. Jana B., Senapati S., Ghosh D., Bose D., Chattopadhyay N. (2012), Spectroscopic exploration of mode of binding of ctDNA with 3-hydroxyflavone: A contrast to the mode of binding with flavonoids having additional hydroxyl groups, *J. Phys. Chem. B*, 116, 639-645. (DOI: 10.1021/jp2094824)
17. Valle L., Vieyra F. E. M., Borsarelli C. D. (2012), Hydrogen-bonding modulation of excited-state properties of flavins in a model of aqueous confined environment, *Photochem. Photobiol. Sci.*, 11, 1051-1061. (DOI: 10.1039/c2pp05385c)
18. Martin C., Cohen B., Gaamoussi I., Ijjaali M., Douhal A. (2014), Ultrafast dynamics of C30 in solution and within CDs and HSA protein, *J. Phys. Chem. C*, 118, 5760-5771. (DOI: 10.1021/jp5026575)
19. Ghosh S., Banik D., Roy A., Kundu N., Kuchlyan J., Sarkar N. (2014), Spectroscopic investigation of the binding interactions of a membrane potential molecule in various supramolecular confined

environments: Contrasting behavior of surfactant molecules in relocation or release of the probe between nanocarriers and DNA surface, *Phys. Chem. Chem. Phys.*, 16, 25024-25038. (DOI: 10.1039/c4cp03178d)

20. De S., Girigoswami A. (2004), Fluorescence resonance energy transfer - A spectroscopic probe for organized surfactant media, *J. Colloid Interface Sci.*, 271, 485-495. (DOI: 10.1016/j.jcis.2003.10.021)

21. Liu B., Liu Z., Cao Z. (2006), Fluorescence resonance energy transfer between acridine orange and rhodamine 6G and analytical application in micelles of dodecyl benzene sodium sulfonate, *J. Lumin.*, 118, 99-105. (DOI: 10.1016/j.jlumin.2005.08.001)

22. Mondal S. K., Ghosh S., Sahu K., Mandal U., Bhattacharyya K. (2006), Ultrafast fluorescence resonance energy transfer in a reverse micelle: Excitation wavelength dependence, *J. Chem. Phys.*, 125, 224710. (DOI: 10.1063/1.2403131)

23. Erogbogbo F., Chang C. May W., J. , Prasad P. N., Swihart M. T. (2012), Energy transfer from a dye donor to enhance the luminescence of silicon quantum dots, *Nanoscale*, 4, 5163-5168. (DOI: 10.1039/c2nr31003a)

24. Rao V. G., Mandal S., Ghosh S., Banerjee C., Sarkar N. (2012), Study of fluorescence resonance energy transfer in zwitterionic micelle: Ionic-liquid-induced changes in FRET parameters, *J. Phys. Chem. B*, 116, 12021-12029. (DOI: 10.1021/jp307883r)

25. Liu L., Fei X., Zhu S., Yu L., Zhang B. (2013), Self-assembly of anionic Gemini surfactant: Fluorescence resonance energy transfer and simulation study, *Langmuir*, 29, 5132-5137. (DOI: 10.1021/la304980r)
26. Roy A., Kundu N., Banik D., Sarkar N. (2016), Comparative fluorescence resonance energy-transfer study in pluronic triblock copolymer micelle and niosome composed of biological component cholesterol: An investigation of effect of cholesterol and sucrose on the FRET parameters, *J. Phys. Chem. B*, 120, 131-142. (DOI: 10.1021/acs.jpcc.5b09761)
27. Prajapati R., Chatterjee S., Kannaujiya K. K., Mukherjee T. K. (2016), Effect of compartmentalization of donor and acceptor on the ultrafast resonance energy transfer from DAPI to silver nanoclusters, *Nanoscale*, 8, 13006-13016. (DOI: 10.1039/c6nr01792d)
28. Barcellona M. L., Cardiel G., Gratton E. (1990), Time-resolved fluorescence of DAPI in solution and bound to polydeoxynucleotides, *Biochem. Biophys. Res. Commun.*, 170, 270-280. (DOI: 10.1016/0006-291X(90)91270-3)
29. Barcellona M. L., Gratton E. (1991), A molecular approach to 4',6-diamidino-2-phenylindole(DAPI) photophysical behaviour at different pH values, *Biophys. Chem.*, 40, 223-229. (DOI: 10.1016/0301-4622(91)80022-J)
30. Mazzini A., Cavatorta P., Iori M., Favilla R., Sartor G. (1992), The binding of 4',6-diamidino-2-phenylindole to bovine serum albumin, *Biophys. Chem.*, 42, 101-109. (DOI: 10.1016/0301-4622(92)80012-T)

31. Manzini G., Barcellona M. L., Avitabile M., Quadrifoglio F. (1983), Interaction of diamidino-2-phenylindole (DAPI) with natural and synthetic nucleic acids, *Nucleic Acids Res.*, 11, 8861-8875. (DOI: 10.1093/nar/11.24.8861)
32. Favilla R., Stecconi G., Cavatorta P., Sartor G., Mazzini A. (1993), The interaction of DAPI with phospholipid vesicles and micelles, *Biophys. Chem.*, 46, 217-226. (DOI: 10.1016/0301-4622(93)80015-B)
33. Barcellona M. L., Gratton E. (1996), Torsional dynamics and orientation of DNA-DAPI complexes, *Biochemistry*, 35, 321-333. (DOI: 10.1021/bi951027b)
34. Banerjee D., Pal S. K. (2008), Excited-state solvation and proton transfer dynamics of DAPI in biomimetics and genomic DNA, *J. Phys. Chem. A*, 112, 7314-7320. (DOI: 10.1021/jp801778e)
35. Shinde M. N., Bhasikuttan A. C., Mohanty J. (2015), The contrasting recognition behavior of  $\beta$ -cyclodextrin and its sulfobutylether derivative towards 4',6-diamidino-2-phenylindole, *ChemPhysChem*, 16, 3425-3432. (DOI: 10.1002/cphc.201500638)
36. Sarkar M., Poddar S. (2000), Studies on the interaction of surfactants with cationic dye by absorption spectroscopy, *J. Colloid Interface Sci.*, 221, 181-185. (DOI: 10.1006/jcis.1999.6573)
37. Duman O., Tunç S., Kancı B. (2011), Spectrophotometric studies on the interactions of CI Basic Red 9 and CI Acid Blue 25 with hexadecyltrimethylammonium bromide in cationic surfactant micelles, *Fluid Phase Equilib.*, 301, 56-61. (DOI: 10.1016/j.fluid.2010.11.018)

38. Tunç S., Duman O., Kancı B. (2012), Spectrophotometric study of the interactions between cationic color (CI general yellow 2) and anionic surfactant (sodium dioctylsulfosuccinate) in the premicellar and the Maysel region, *Dyes Pigm.*, 94, 233-238. (DOI: 10.1016/j.dyepig.2012.01.016)
39. Chatterjee S., Mukherjee T. K. (2013), Size-dependent differential interaction of allylamine-capped silicon quantum dots with surfactant assemblies studied using photoluminescence spectroscopy and imaging technique, *J. Phys. Chem. C*, 117, 10799-10808. (DOI: 10.1021/jp402408d)
40. Chen H., Farahat M. S., Law K. Y., Whitten D. G. (1996), Aggregation of surfactant squaraine dyes in aqueous solution and microheterogeneous media: Correlation of aggregation behavior with molecular structure, *J. Am. Chem. Soc.*, 118, 2584-2594. (DOI: 10.1021/ja9523911)
41. Maiti N. C., Majumdar S., Periasamy N. (1998), J- and H-aggregates of porphyrin-surfactant complexes: Time-resolved fluorescence and other spectroscopic studies, *J. Phys. Chem. B*, 102, 1528-1538. (DOI: 10.1021/jp9723372)
42. Guralchuk G. Y., I Katrunov. K., Grynyov R. S., Sorokin A. V., Yefimova S. L., Borovoy I. A., Malyukin Y. V. (2008), *J. Phys. Chem. C*, 112, 14762-14768. (DOI: 10.1021/jp802933n)
43. Fuguet E., Ra`fols C., Bosch E., Rose´s M. (2003), Characterization of the solvation properties of sodium n-dodecyl sulfate

micelles in buffered and unbuffered aqueous phases by solvatochromic indicators, *Langmuir*, 19, 55-62. (DOI: 10.1021/la026307o)

44. Fuguet E., Rañols C., Rosés M., Bosch E. (2005), Critical micelle concentration of surfactants in aqueous buffered and unbuffered systems, *Anal. Chim. Acta*, 548, 95-100. (DOI: 10.1016/j.aca.2005.05.069)

45. Adhikari B., Banerjee A. (2010), Facile synthesis of water-soluble fluorescent silver nanoclusters and Hg(II) sensing, *Chem. Mater.*, 22, 4364-4371. (DOI: 10.1021/cm1001253)

## **Chapter 7**

### *Conclusions and Future Scopes*

### 7.1. Conclusions

The resonance EET from various photoexcited donors to acceptors has been studied thoroughly in the recent past due to its importance in photovoltaics, light-emitting diodes, sensors, bioimaging, etc. Despite of numerous reports, the fundamental mechanism of EET from various photoexcited donors to metal NP as well as the role of spectral overlap in the EET process still remains obscure. Moreover, very less is known about the mechanism and dynamics of fluorescence quenching near the ultrasmall metal NC, which lacks characteristic LSPR. Therefore, a comprehensive study was required to reveal the mechanism and dynamics of EET from various photoexcited donors to metal NPs and NCs as well as the role of spectral overlap. Here in this thesis, the detailed mechanism and dynamics of EET from various photoexcited donors such as Si QDs, CDs, and DAPI to Ag NPs and Ag NCs as acceptors have been demonstrated. The PL quenching of photoexcited donors in the presence of Ag NPs correlates well with NSET rather than FRET model. Moreover, the involvement of spectral overlap in the NSET process has been clearly revealed. Further, the effect of different sizes of Ag NPs on NSET efficiency has also been displayed. The mechanism and dynamics of fluorescence quenching of photoexcited DAPI near the ultrasmall Ag NCs has been explained using the FRET model. Furthermore, the influence of various microheterogeneous environments such as CTAB, SDS, PDADMAC, and DNA on the efficiency of energy transfer has also been illustrated. The following next paragraphs discuss the chapter-wise conclusion of the entire work of this thesis.

In chapter three, it has been demonstrated that the observed PL quenching of Si QDs in the presence of Ag NPs is mainly due to the EET

from photoexcited Si QD to the surface of Ag NP. The quenching in steady-state PL yield as well as in the excited-state lifetime of Si QDs in the presence of Ag NPs is due to the increased nonradiative decay rate, while the radiative decay rate remains almost constant. The experimentally estimated quenching efficiency from the lifetime data correlates well with the NSET mechanism rather than FRET mechanism. The NSET efficiency significantly reduces in the presence of 0.5 mM CTAB. CTAB molecules not only induce aggregation of Ag NPs but also provide an extra bilayer shell on top of the citrate-capped Ag NPs, due to which the mean separation distance between Si QD and the surface of Ag NP increases. As a result, the NSET efficiency decreases.

In chapter four, the resonant NSET process between CD and different sized citrate-capped Ag NPs has been illustrated. The steady-state and time-resolved lifetime measurements reveal significant PL quenching of CD in the presence of Ag NPs. The origin behind this PL quenching of CD has been rationalized on the basis of increased nonradiative decay rate due to NSET from photoexcited CD to Ag NP surface. Moreover, it has been observed that the efficiency of this NSET increases with increase in the size of Ag NPs. This phenomenon has been explained by considering the extent of spectral overlap and distance between CD and different sized Ag NPs. It has been observed that with increase in the size of Ag NPs, the spectral overlap increases. More importantly, the zeta potential of Ag NPs decreases with increase in the size and as a consequence, the effective distance between CD and Ag NPs decreases due to reduced electrostatic repulsion. These findings reveal that the efficiency of NSET process can be easily tuned as a function of NP size.

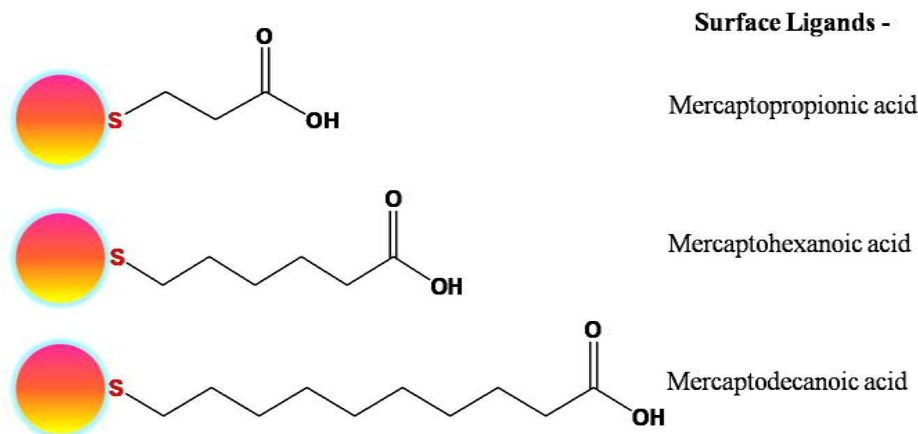
In chapter five, the fundamental mechanism behind the fluorescence (FL) quenching of DAPI in the presence of ultrasmall Ag NC and its subsequent modulation in the presence of PDADMAC polymer and CT-DNA have been explored. The FL of DAPI significantly quenches in the presence of Ag NCs. Importantly, the concomitant increase in the PL of Ag NCs clearly signifies the involvement of FRET from DAPI to Ag NC. The FL quenching is predominantly nonradiative in nature with significant shortening of the excited-state lifetime of DAPI. This nonradiative FRET process completely suppresses in the presence of a cationic polymer PDADMAC. Steady-state PL, HRTEM and PL imaging measurements reveal efficient and complete encapsulation of acceptor (Ag NC) within the polymer matrix. The effect of selective compartmentalization of donor (DAPI) on the FRET process has also been demonstrated in the presence of CT-DNA. The nonradiative FRET process completely suppresses in the presence of CT-DNA due to the selective binding of DAPI with CT-DNA.

In chapter six, the effect of SDS assemblies on the FRET between DAPI and Ag NC in phosphate buffer has been demonstrated by using FL spectroscopy. While DAPI interacts specifically with SDS surfactants in a concentration-dependent manner, Ag NC shows no specific interaction with surfactant assemblies. At very low concentrations of SDS ( $< 0.6$  mM), DAPI forms surfactant-induced aggregates at the interface. In the case of intermediate SDS concentrations ( $0.6 \text{ mM} \leq \text{SDS} < 4 \text{ mM}$ ), DAPI associates with the negatively charged SDS pre-micelles via electrostatic interaction. Beyond 4 mM SDS, the FL intensity of DAPI saturates due to complete incorporation of DAPI into the micellar Stern layer. The negligible changes in the FL of DAPI upon addition of non-ionic triton X-

100 (TX-100) and cationic CTAB surfactants indicate minimal interaction of DAPI with TX-100 and CTAB. Hence, the significant FL enhancement of DAPI in the presence of SDS is due to the specific electrostatic interactions between the positively charged DAPI and negatively charged SDS. Notably, the interaction between DAPI and Ag NC significantly perturbs in the presence of SDS. In phosphate buffer, FRET efficiency ( $\phi_{\text{Eff}}$ ) of 78% has been estimated for DAPI-Ag NC pair. This  $\phi_{\text{Eff}}$  decreases to 23% in the presence of 1 mM SDS. Furthermore, in the presence of 16 mM SDS, complete suppression of this nonradiative FRET has been observed due to the incorporation of DAPI into the micellar Stern layer.

### 7.2. Scope for Future Works

Resonance energy transfer being a sensitive and selective fluorescence technique has been widely used in various research fields. The present thesis unveils the fundamental mechanism and dynamics of the EET from various photoexcited donors such as Si QDs, CDs, and DAPI to Ag NPs and Ag NCs as acceptors. Moreover, in this thesis, the effect of various microheterogeneous environments such as surfactants, polymer, and DNA on the efficiency of energy transfer has also been illustrated. In chapter 3 and 4, the role of spectral overlap and size of NPs in NSET has been demonstrated from photoexcited Si QDs and CDs to Ag NPs. Further, the effect of donor-acceptor separation distance on the efficiency of resonance EET can be investigated. For example, the separation distance between the positively charged donor and negatively charged metal NP can be varied by using stabilizing agents of different alkyl chain lengths containing both thiol as well as carboxylic acid groups such as mercaptopropionic acid, mercaptohexanoic acid, mercaptodecanoic acid, etc (Scheme 7.1).



**Scheme 7.1.** Schematic representation of metal NPs with surface ligands having different alkyl chain length.

The separation distance between the donor and acceptor can also be controlled by covalent attachment of donor and acceptor using different spacer molecules such as peptides, dendrimers, DNA strands, etc. In chapter 5 and 6, the FRET has been demonstrated from photoexcited DAPI to Ag NC, followed by its subsequent suppression in the presence of polymer, DNA, and SDS assemblies. Further, different types of quantum dots can be synthesized which can be used as donors for EET studies. For example, a comparative study of the resonance EET can be carried out by synthesizing traditional quantum dots (e.g. CdSe, CdS, ZnSe, etc.) core-shell quantum dots (e.g. CdSe/ZnS, PbS/CdS, etc.) and recently emerging perovskite quantum dots (e.g. CsPbBr<sub>3</sub>, CH<sub>3</sub>NH<sub>3</sub>PbCl<sub>3</sub>, etc.) with tunable band gap. Depending upon the optical properties of these QDs, metal nanoclusters as acceptors can be strategically chosen. Such donor-acceptor pairs can further be utilized for various optoelectronic and photovoltaic applications.